NORTHEASTERN UNIVERSITY
Graduate School of Engineering

Dissertation Title: Investigation of Defects in Thermal Sprayed Coatings using Impedance Spectroscopy

Author: Ali Marzban

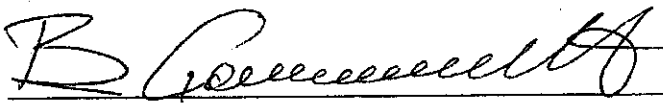Department: Mechanical and Industrial Engineering

Approved for Dissertation Requirement for the Doctor of Philosophy Degree

_____   _8/17/10_____
Dissertation Advisor - Professor Andrew Gouldstone   Date
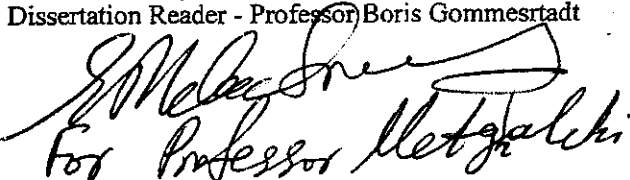
_____   _8/14/2010_____
Dissertation Reader - Professor Sinan Muftu   Date
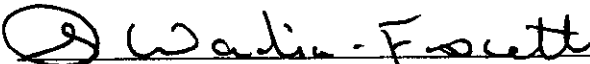
_____   _08/06/2010_____
Dissertation Reader - Professor Boris Gommesrtadt   Date

_____   _08/17/2010_____
Department Chair - Professor Hameed Metghalchi   Date

Graduate School Notified of Acceptance:

_____   _8/19/2010_____
Director of the Graduate School   Date

INVESTIGATION OF DEFECTS IN THERMAL SPRAYED
COATINGS USING IMPEDANCE SPECTROSCOPY

A Dissertation Presented

by

Ali Marzban

to

The Department of Mechanical and Industrial Engineering

in partial fulfillment of the requirements
for the degree of

Doctor of Philosophy
in the field of

Mechanical Engineering

Northeastern University
Boston, Massachusetts

Aug. 2010

ABSTRACT

Thermal spray (TS) coatings and materials including thermal barrier, tribological and anti-corrosive coatings have established application across a number of engineering fields. TS is attractive for these systems due to its low cost, ability to coat large areas and flexibility in material feedstock. These attributes, along with improvements in process diagnostics have spurred the exploration of TS for more functional applications including fuel cells, conformal electronic sensors and biomedical implants. Successful implementation of TS coatings in these systems will require more robust characterization of their mechanical behavior; to date this has been limited and in practice most measurements are carried out in a pass/fail manner. Little is known about the intrinsic or progressive behavior of the coatings under repeated loading. This is important as the microstructure of TS coatings comprises layers of micron-thick flattened particles ('splats') separated by interfaces, the bonding between which is not well understood. These interfaces represent potential short crack growth sites throughout the material. A lot of works has demonstrated that microstructurally short cracks propagate at substantially higher growth rates than long cracks at equivalent driving forces under both quasi-static and cycling loading conditions in ceramics and their composites and metals. Short cracks in a naturally broken material like TS will have a different mechanism.

Mechanical properties and fracture behavior have been examined in TS, but via conventional methods. That is to say, a large notch is introduced and allowed to propagate. This method completely neglects the existing microstructure of a TS material, which is lamellar and contains a number of near-horizontal cracks. In this study, a new

approach to damage monitoring in TS coatings, using through thickness impedance spectroscopy to detect changes in dielectric properties is introduced. The goal of this research is to understand the fatigue behavior and microstructure changes of thermal spray coatings under low strain cycling. Results showed a significant increase in relative dielectric constant of thermal sprayed coatings under tension (R=0) which is due to the growth of micro-scale pre-existing cracks. Yttria-Stabilized Zirconia (YSZ) were deposited on tapered cantilever beam substrates to provide constant in-plane cyclic strains. Relative dielectric constant of coatings was measured via impedance spectroscopy. A Finite Element (FE) model of a randomly distributed network of short crack pairs under a Paris law type stable crack growth was used to model the growth of micro-scale pre-existing cracks in coatings. Experiments confirm growth of micro-cracks in thermal spray coatings which are in good comparison with Finite Element (FE) models.

ACKNOWLEDGEMENTS

I would like to thank all people who have helped me during my graduate study. I especially want to thank my advisor, Professor Andrew Gouldstone, for his guidance during my research and study at Northeastern University. His wide knowledge and logical way of thinking have been of great value for me. His understanding, encouraging and personal guidance have provided a good basis for the present thesis.

It is difficult to overstate my gratitude to Professor Sinan Muftu for his support, inspiration, and his great efforts to explain things clearly and simply. I would not have been able to complete this work without his help.

And especial thanks to Professor Boris Gommerstadt for his warmth support whenever I needed his advice.

My deepest gratitude goes to my family for their love and support throughout my life; this dissertation was simply impossible without them.

This acknowledgement would be incomplete, if I miss to mention the support I received from my research group, and friends especially Amin Ajdari, Samira Faegh, Maricris Silva Abelarde and Salmon Masbooghi Kakhoran. Without their help and support, I won't be able to make this happen.

TABLE OF CONTENTS

LIST OF FIGURES

CHAPTER 1. Introduction

1.1 Introduction to Thermal Spray Coating

Thermal Spraying technique is a coating process in which the molten particles of coating material are sprayed onto a substrate. The coating material is heated by electrical (plasma) or chemical (combustion flame) means. Thermal spraying can provide thick coatings over a large area of substrate. Coatings' fed are in the form of powder and they will be heated to a molten or semi-molten state and accelerated toward the substrates in the form of molten particles (splats). The speed of the molten splats vary from 50 to 200 m/s for different coating setups. Coating layer is made of accumulation of numerous amount of these splats [1].

1.2 Literature Review

Coatings are widely used to insulate and protect hot-section metal components in advanced gas-turbines (aircrafts and power generations) and diesel engines for propulsion and power generation. By lowering the temperature of substrate, coatings can improve the durability of the metal components and enhancing engine performance [2-5]. TS is attractive for these systems due to its low cost, ability to coat large areas and flexibility in material feedstock. These attributes, along with improvements in process diagnostics have spurred the exploration of TS for more functional applications including fuel cells [6], electronic sensors [7] and biomedical implants [8]. Successful usage of TS coatings in these systems will require more robust characterization of their mechanical behavior; which has been limited till now [9].

The microstructure of TS coatings includes layers of micron-thick flattened particles ('splats') separated by interfaces, the bonding between which is not well understood [10-11]. These interfaces represent potential short crack growth sites throughout the material. Generally, a thermal sprayed coating has many local micro-cracks inside, because the coating is a porous material and it is coated on a rough surface which has a blasting treatment [12]. The micro-cracks behavior is similar to the literature discussion of short cracks [13-15], in ceramics [16-20] and composites [21-22], for which a number of size-dependent mechanisms have been discussed.

Little is known about the intrinsic or progressive behavior of the coatings under repeated loading. Impedance Spectroscopy (IS) has been widely used to measure the electrical properties of materials and electrochemical behaviors. Impedance Spectroscopy (IS) of coatings reflect changes in thickness, porosity, and cracks' length of the coating [5]. During impedance measurements, an electrode is placed on the top surface of coated sample with a metal substrate as the other electrode. An electric field with varying frequency is applied to the electrodes. Therefore, the electrical response from different layers of the coating can be separated in the impedance spectra and the microstructure of coating can be correlated to the impedance spectroscopy (IS) parameters. Changes in the microstructure (i.e. micro-cracks, porosity, etc) lead to changes of electrical properties and thereby causes variations of the impedance spectra output (i.e. capacitance, relative dielectric constant, etc) [5]. Therefore, the micro-structural changes of coating during a fatigue test can be monitored with IS.

1.3   Thermal Spray (TS) Coating Procedure

As the goal of this study was to ascertain damage and defects in thermal spray coatings under fatigue test, capacitance was measured on as-sprayed, unpolished coating surfaces. Thermal Spraying technique is a coating process in which the molten particles of coating material are sprayed onto a work piece. As it is shown in Figure 1-1-(B), the coating material is heated by electrical (plasma) or chemical (combustion flame) means. The speed of the molten splats vary from 50 to 200 m/s for different coating setups. Coating layer is made of accumulation of numerous amount of these splats (Figure 1-1-(C)). Thermal spraying can provide thick coatings over a large area of substrate. Coatings' fed are in the form of powder and they will be heated to a molten or semi-molten state and accelerated toward the substrates in the form of molten particles (splats).
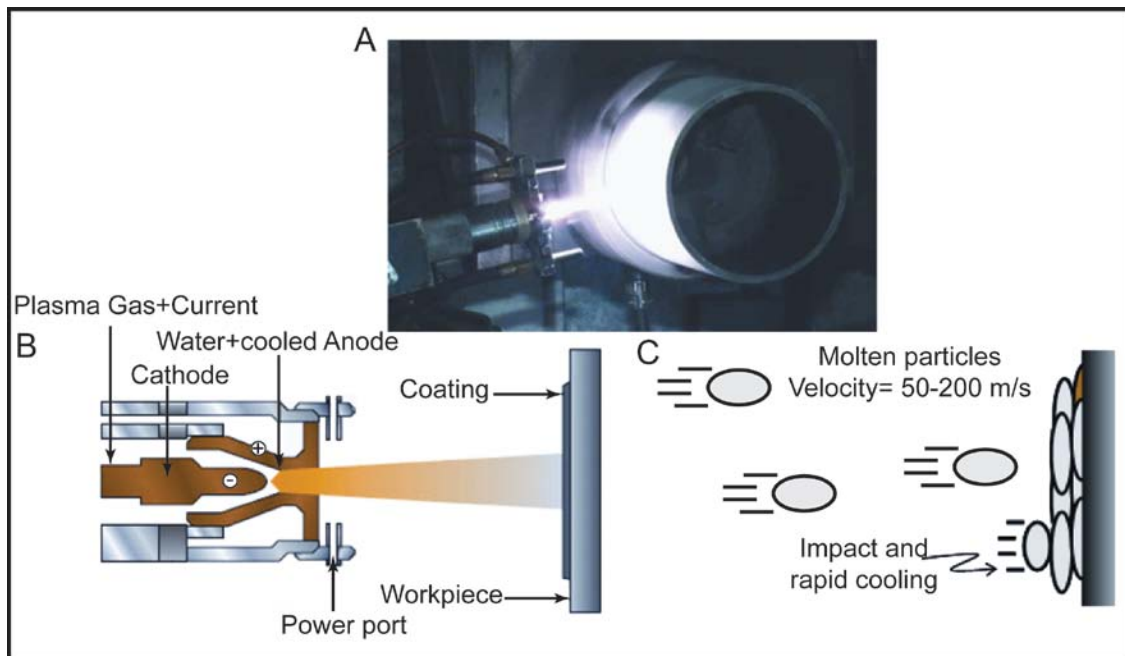
Figure 1-1-A) Thermal spray procedure; B) Schematic thermal spray process; C) high velocity molten particles which make splats on a substrate

There are several kind of thermal spraying as follows:

o High-velocity oxy-fuel coating spraying (HVOF)

o Cold spraying

o Detonation spraying

o Flame spraying

o Wire arc spraying

o Warm spraying

o Air plasma spraying (APS)

The procedure of some them will be explained in following sections.

1.3.1 High-Velocity Oxy-Fuel Coating Spraying (HVOF)

High velocity oxy-fuel spraying was developed in 1980s. A mixture of fuel and oxygen is fed into a combustion chamber, where they are ignited and combusted continuously. The resultant hot gas at a pressure near 1 MPa merges through a nozzle and travels through a straight section. The jet velocity at the exit of the barrel is more than 1000 m/s and exceeds the speed of sound. The spraying material is injected into the gas stream as a powder. The stream of hot gas and powder is directed towards the substrate. The powder partially melts in the stream, and deposits on the surface. The resulting coating has low porosity and a very high bond strength. This kind of coatings can be produced as thick as 12 mm [1].

1.3.2 Cold Spraying

Cold spraying has been introduced in the 1990s. In this method, particles are accelerated to a very high velocity by the carrier gas forced through a nozzle. Upon impact, solid particles with a high kinetic energy deform plastically and produce a mechanical bond with the substrate to form a coating. The velocity of the particles to make a coating depends on the powder size, materials properties, and temperature. The efficiency of this type of coating is low, and the window of changing process parameters and suitable powder sizes is narrow. To accelerate powders to higher velocity, finer powders is necessary [1].

1.3.3 Wire Arc Spraying

Wire arc spray is a form of thermal spraying where two consumable metal wires are fed independently into the spray gun. These wires are then charged and an arc is generated between them. The heat from this arc melts the incoming wire, which is then entrained in air jet from the gun. This entrained molten feedstock is then deposited onto a substrate. This process is commonly used for metallic, heavy coatings [1].

1.3.4 Warm Spraying

Warm spraying is a new modification of HVOF spraying, in which the temperature of the combustion chamber is lowered by adding nitrogen to the combustion

gas. By this modification, warm spraying process is closer to the cold spraying. The coating efficiency is higher than the cold spraying. Besides, the lower temperatures in this method will reduce chemical reactions and melting of the powder comparing to HVOF [1].

1.3.5 Air Plasma Spraying (APS)

A typical air plasma spraying system consists of a spray torch, a feeder, and a media supply. The spray torch or spray gun is the core device of the thermal spraying which perform the melting and acceleration process of the particles to be deposited. Feeder supplies the powder to the torch. Media supply provides the gases for the flame generation and gases for carrying the powder. In most cases, the torch is moving by a robot for maneuvering over the substrate.

In plasma spraying procedure, the powder is injected in a plasma jet where the temperature is about 10,000 K. The melted particles are pushed toward the substrate where will rapidly solidified upon impact. The interaction between the flattened particles and the substrate is a complicated procedure which highly depends on the powder type, flow rate, torch offset distance and substrate cooling technique.

CHAPTER 2. Experiments

For our experiments, the substrates were made of Aluminum and was deposited by Yttria-Stabilized Zirconia (YSZ) coating (Figure 2-1). The molten particles (splats) of the coating were deposited on cleaned and grit-blasted substrates with a very high velocity. Therefore, thermal spray coating's layer includes layers of micron-thick flattened splats separated by interfaces which are potential short crack growth sites. The average reported crack size in thermal spray coatings is about 10µm with an angle of 10 to 20 degree with respect to the substrate surface [23-24].

Figure 2-1- Yttria-Stabilized Zirconia (YSZ) coating.

Different amount of materials used in coating procedure will cause different coating property and thickness. The different amount of materials which were used in four experimental sample of coatings are listed in Table 1.

Table 1-Different materials used in coatings

	Sample#1	Sample#2	Sample#3	Sample#4
Coating Thickness (mm)	0.2	0.22	0.26	0.40
Current (A)	700	700	700	700
Argon (slm)	40	55	55	30
Helium (slm)	10	10↔15	10	5
Hydrogen (slm)	0	0	0	0
Carrier (slm)	4.0	4.0	4.0	4.0
Federate (RPM)	3.0	3.0	3.0	3.0

2.1 Impedance Spectroscopy

Impedance Spectroscopy (IS) is a very powerful method for characterizing electrical properties of materials and its interface with electronically conducting electrodes. It may be used in investigating the electrical property of the bulk or the interfacial regions of any kind of solid or liquid material. Two parallel circular or rectangular electrodes are used to evaluate the electrochemical behavior of a material in electrical measurements. The general approach is to observe the response (the resulting voltage or current) of the system to a known applied electrical stimulus (voltage or current) [25-26]. Impedance Spectroscopy uses alternating current with low amplitude to facilitate a non-invasive method for detailed observation of behavior of many systems. This method is useful in investigating the processes occurring at the molecular level, such as biological and synthetic membranes or interfaces between solutions and various solids [27].

2.1.1 Fundamental

There are three different ways to use Impedance Spectroscopy. In the first method, a step function of voltage $V(t)$ will be applied at $t=0$, where $V(t)=V_0$ for $t>0$ and $V(t)=0$ for $t<0$. The ratio of $V_0/i(t)$ is called indicial impedance and is resultant of step function voltage perturbation. This time-varying quantity will be transformed to frequency domain by using Fourier transform. This transformation is valid when $|V_0|$ is sufficiently small and the system response is linear. The advantage of this easy method is that the independent variable (voltage) controls the rate of the electrochemical reactions at the interface. Disadvantage of this method is that the impedance is not determined over all desired frequencies [25].

In the second method, a signal $V(t)$ composed of random noise will be applied to the system and the resultant current will be measured. Again the results will be transformed to frequency domain by using Fourier transform. This method offers a very short data collection time because only one signal is applied to the interface for a short time. The disadvantage of this method is necessity of using random noise and Fourier transform which can be computationally difficult.

In the third method which is the most common and standard one, a single frequency voltage will be applied to the system and the phase shift and amplitude (i.e. real and imaginary parts) of the resulting current will be measured. The impedance of any system can be measured in the range of 1mHz to 1MHz by using commercial instruments with this method. The advantage of this method is ease of use and availability of commercial instruments. In addition, the desired frequency for measuring impedance can be controlled.

In Impedance Spectroscopy, a monochromatic signal $V(t)=V_m \ sin(\omega t)$ will be applied to the system and the resultant steady state current $i(t)=I_m \ sin(\omega t+\theta)$ will be measured. The conventional impedance will be defined as $Z(\omega)=v(t)/i(t)$. The magnitude and direction of a planar vector in a right-hand orthogonal system can be expressed as $Z(\omega)=R+jX$ where R is the Resistant (real part) and X is Reactance (imaginary part). The imaginary number $j=\sqrt{-1}=exp(j\pi/2)$ indicates an anticlockwise rotation by $\pi/2$ relative to the x axis. Thus, the real part of Z is along the real axis x, and the imaginary part is along the y axis which is shown in Figure 2-2. So the two rectangular coordinates values are

$$Re(Z) = R = |Z| \cos(\theta) \quad \text{and} \quad Im(Z) = X = |Z| \ \sin(\theta)$$

with the phase angle of

$$\theta = \tan^{-1}(X/R)$$

and the modulus

$$|Z| = [(R)^2 + (X)^2]^{1/2}$$
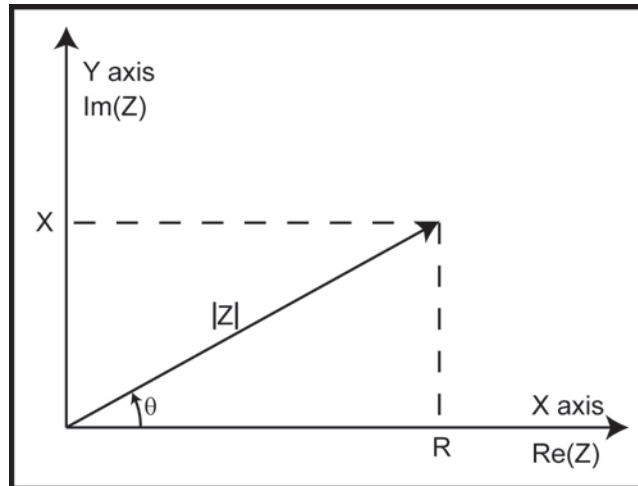
Figure 2-2-The impedance Z plotted in rectangular and polar coordinates

In the polar coordinate system Z is expressed as $Z(\omega) = |Z|\exp(j\theta)$. In general, Z is frequency-dependent, as defined above. In conventional Impedance Spectroscopy, Z will be measured over a wide range of frequencies, from which the electrical properties of the structure is derived.

The impedance of a system can be expressed in terms of two parallel Conductance (G) and Capacitance (C),

$$Z(\omega) = \frac{1}{G + j\omega C} \tag{1}$$

G represents the ability of the structure to conduct the electricity and C represents the ability to store the electricity. For a homogenous material with cross sectional are A and thickness t, the conductance and capacitance can be written as follows:

$$G = \sigma\frac{A}{t} \tag{2}$$

and

$$C = \epsilon\frac{A}{t} = \epsilon_r\epsilon_0\frac{A}{t} \tag{3}$$

where σ is the electrical conductivity, ϵ is dielectric constant (permittivity) [F/m], ϵ_r is relative dielectric constant (relative permittivity), and ϵ_0 is space permittivity (=8.854×10^{-12} [F/m]) [25-26].

2.1.2 Impedance Spectroscopy as an NDT in Thermal Spray Coatings

Impedance Spectroscopy is a very simple and popular analytical and experimental tool in material research and development. It can be used in detecting corrosions, chemical reactions and defects influences on the conductance of solids. Recently, Impedance Spectroscopy was used as a quality control procedure, non-destructive test (NDT) or in health monitoring. This method has been successfully used to evaluate failure, nucleation of cracks and defects (damage detection), oxidation and degradation of Thermal Barrier Coatings (TBC) [28-29]. Due to failure behavior of these coatings, a non-destructive evaluation is very useful. Changes in oxidation amount, crack growth and degradation can be related to the changes of resistance and capacitance by means of impedance spectroscopy.

In this study, impedance spectra of Yttria-Stabilized Zirconia (YSZ) coatings on Aluminum substrate at varying frequencies was investigated. In particular, the change of dielectric constant of YSZ coatings at different humidity levels was studied. The crack growth in YSZ coating of specimens subjected to cyclic micro-strain test was related to their dielectric constant.

2.1.3 Impedance Analyzer

In our experiments two electrodes (HP 16451B Dielectric Test Fixture) were placed at five different locations on the top and on the bottom of each sample, as shown in Figure 2-3. As the substrate is Aluminum, the actual bottom electrode is the substrate

itself. Therefore, only the characteristic and the diameter of the top electrode is important. The top electrode's diameter was 5 mm, as shown in Figure 2-3.

Before each experiment, the HP 16451B Dielectric Test Fixture was calibrated by the impedance analyzer.

A

top electrode

bottom electrode

HEWLETT PACKARD 16451B DIELECTRIC TEST FIXTURE

B

5 mm

top electrode

bottom electrode

to instrument
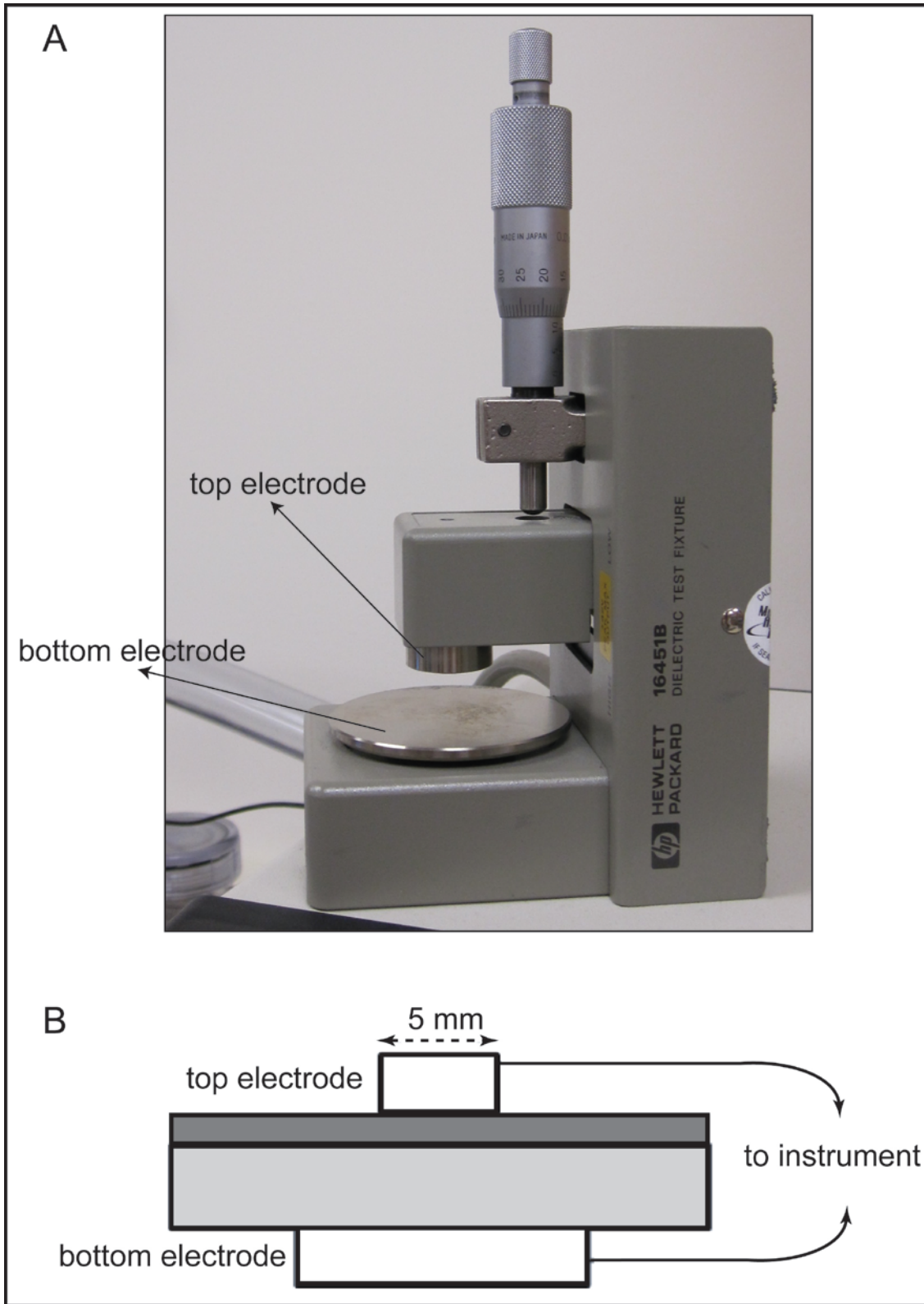
Figure 2-3-A) HP 16451B dielectric test fixture; B) Two electrodes placed on top and bottom of the coated sample

An Agilent 4294A Precision impedance analyzer with a four-terminal pair configuration which is shown in Figure 2-4, was connected to these electrodes for measuring the capacitance of the samples. The impedance analyzer frequency range and resolution are given in Table 2.
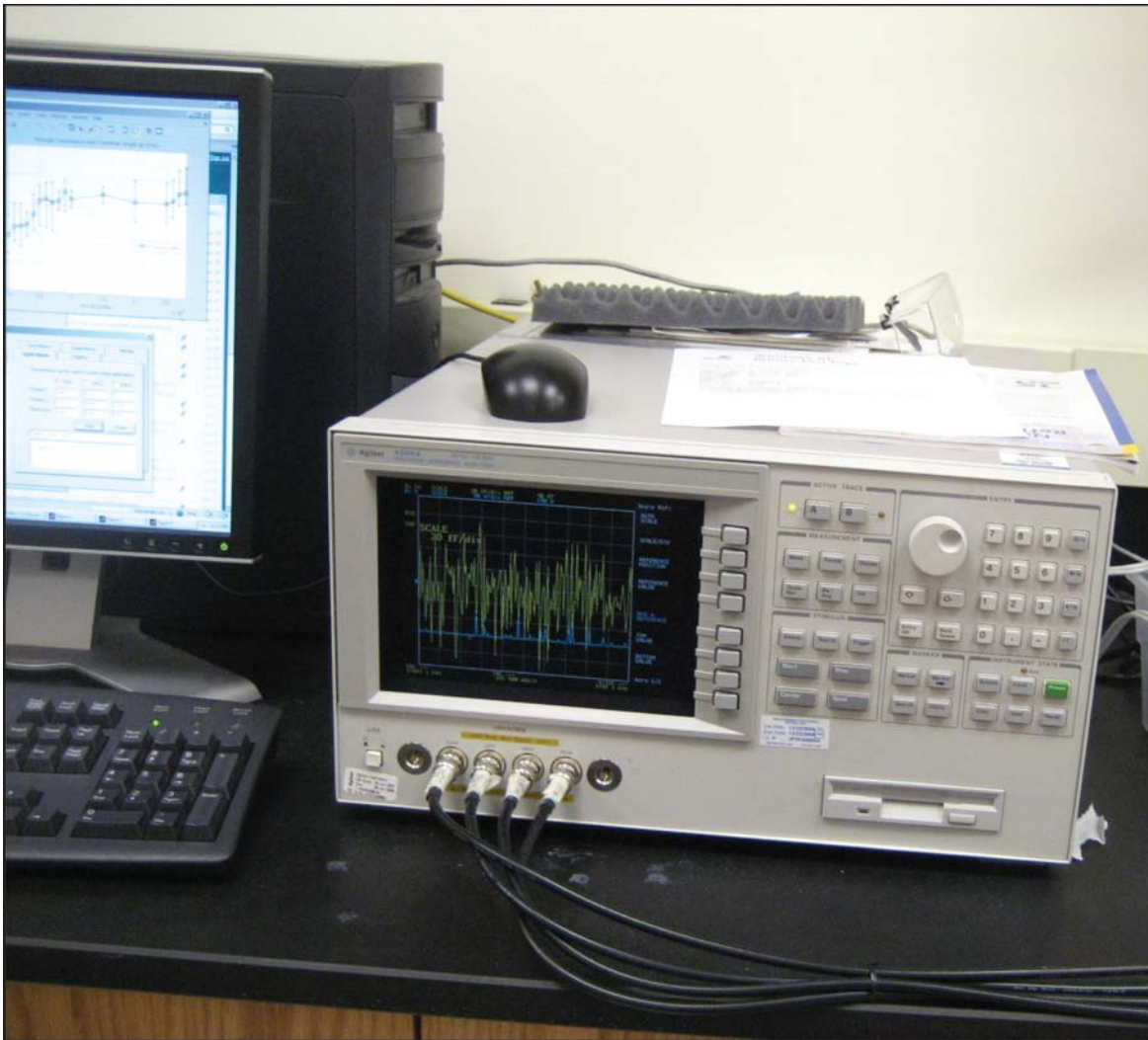
Figure 2-4-Agilent 4294A precision impedance analyzer

Table 2-Basic Characterization of Agilent 4294A Precision Impedance Analyzer

	Range	Resolution	Accuracy
Frequency	40 Hz to 110 MHz	1 mHz	± 20 ppm *(at 23 ± 5 °C)* ± 40 ppm *(at 0 to 55 °C)*
Voltage Signal Level	5 mVrms to 1 Vrms	1 mV	$\pm[(10 + 0.05 \text{ X f})\% + 1 \text{ mV}]$ *(at 23 ± 5 °C)*
Current Signal Level	200 µArms to 20 mArms	20 µA	*at ≤15 MHz* $+[10\% + 50 \text{ µA}]$ $-[(10 + 0.2 \text{ X f 2})\% + 50 \text{ µA}]$ *at >15 MHz* $\pm[(10 + 0.3 \text{ X f})\% + 50 \text{ µA}]$ *(at 23 ± 5 °C, typical)*
DC voltage bias	0 to ± 40 V	1 mV	$\pm[0.1\% + (5 + 30 \text{ X } |I_{mon}|) \text{ mV}]$ *(at 23 ± 5 °C)* $\pm[0.2\% + (10 + 30 \text{ X } |I_{mon}|) \text{ mV}]$ *(beyond 23 ± 5 °C)*
DC current bias	0 to ± 100 mA	40 µA	$\pm[2\% + (0.2 + |V_{mon}|/20) \text{ mA}]$ *(at 23 ± 5 °C)* $\pm[4\% + (0.4 + |V_{mon}|/20) \text{ mA}]$ *(beyond 23 ± 5 °C)*

All of this data belongs to the four-terminal pair port of the Agilent 4294A which is shown in Figure 2-5. The capacitance was measured at different frequencies and as the capacitance had almost the same behavior during fatigue test, the frequency was fixed to 1KHz. More results will be discussed further in Chapter 4 of this manuscript.
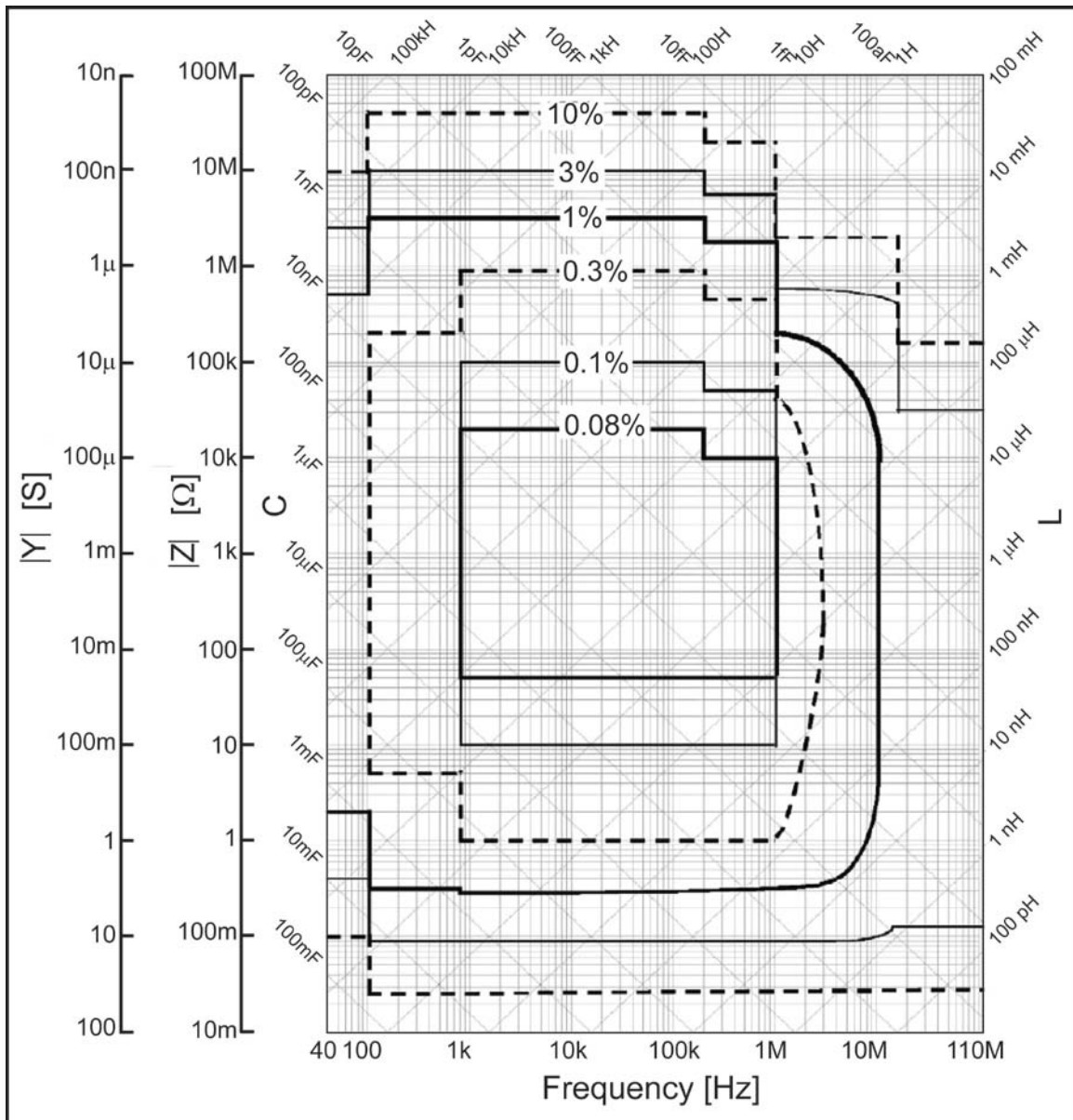
Figure 2-5-Calculated impedance measurement accuracy at four-terminal pair port of the Agilent 4294A's front panel (oscillator level=0.5 Vrms)

It's much more convenient to work with dielectric constant instead of capacitance, therefore, the measured capacitance was converted to dielectric constant by

$$\epsilon_r = \frac{t \times C_p}{\pi \times \left(\frac{d}{2}\right)^2 \times \epsilon_o}$$

(4)

where ϵ_r is relative dielectric constant (relative permittivity), t is average coating thickness [m], C_p is equivalent parallel capacitance value [F], d is diameter of electrode [m] and ϵ_o is space permittivity which is equal to 8.854×10^{-12} [F/m].

2.2 Cantilever Beam Structure

The experimental substrate that was used has a varying cross sectional area as shown in Figure 2-6, to have a constant strain, over the beam length. One end of the cantilever was fixed and the other end had a deflection of δ.
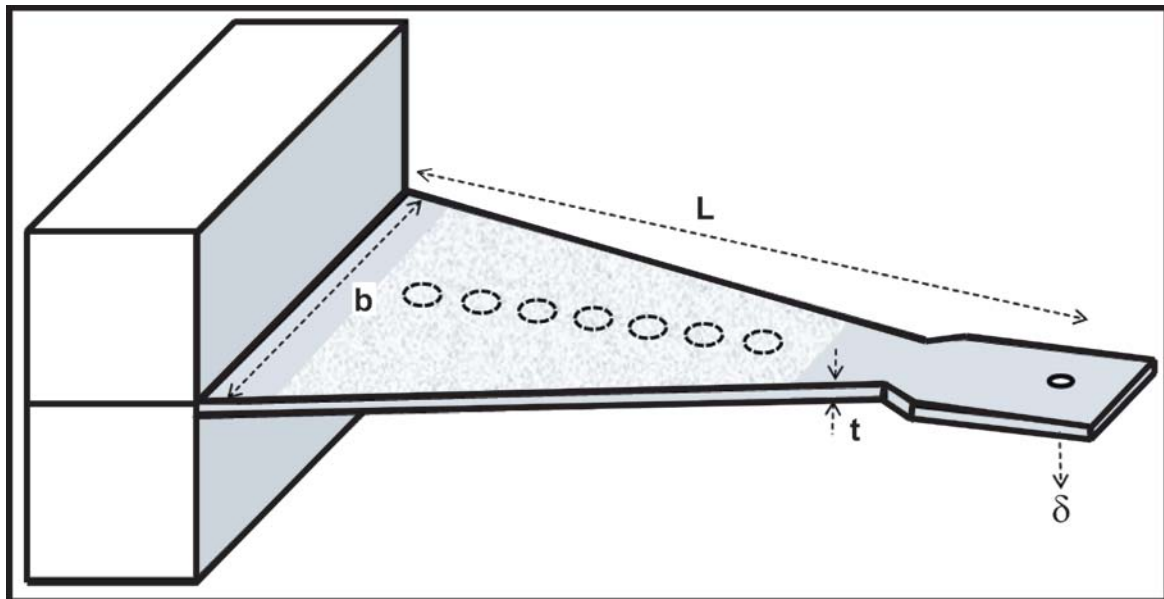
Figure 2-6-Substrate with coating

2.2.1 Constant Strain Concept in a Varying Cross-Sectional Area Cantilever Beam

It was assumed that strain in the relatively thin coating was equal to substrate surface strain. The relation between the deflection of the end of cantilever beam (δ) and strain (ε) was calculated. The stress in a cantilever beam under a torque is equal to

$$\sigma_x = \frac{M_x y}{I} \tag{5}$$

The torque and moment of inertia of the cantilever beam of Figure 2-6 can be written as

$$M_x = F(L - x) \tag{6}$$

$$I = \frac{1}{12} \times \frac{b}{L}(L - x)t^3 \tag{7}$$

So by using equations 2, 3 and 4 we can relate the stress to the applied force as bellow

$$\sigma_x = \frac{F(L - x)\,{}^t\!/_2}{\frac{1}{12} \times \frac{b}{L}(L - x)t^3} = \frac{6FL}{bt^2} \tag{8}$$

and strain has the following relation with the stress,

$$\varepsilon = \frac{\sigma_x}{E} = \frac{6FL}{Ebt^2} \tag{9}$$

From beam theory, we have

$$EI \frac{\partial^2 v}{\partial x^2} = M_x \tag{10}$$

So

$$E \times \frac{1}{12} \times \frac{b}{L}(L-x)t^3 \times \frac{\partial^2 v}{\partial x^2} = F(L-x)$$

$$\Rightarrow \quad \frac{\partial^2 v}{\partial x^2} = \frac{12FL}{Ebt^3}$$

$$\Rightarrow \quad \frac{\partial v}{\partial x} = \frac{12FL}{Ebt^3}x + c_1$$

$$\Rightarrow \quad v = \frac{6FL}{Ebt^3}x^2 + c_1 x + c_2 \tag{11}$$

considering boundary conditions, we have:

$$\frac{\partial v}{\partial x} = 0 \quad at \quad x = 0 \quad \Rightarrow \quad \frac{12FL}{Ebt^3}x + c_1 = 0$$

$$\Rightarrow c_1 = 0$$

$$v = 0 \text{ at } x = 0 \quad and \quad c_1 = 0 \quad \Rightarrow \quad \frac{6FL}{Ebt^3}x^2 + c_2$$

$$\Rightarrow \quad c_2 = 0$$

Therefore

$$\delta = v(L) = \frac{6FL^3}{Ebt^3} \tag{12}$$

and

$$F = \frac{Ebt^3\delta}{6L^3} \tag{13}$$

Substituting F from equation 13 in the strain relationship of equations 9, we will have

$$\varepsilon = \frac{\delta t}{L^2} \tag{14}$$

So the strain is constant over the length of the cantilever beam and has a linear relationship with end deflection of the beam (δ). The cantilever beam dimensions are shown in Figure 2-7. The length of the beam was L=16.16 cm, and the thickness was t=2.7mm. If we used these dimensions in equation (8), we can find the maximum deflection of the beam from equation 14.

$$\delta = \frac{\varepsilon L^2}{t} = \frac{0.001 \times (0.1616)^2}{0.0027} = 9.7 \; mm \tag{15}$$

The strain was changing from 0 to 0.1% tension (R=0) by using a Zaber NA14B60 actuator.
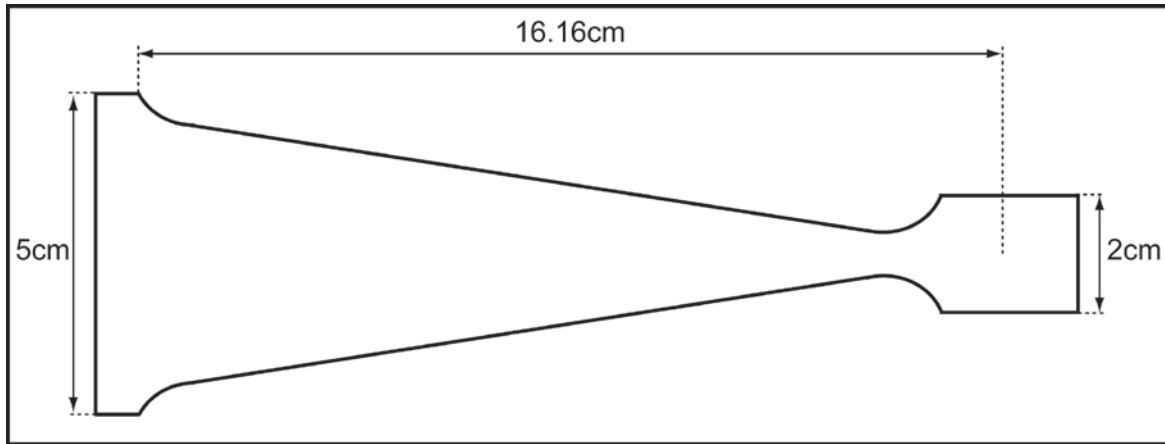
Figure 2-7-Dimensions of the cantilever beam

2.2.2 Actuator

A Zaber NA14B60 actuator which is shown in Figure 2-8 was used in our experiments. Its specification are shown in Table 3. This actuator was programmed to move specific amount of distance from a specific point.

Table 3-Zaber NA14B60 Actuator specification

Microstep Size (Default Resolution)	0.09525 µm
Microstep Size (Finest Resolution)	0.047625 µm
Travel Range	60 mm
Accuracy	+/- 15 µm
Repeatability	< 2 µm
Backlash	< 18 µm
Speed Resolution	0.000893 mm/s
Maximum Speed	10 mm/s
Maximum Continuous Thrust	225 N
Motor Temperature Rise	75 degree C
Linear Motion Per Motor Rev	1.2192 mm
Motor Steps Per Rev	200
Motor Rated Current	570 mA/phase
Motor Winding Resistance	8.8 ohms/phase

Figure 2-8-Zaber NA14B60 actuator

Each microstep size of this actuator is about 0.09525µm by default based on Table 3. As it was calculated, 9.7mm displacement is necessary for having 0.1% strain in the cantilever beam, which is equal to 101837 microstep in each half cycle. The speed of the fatigue test was set to be quasi static (around 30 cycles/min).

All of the experimental setup was placed inside a glove box to keep the humidity of test environment constant which is shown in Figure 2-9.
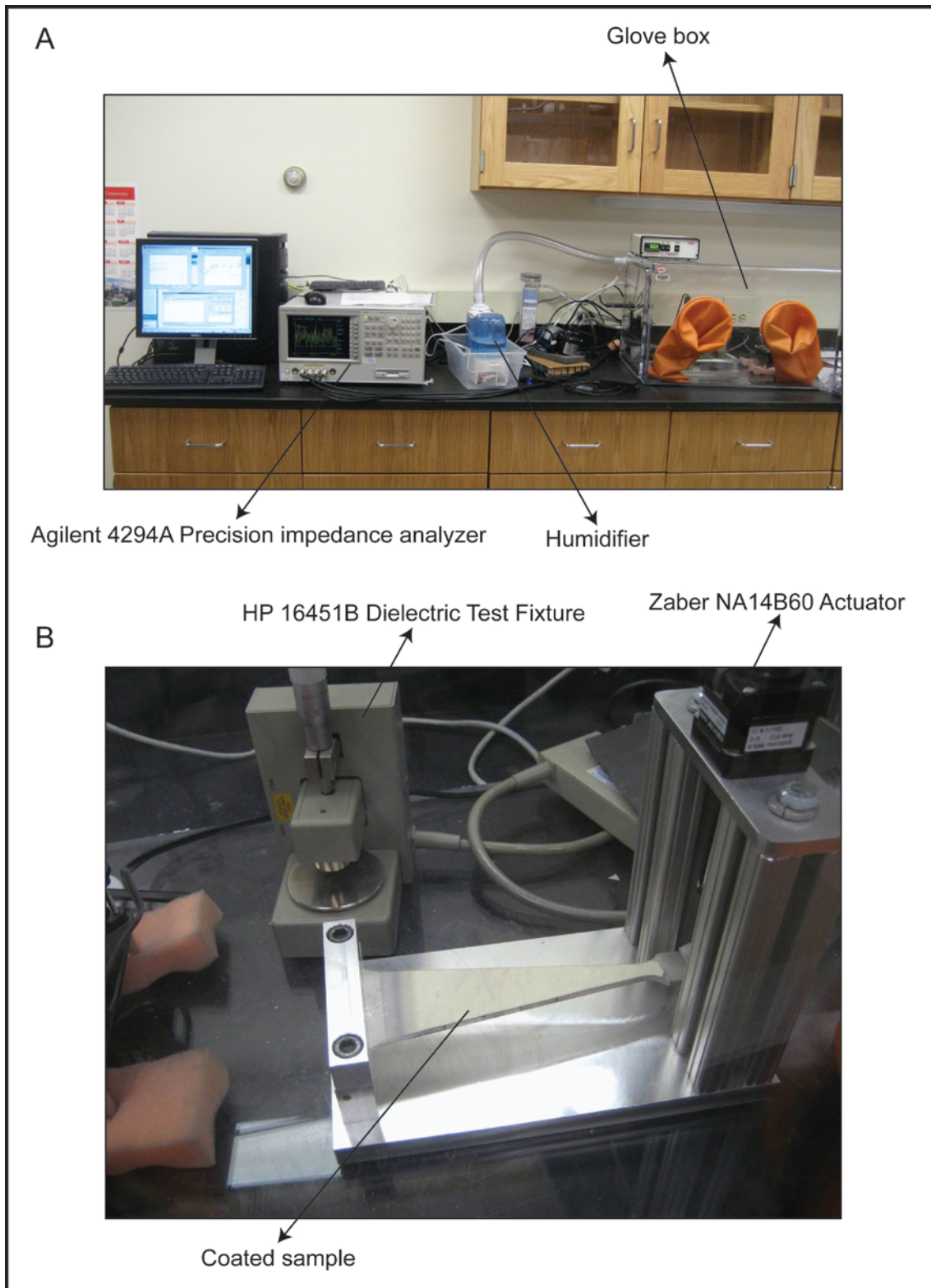
Figure 2-9-A) Experimental setup; B) Cantilever beam and Zaber NA14B60 actuator

2.3 Effect of Humidity on Electrical Measurement of Samples

Relative dielectric constant of Zirconia is about 22 but coating is very porous due to cracks which are filled with air and humidity (water) with relative dielectric constant of 1 and 80 respectively. Therefore, the amount of humidity has a significant effect on the measured dielectric constant and it should be kept constant during the experiments.

2.3.1 Humidifier

A controlled environmental chamber (Model 5503-11 with package D) from Electro-Tech Systems, Inc. was used to keep the humidity constant which is shown in Figure 2-10. This system was capable of changing the humidity from 5% to 100% RH. It consisted of a chamber with glove ports and a ETS Model 5100-240 Microprocessor Humidity controller in conjunction with the Model 5461 Dehumidification System and Model 5462 Ultrasonic Humidification System.

A Model 554 Humidity Sensor was used to measure the humidity level inside the chamber with an accuracy better than ±2%.The operating range of the sensor was -40 to 85ºC. The specification of the humidity sensor is summarized in Table 4.

Table 4-Model 554 Humidity sensor of Electro-Tech Systems (ETS) specifications

Humidity	Capacitive film
Range	0-100% (10mV/%RH)
Accuracy	±2% RH at 23ºC
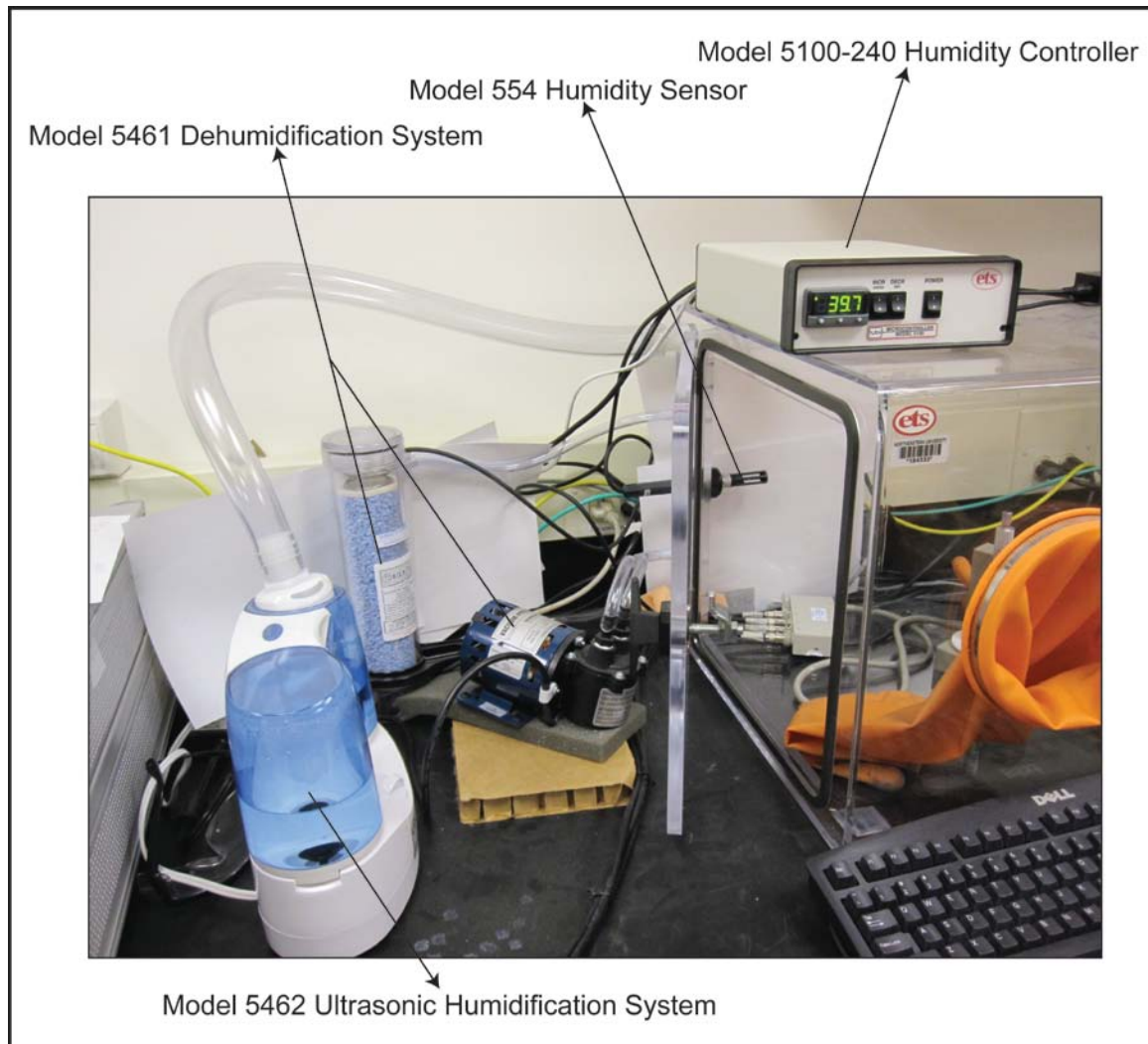
Figure 2-10-Controlled environment chamber Model 5503-11 with package D of Electro-Tech Systems (ETS) for keeping the humidity constant

The controller Model 5100-240 was used to control the level of humidity. It constantly monitored humidity and pulse the humidifier or dehumidifier to maintain the humidity at the set point, and it was capable of maintaining humidity at ±0.2 of the assigned humidity. The controller specifications is summarized in Table 5.

Table 5-Controller Model 5100-240 of Electro-Tech Systems (ETS) specifications

Sensor input (std linear)	0-1.0V
Accuracy	±0.5%
Resolution	±0.1 of digital readout
Calibration accuracy	±0.25% (max input)
Sampling frequency	10 Hz, CJC - 2 sec

The Dehumidification system (model 5461) used a pump to draw air from the chamber and circulate it through a plastic cylinder that contains calcium sulfate which absorbs any moisture that is in the air. The dried air was then forced back into the chamber.

The model 5432 Humidification System produced a fine mist by using an ultrasonic transducer. A small fan built in the humidifier forced the mist out of the humidifier through a plastic tube and into the chamber.

2.3.2 Change of Capacitance and Dielectric Constant Versus Humidity

As it was discussed before, relative dielectric constant of the coating is changing due to humidity because of the porosity amount and cracks inside the coating. The changes of capacitance and relative dielectric constant consequently versus humidity change are shown in Figure 2-11. As it is shown, the overall capacitance is increasing because of penetration of water molecules with dielectric constant of 80 and replacing the air with dielectric constant of 1 inside the porous coating.
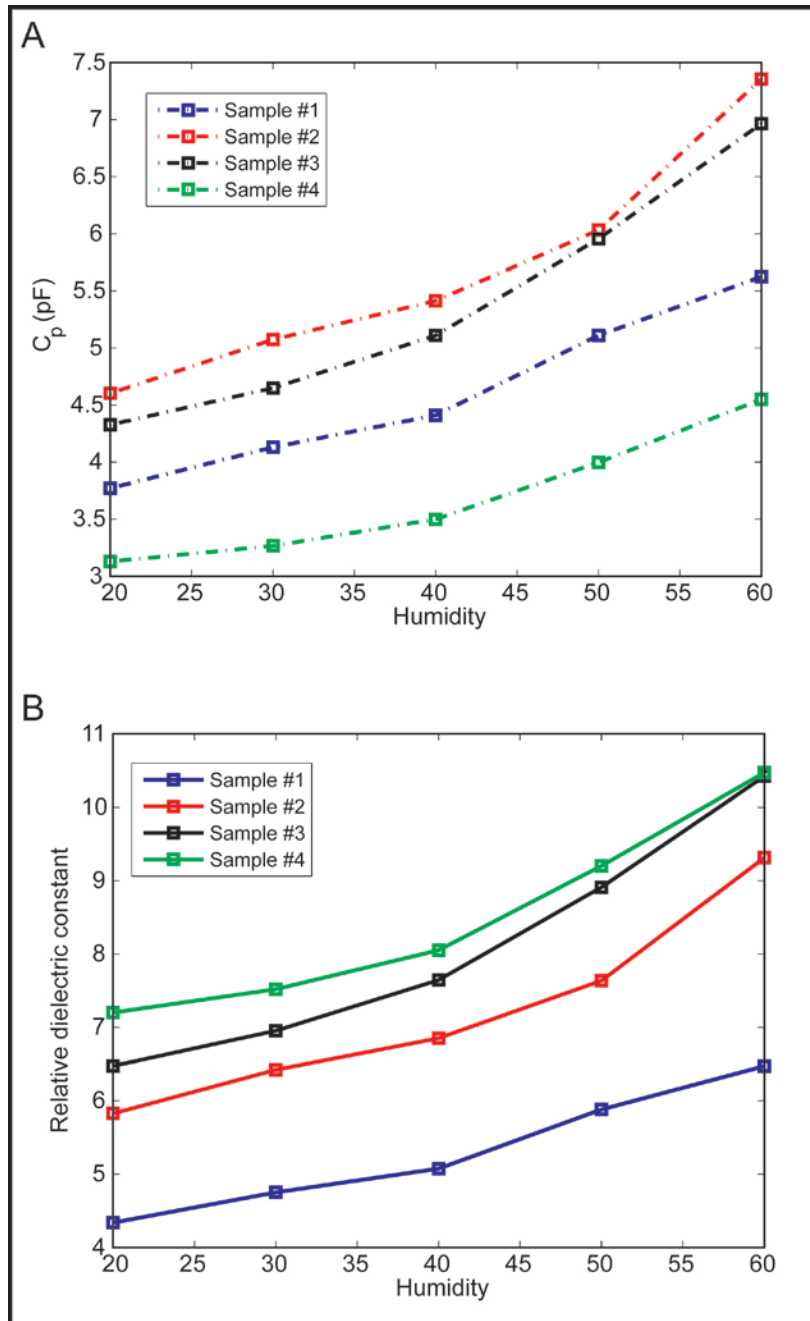
Figure 2-11-A) Capacitance versus humidity; B) Relative dielectric constant versus humidity

Samples should be placed in a constant humidity environment for at least 100 minutes to let the humidity fill the porosities of the coating. To examine the penetration time of water into the porous coating, the samples were placed in the glove box at fixed

humidity of 80%. The capacitance was showing an asymptotic behavior till it converged to a specific amount. The change of dielectric constant versus time at 80% humidity and 1kHz sampling rate (for sample #124) is shown in Figure 2-12.
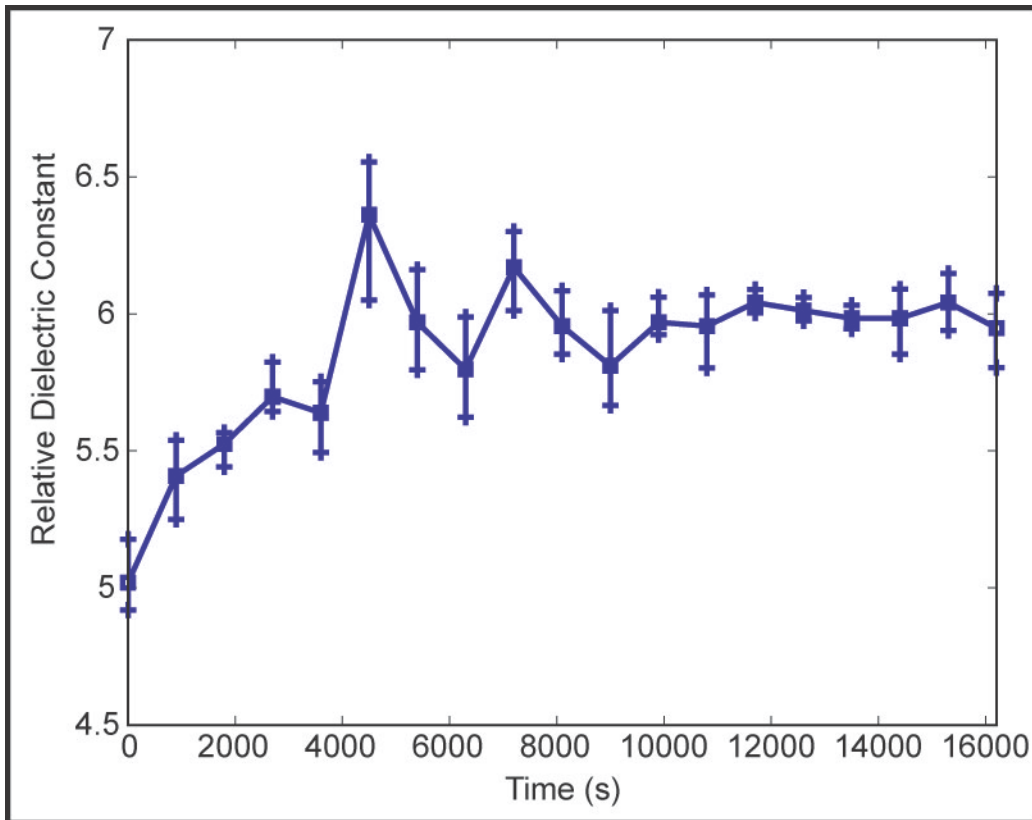
Figure 2-12-Relative dielectric constant vs. time at 80% humidity and 1kHz

The relative dielectric constant vs. time at 50% humidity was measured too which is shown in Figure 2-13. As it is shown the amount of change is smaller, and we have the plateau surface much sooner than the 80% case.
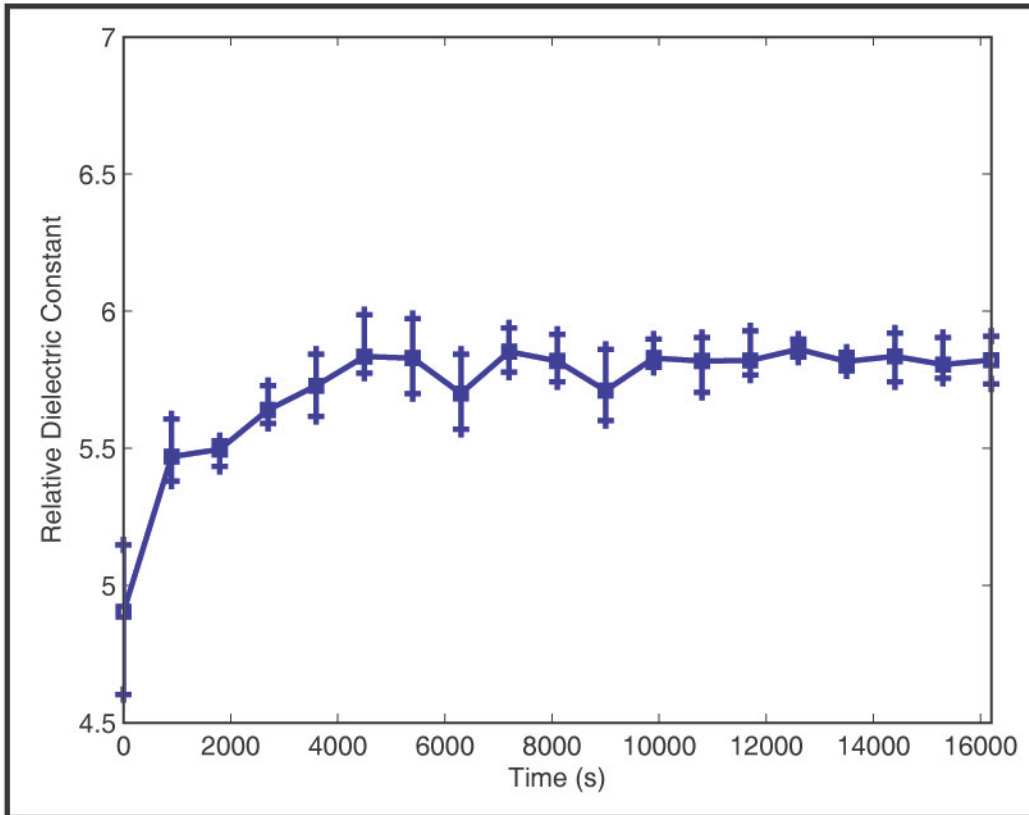
Figure 2-13-Relative dielectric constant vs. time at 50% humidity and 1kHz

For better understanding the penetration of the humidity inside the coating, the surface of the above sample was covered with a protective, waterproof paint. All of the top surface was covered except a small location for placing the top electrode. The sample was placed inside the glove at humidity of 80% and its capacitance and dielectric constant was measured. As it is shown in Figure 2-14, the dielectric constant of the sample was remain almost constant during the time. This experiment confirms the penetration of water particles into the available porosity and cracks inside the coating.
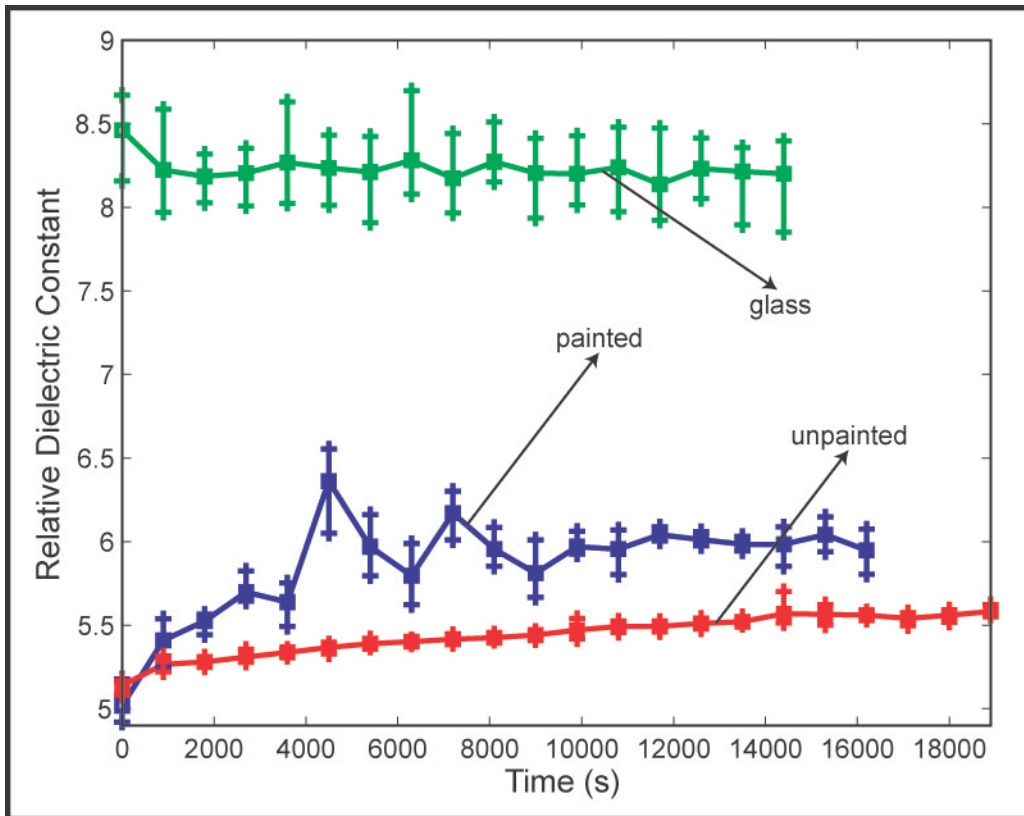
Figure 2-14-Relative dielectric constant vs. time at 80% humidity and 1kHz for a painted and unpainted coating and a glass sample

The dielectric constant was measured for a glass sample too. The results for humidity versus time are shown in Figure 2-14 too. As it is shown, the dielectric constant is not changing because glass does not have a porous structure like thermal spray coatings. Therefore, humidity is not penetrating the microstructure of it.

Each coated substrate was placed in a glove box and maintained at 50% relative humidity for at least 100 minutes, and it remained constant for all subsequent tests and measurements. Coatings were then strained in-plane by bending the cantilever substrates on a custom-built apparatus which is shown in Figure 2-9B.

2.4 Sampling Frequency

The sampling frequency is an important factor and it should be kept constant during the experiments. The dielectric constant versus sampling frequency is shown in Figure 2-15.
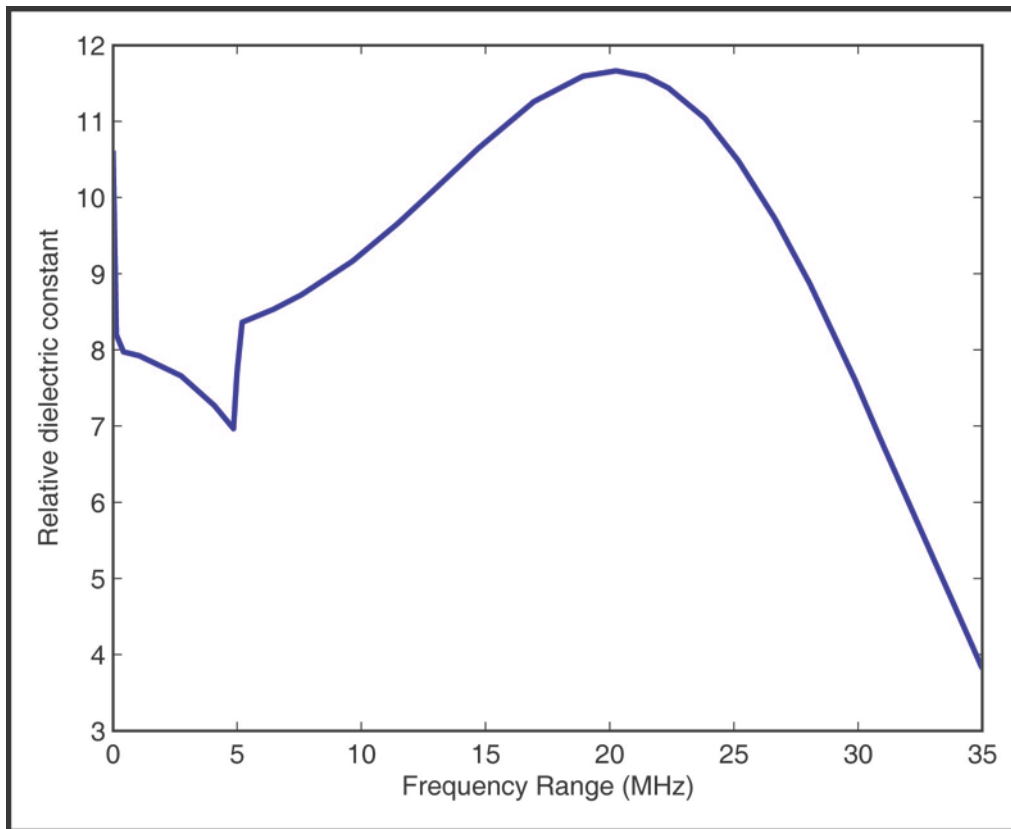
Figure 2-15-Relative dielectric constant versus sampling frequency

Although the relative dielectric constant is highly dependent on the sampling frequency, the asymptotic behavior of it versus the number of cycles in the fatigue test is not changing. As it is shown in Figure 2-16, for all sampling frequency, the dielectric

constant is increasing till it reach a plateau which is like the 1KHz sampling frequency case.
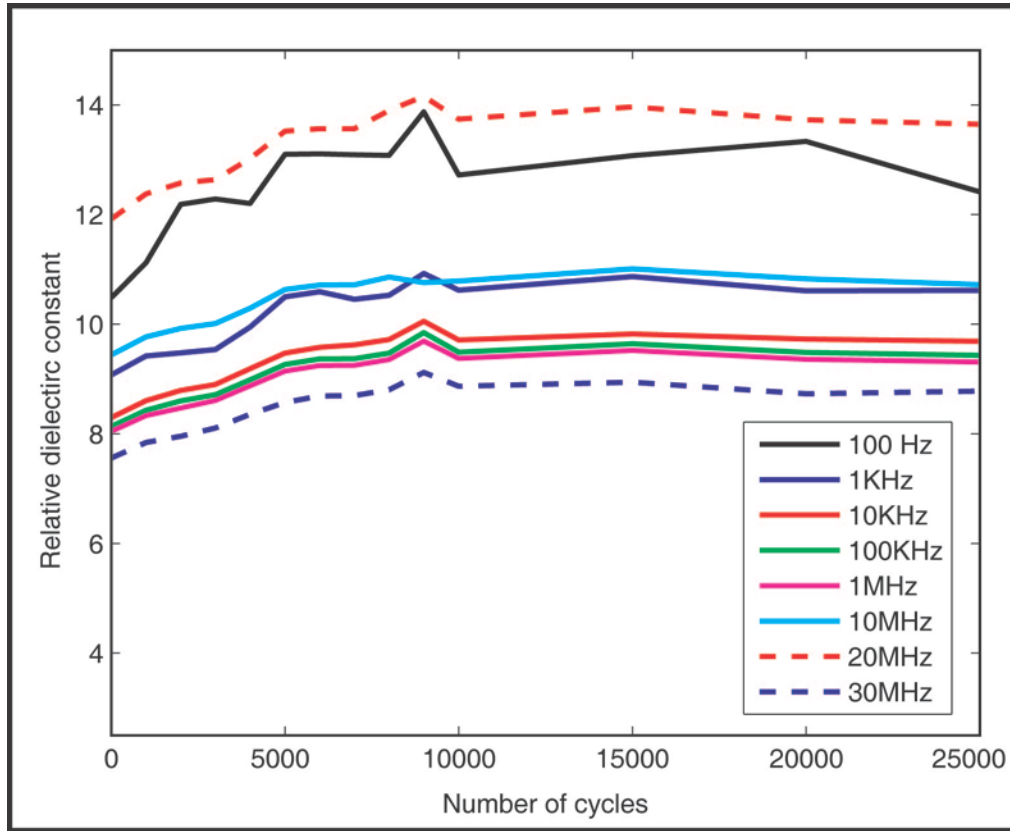
Figure 2-16-Asymptotic behavior of dielectric constant versus number of cycles for different sampling frequencies

As it is shown in all cases and for all sampling frequencies, the asymptotic behavior is repeated.

2.5 Conclusion

The humidity should be fixed in the whole experiment procedure time. Every sample should be placed in the glove box for more than 10000 seconds (≈160 minutes) to

make sure that the dielectric constant is not changing due to the humidity. The sampling frequency is an important factor in measuring the dielectric constant but it does not change the overall asymptotic behavior of the dielectric constant under fatigue test. By increasing the amount of strain, the dielectric constant increases and then approaches a constant value again.

CHAPTER 3. Modeling of Stable Crack Growth in Thermal Spray Thick Coatings Detected by Capacitance Measurements

3.1 **Abstract**

The goal of this research is to understand the fatigue behavior and microstructure changes of thermal spray coatings under low strain cycling. Results showed a significant increase in relative dielectric constant of thermal sprayed coatings under tension (R=0) which is due to the growth of micro-scale pre-existing cracks. Yttria-Stabilized Zirconia (YSZ) were deposited on tapered cantilever beam substrates to provide constant in-plane cyclic strains. Relative dielectric constant of coatings was measured via impedance spectroscopy. A Finite Element (FE) model of a randomly distributed network of crack pairs under a Paris law type stable crack growth was used to model the growth of micro-scale pre-existing cracks in coatings. Experiments confirm growth of micro-cracks in thermal spray coatings which are in good comparison with Finite Element (FE) models.

3.2 **Introduction**

Thermal Spraying technique is a coating process in which the molten particles of coating material are sprayed onto a substrate. The coating material is heated by electrical (plasma) or chemical (combustion flame) means. Thermal spraying can provide thick coatings over a large area of substrate. Coatings' fed are in the form of powder and they will be heated to a molten or semi-molten state and accelerated toward the substrates in the form of molten particles (splats). The speed of the molten splats vary from 50 to 200 m/s for different coating setups. Coating layer is made of accumulation of numerous amount of these splats [1].

Coatings are widely used to insulate and protect hot-section metal components in advanced gas-turbines (aircrafts and power generations) and diesel engines for propulsion and power generation. By lowering the temperature of substrate, coatings can improve the durability of the metal components and enhancing engine performance [2-5]. TS is attractive for these systems due to its low cost, ability to coat large areas and flexibility in material feedstock. These attributes, along with improvements in process diagnostics have spurred the exploration of TS for more functional applications including fuel cells [6], electronic sensors [7] and biomedical implants [8]. Successful usage of TS coatings in these systems will require more robust characterization of their mechanical behavior; which has been limited till now [9].

The microstructure of TS coatings includes layers of micron-thick flattened particles ('splats') separated by interfaces, the bonding between which is not well understood [10-11, 30]. These interfaces represent potential crack growth sites throughout the material. Generally, a thermal sprayed coating has many local micro-cracks inside, because the coating is a porous material and it is coated on a rough surface which has a blasting treatment [12]. The micro-cracks behavior has been discussed in [13-15], and for ceramics in [16-20] and for composites in [21-22].

Little is known about the intrinsic or progressive behavior of the coatings under repeated loading. In most conventional tests, a machining procedure is needed for observation of the behavior of short-cracks which introduce further defects in the structure. Impedance Spectroscopy (IS) has been widely used to measure the electrical properties of materials and electrochemical behaviors. Impedance Spectroscopy (IS) of coatings reflect changes in thickness, porosity, and cracks' length of the coating [5].

During impedance measurements, an electrode is placed on the top surface of coated sample with a metal substrate as the other electrode. An electric field with varying frequency is applied to the electrodes. Therefore, the electrical response from different layers of the coating can be separated in the impedance spectra and the microstructure of coating can be correlated to the impedance spectroscopy (IS) parameters. Changes in the microstructure (i.e. micro-cracks, porosity, etc) lead to changes of electrical properties and thereby causes variations of the impedance spectra output (i.e. capacitance, relative dielectric constant, etc) [5]. Therefore, the micro-structural changes of coating during a fatigue test can be monitored with IS.

3.3 **Method**

Thermal spray coating is a porous material consisting of a lot of cracks with possible crack growth planes in splat interfaces. The coating material is considered to be weaker in these directions because of the poor bonding phenomena between coating layers. An schematic thermal spray coating material consisting of cracks and porosity is shown in Figure 3-1.

It has been considered that the cracks are generated in these interfaces and they will make interactions between each other. The interaction of cracks has been investigated in literature [31-40]. It has been shown that the stress intensity factor of cracks will increase significantly when two crack tips are close to each other and will decrease when the two crack tips will pass each other [33, 41-42].
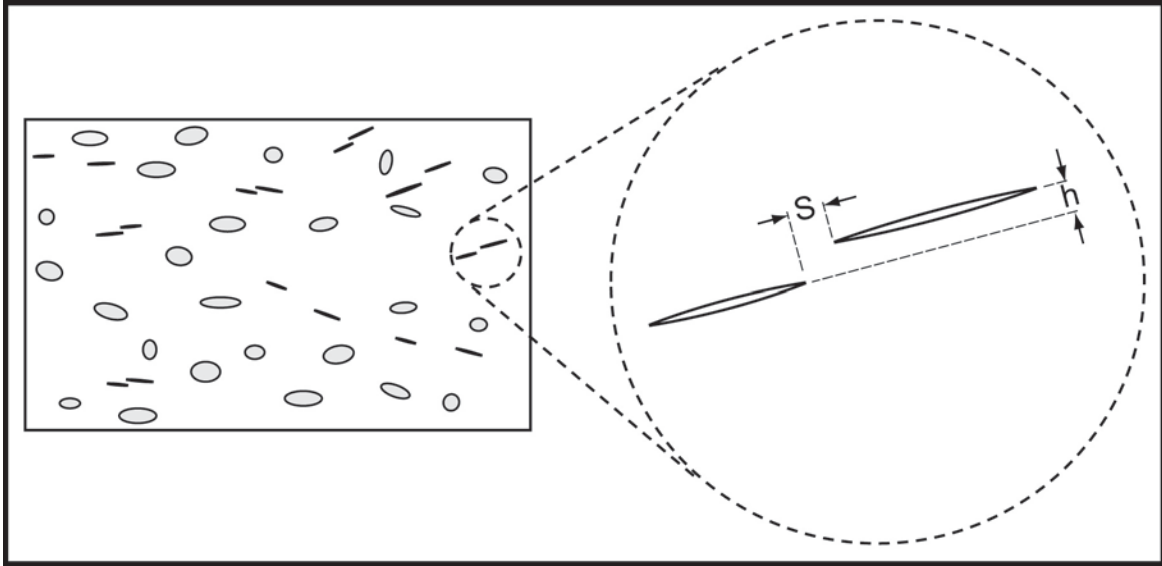
Figure 3-1-A schematic coating material consisting of a lot of cracks and porosity

A finite element model of a pair of cracks was considered in commercial finite element software of ANSYS Multiphysics 11.0 (ANSYS, Inc., Canonsburg, PA, USA) to model the crack growth behavior in thermal spray coating. One pair of parallel cracks with different length of L and a were considered in Finite Element model which is shown in Figure 3-2. The vertical distance of these cracks was assumed to be h and the horizontal distance of the crack tips B and C was assumed to be S.
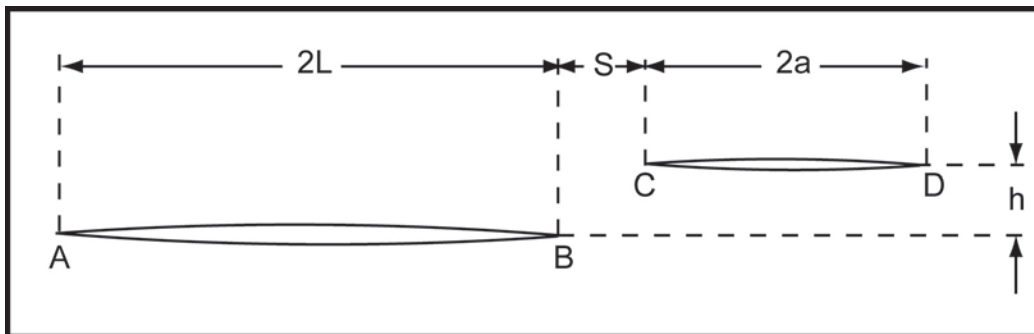
Figure 3-2-Two parallel cracks with different length

The model was meshed by Plane82 elements in ANSYS with plane strain conditions in a 2-dimensional model. The meshing is shown in Figure 3-3. As it is shown, there is a mesh concentration around each crack tip to increase the accuracy of calculating the stress intensity factor. The Poisson's ratio was assigned to be 0.3. Elastic modulus was assigned to be 30 GPa which is around the modulus of bulk material of Zirconia. The change of the material is not important if we keep the stress of the far field constant. As it is known for a single crack in plate is equal to

$$K = \sigma\sqrt{\pi a} \qquad (16)$$

which depends only on stress and the crack length. The assigned stress was equal to $0.001 \times E$ which is 0.1% strain.
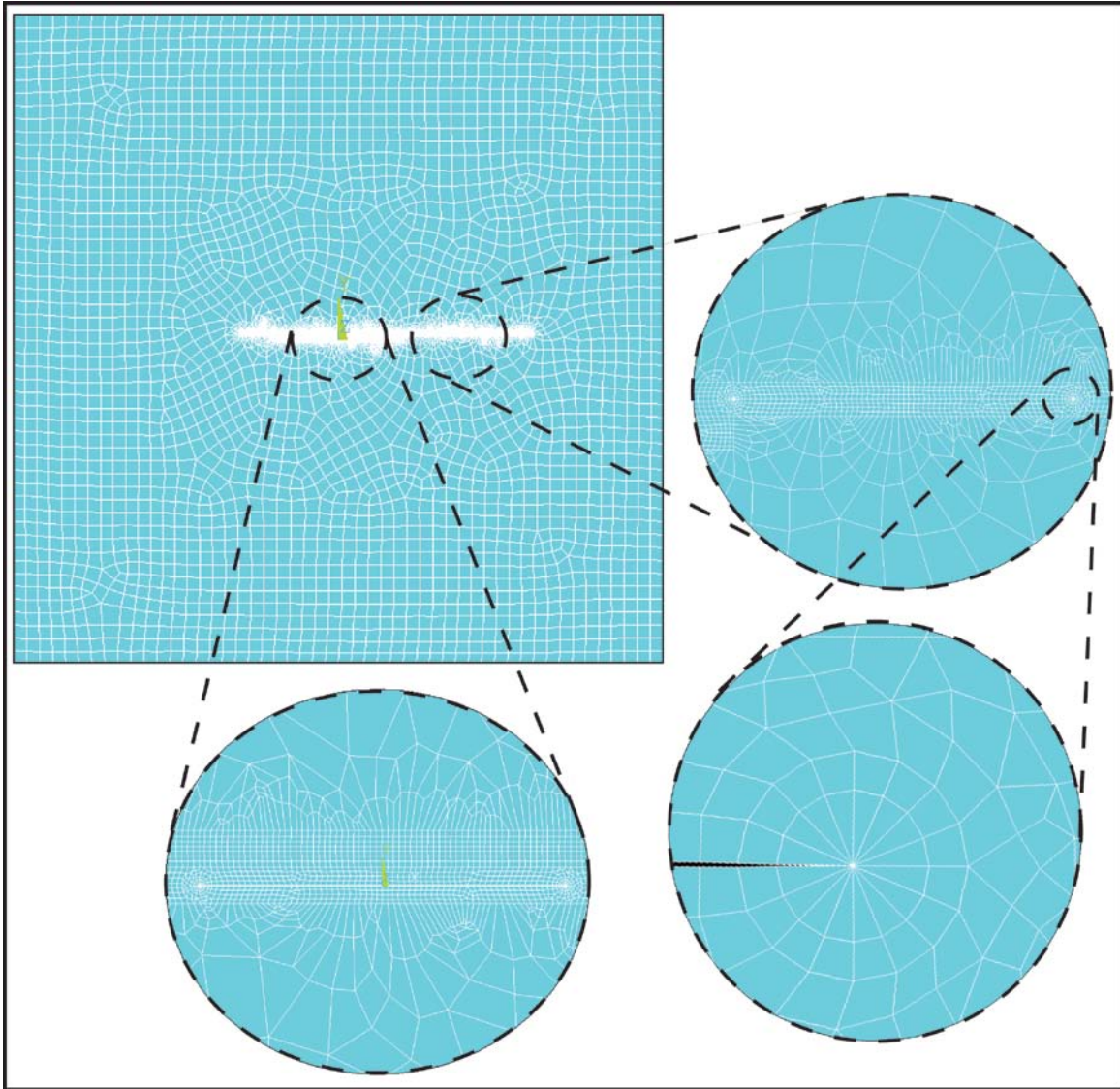
Figure 3-3-Meshing of cracks in ANSYS model

These two different applied boundary conditions are shown in Figure 3-4. By considering these two boundary conditions, all different loading conditions will be covered.
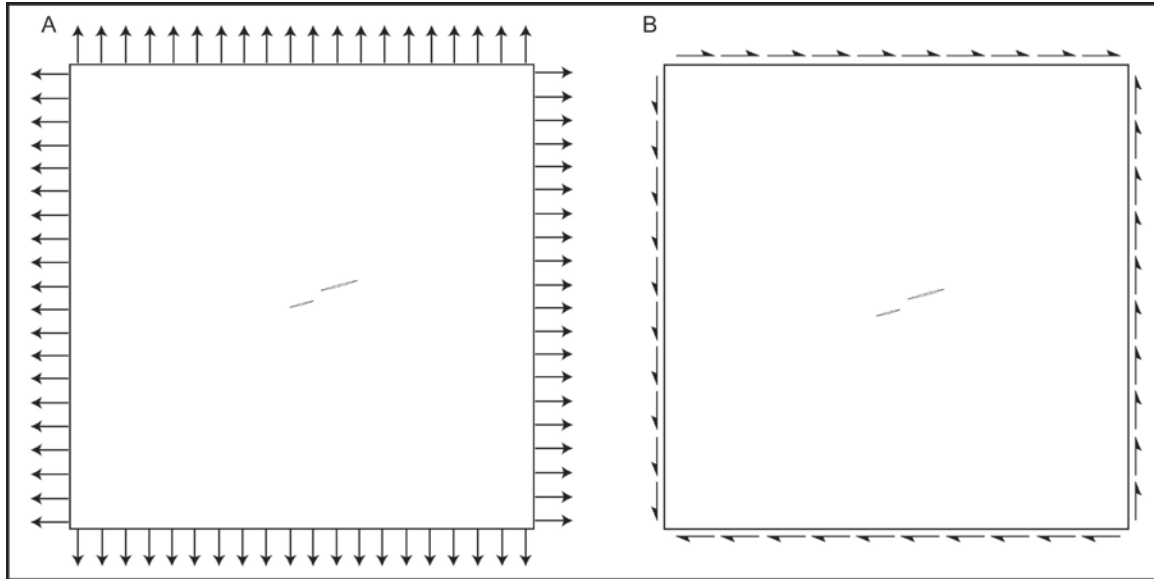
Figure 3-4- Different applied boundary conditions A) tension; B) shear

The stress intensity factor (SIF) was measured in ANSYS which use the displacement correlation technique to calculate it [43]. The vertical distance of the two cracks h was fixed to a0/10 (the initial crack length/10). The Stress Intensity Factor (SIF) of the first mode (K_I) was calculated for different crack lengths to imitate the crack growth behavior. The von-Misses stress distribution around crack tips is shown in Figure 3-5. As it is shown, when two cracks are close to each other, the maximum stress is higher.
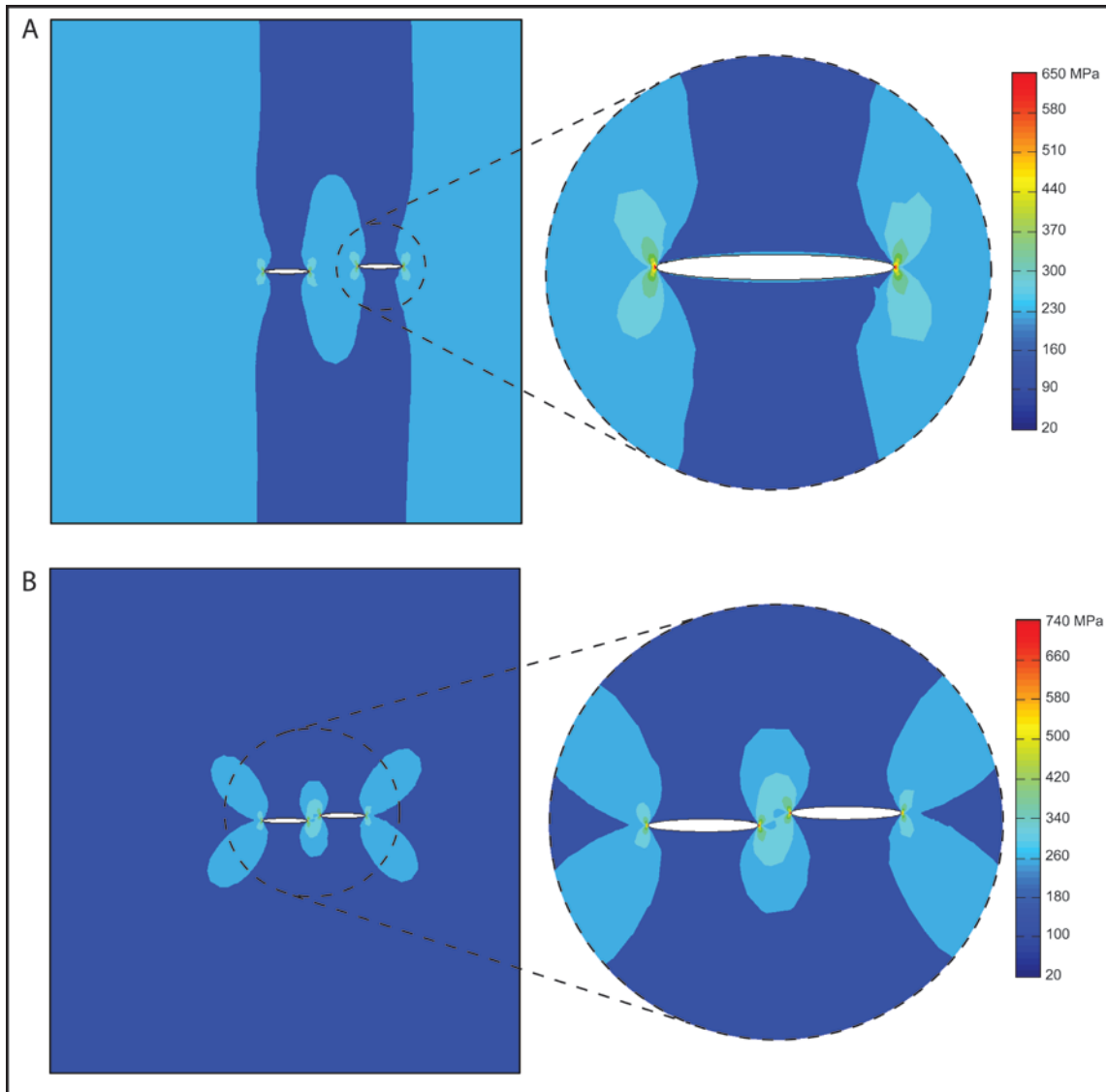
Figure 3-5- Von-Misses stress distribution of A) two far parallel crack pair; B) two close parallel crack pair under tension stress

The results for K_I and K_{II} versus different crack tips distance, S, for the inner crack tip "B" is shown in Figure 3-6. The results show a significant increase in Stress Intensity factor when two crack tips reach each other (S=0), for all orientations (10, 15 and 20 degree cracks). There is a huge drop in Stress Intensity Factor when two inner tips pass each other.
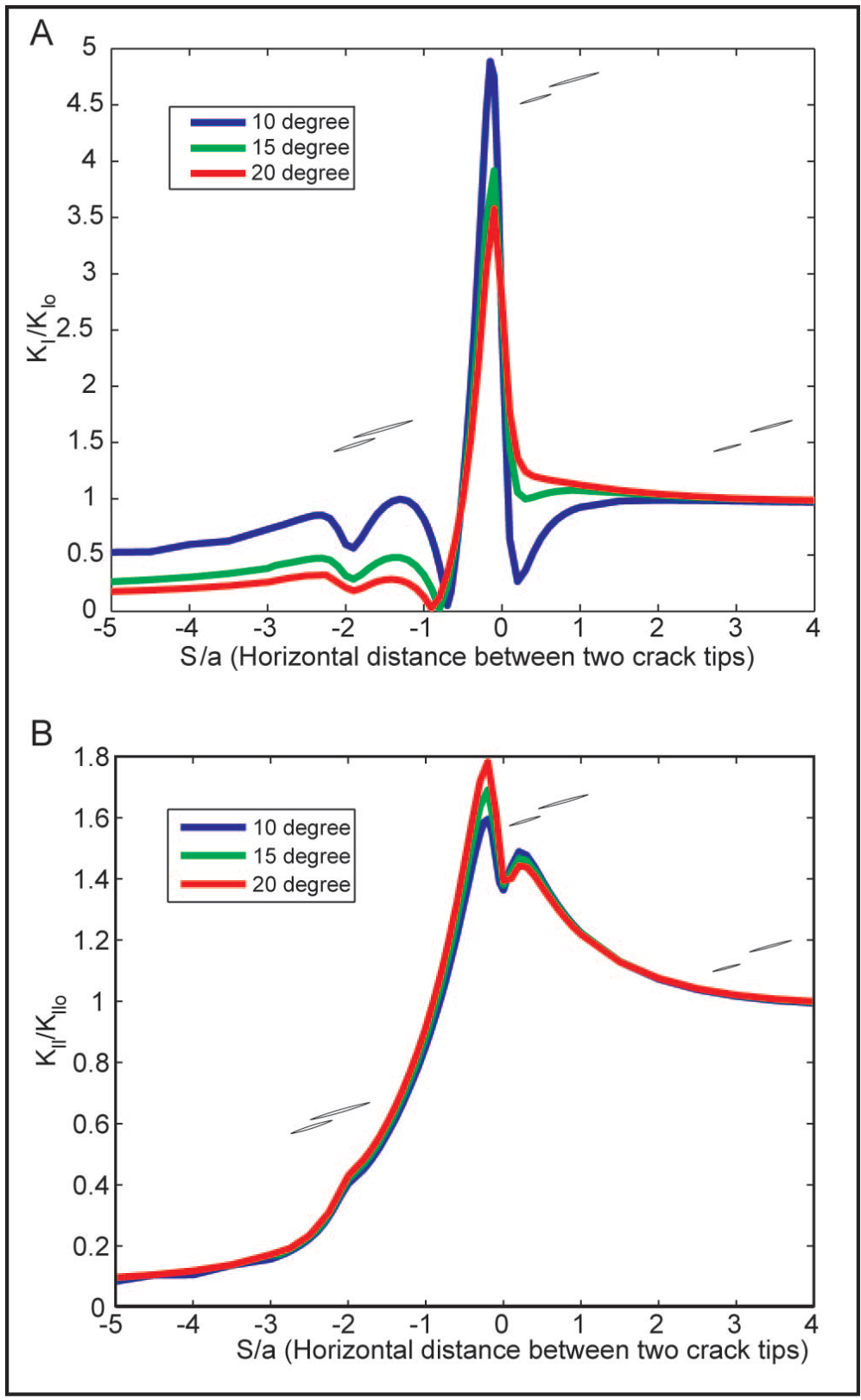
Figure 3-6-Stress Intensity Factor (SIF) of (A) the first mode, K_I (B) the second mode, K_{II} versus horizontal crack tip distance S

In most isotropic materials, the two cracks will approach each other and coalesce when their two inner tips are close to each other ($S=0$). As it was discussed before, the splats' interface represent a potential crack growth site which allows cracks to propagate parallel to each other instead of coalescing. Thermal spray coating is not isotropic and it is stronger in one direction (perpendicular to cracks) and weaker in the other direction (parallel to cracks). Stress intensity factor is the main driving force for crack propagation based on Paris Law [13, 15]. The relation between the change of crack length and stress intensity factor is

$$da = C(\Delta K)^m \tag{17}$$

where a is the crack length, C and m are material properties and ΔK is the change of stress intensity factor. The cracks were assumed to be in region II of the Paris law which is shown in Figure 3-7. The stress intensity factor of each crack must be more than a threshold amount (ΔK_{th}) to start the growth.
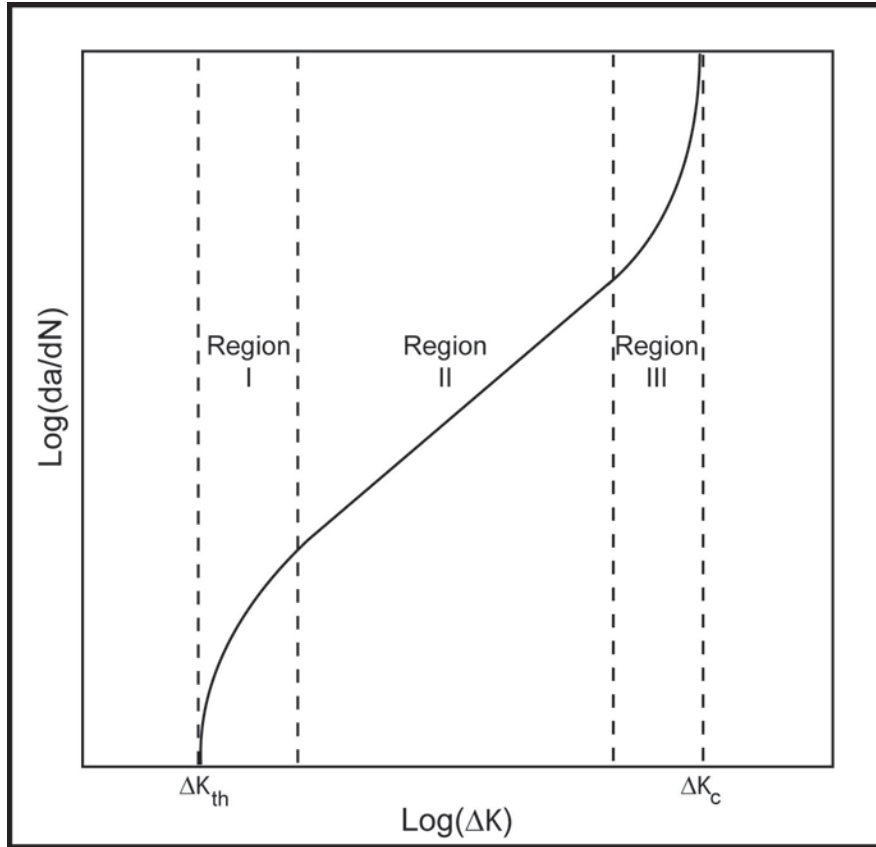
Figure 3-7-The relationship between the change of the crack length and stress intensity factor based on the Paris Law

In our experiments $R=0$, which means that cantilever beam is under tension only. So $K_{min}=0$ and

$$\Delta K=K_{max} - K_{min}= K_{max} \qquad (18)$$

Therefore, the two parallel cracks in TS will propagate under fatigue till their inner tips reach other. At this point unlike most isotropic materials, the two cracks will

not coalesce and they will propagate in the same plane (splats' interface). The two cracks will pass each other and then they will stop propagating due to significant decrease in stress intensity factor. By using stress intensity factor amount and Paris Law the changes in crack length was calculated. The algorithm of finding the crack length is shown in Figure 3-8.

```
                    ┌─────────┐
                    │  Start  │
                    └─────────┘
                         │
                         ▼
              ┌──────────────────────┐
              │  Start with the initial │
              │     crack length       │
              └──────────────────────┘
                         │
                         ▼
              ┌──────────────────────┐
              │ Read the Stress Intesity │◄──────────┐
              │  Factor (SIF) based on   │           │
              │   crack length (a_new)   │           │
              └──────────────────────┘           │
                         │                          │
                         ▼                          │
              ┌──────────────────────┐           │
              │       da=C(ΔK)^m        │           │
              └──────────────────────┘           │
                         │                          │
                         ▼                          │
                      ◇ is da=0? ◇ ─── No ──► ┌──────────────────┐
                         │                     │  a_new=a_old+da   │
                        Yes                    └──────────────────┘
                         │
                         ▼
                    ┌──────────┐
                    │ Converged │
                    └──────────┘
```
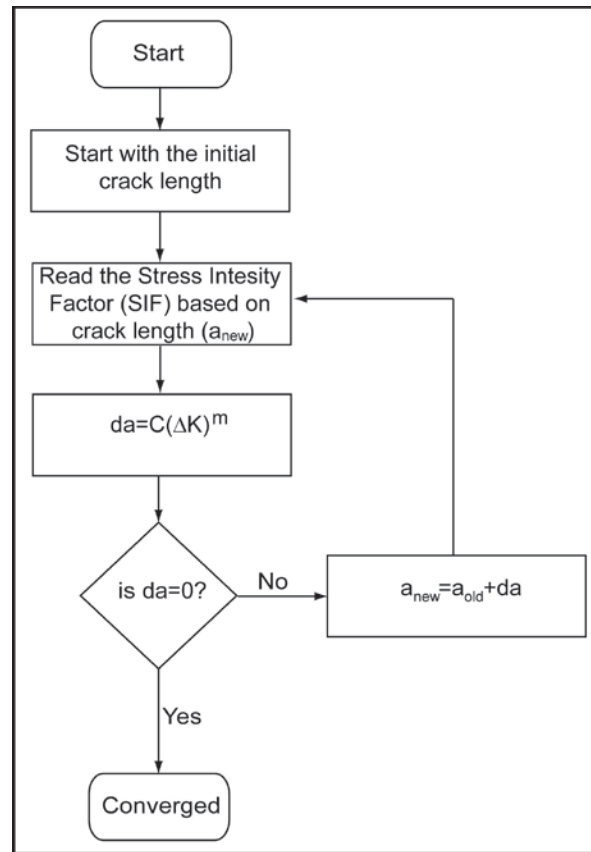
Figure 3-8-Algorithm for crack length change based on Paris Law

Crack length versus no. of cycles for a single pair of cracks is shown in Figure 3-9 based on Paris Law and using stress intensity factors results. For the first step, we considered that the constant m in the Paris Law is equal to one. So the change in the crack length (da) has a linear relation with the change of SIF (ΔK). As it is shown, the crack

length is increasing almost linearly till the two inner tips reach each other which is followed by rapid growth upon approach of two crack tips due to huge increase in the amount of stress intensity factor. Then the stress intensity factor will drop significantly as the two crack tips pass each other (Figure 3-6). The crack length will remain constant due to decrease of stress intensity constant which is almost zero (plateau region).
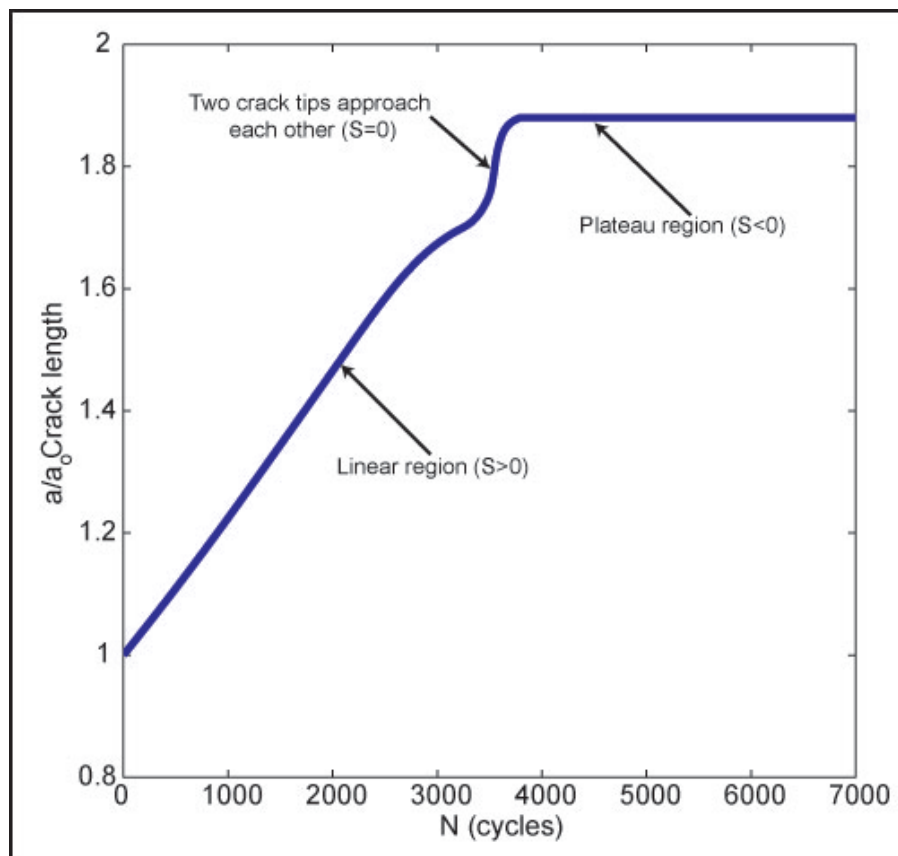
Figure 3-9-Crack length versus number of cycles for a single pair of cracks

3.4 Experiments

The relative dielectric constant of the samples at different frequencies has an asymptotic manner under fatigue test which is shown in Figure 3-10 for sampling

frequency of 1kHz and at 50% humidity. It was assumed that strain in the relatively thin coating was equal to substrate surface strain, and given by the equation 5. In this way coatings were cycled from 0 to 0.1% strain, placing the coating in tension (R=0), up to 50000 cycles by using a Zaber NA14B60 actuator. Every four samples of Table 1 was placed in the glove box for more than 10,000 seconds to make sure that the dielectric constant is not changing due to the humidity. Every 1,000 cycles, cycling was stopped and capacitance was measured at different points on the surface of the coating. The relative dielectric constant significantly increased from an initial value of approximately 8.5 over the first few hundred cycles, and then approaches a constant value of 10.5 after several thousand cycles which is 24% increase in comparison to the initial value. Error bars show that the changes in dielectric constant were significant relative to instrument and measurement noise. The measurements taken several hours after the mechanical cycling showed no change. Accepting that dielectric constant is linear relationship with crack area, and assuming cracks grow in a single direction (parallel to crack due to potential crack growth sites at splats' interface), it follows that self-arresting fatigue behavior is likely responsible for the asymptotic behavior in Figure 3-10.
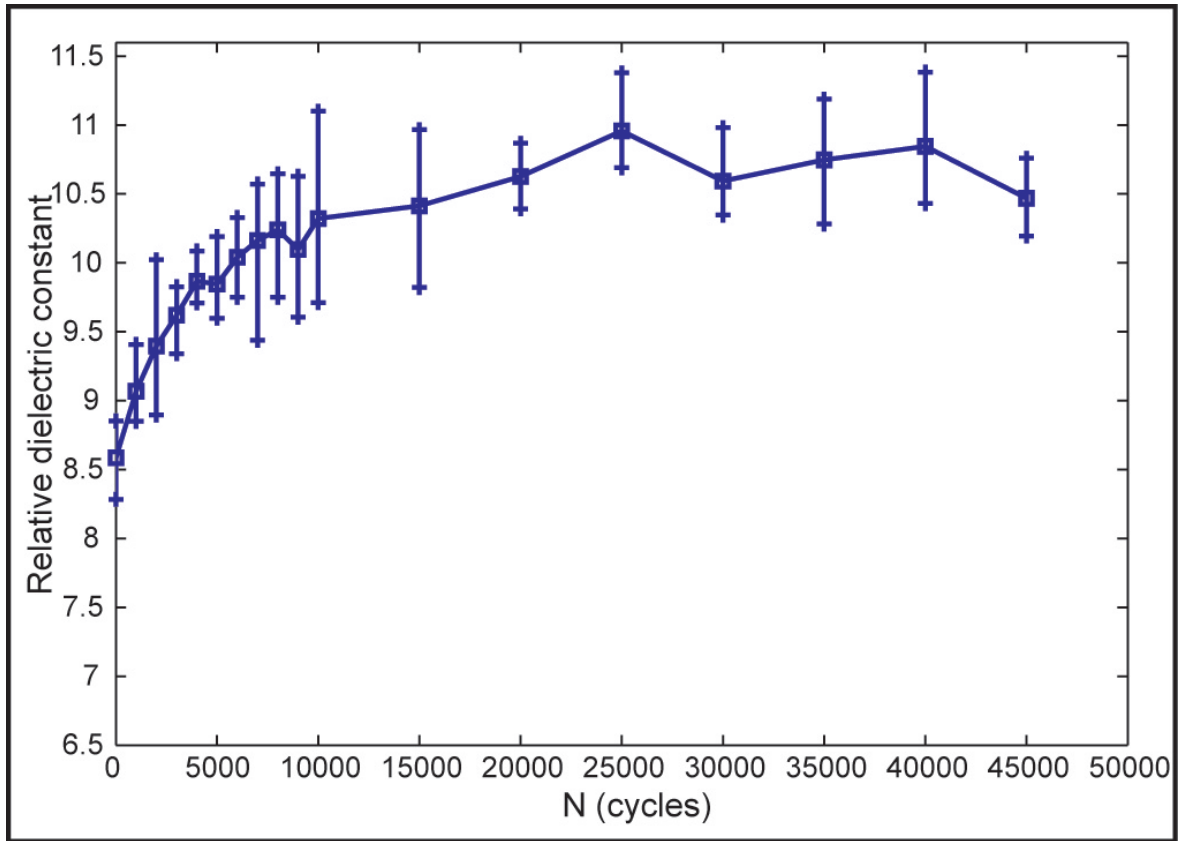
Figure 3-10-Relative dielectric constant versus number of cycles

The Dielectric constant is not increasing except when the strain was increased again. It is shown in Figure 3-11.
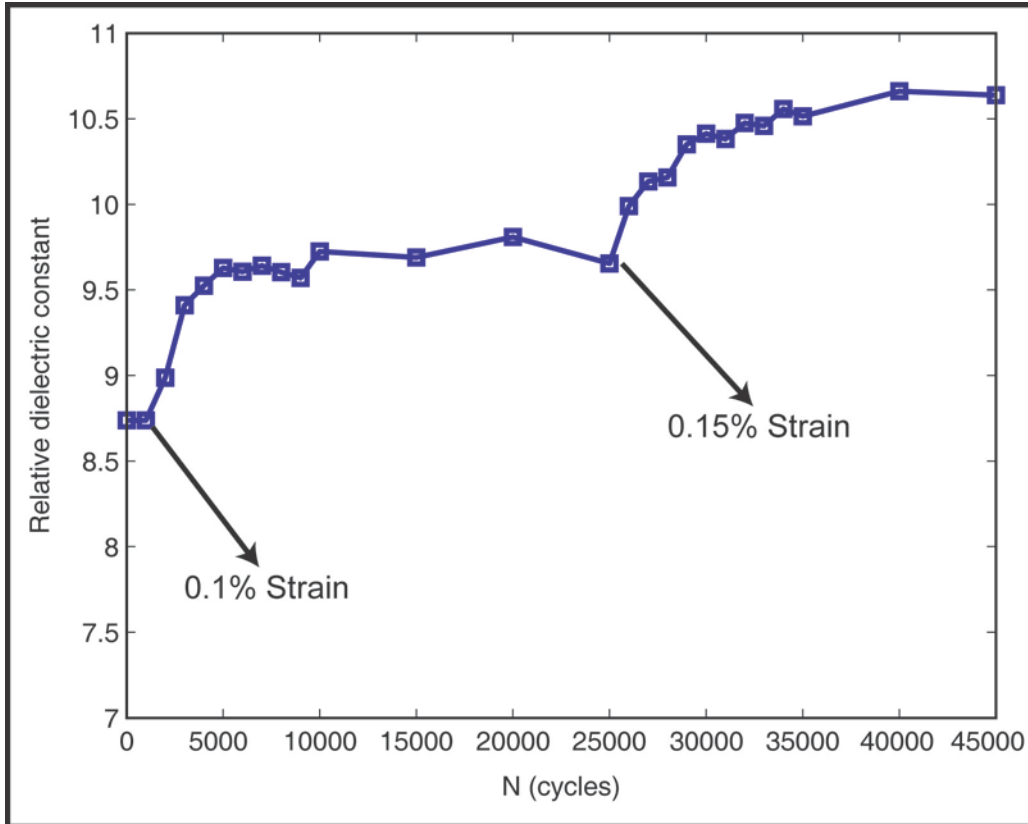
Figure 3-11-Change in effective dielectric constant with cycling, for experiments and models explained in text

3.5 **Multi Crack Pairs Concept**

For one crack pair, a slow initial crack growth phase is followed by rapid growth upon approach and arrest upon overlap which was shown in Figure 3-9. This behavior does not precisely match our experiments, but if we now consider the average growth of 100 crack pairs which are randomly distributed within a structure, the asymptotic behavior appears quite clearly which is shown in Figure 3-12. The cracks were distributed randomly within the structure by writing a code in Matlab software. These results match our experiments quite closely which indicates a linear relation between

crack length and relative dielectric constant of the structure. The results were verified by considering different random distribution of the cracks within the structure. It was observed that for any random distribution of the crack pairs, the overall shape of crack length growth is like Figure 3-12.
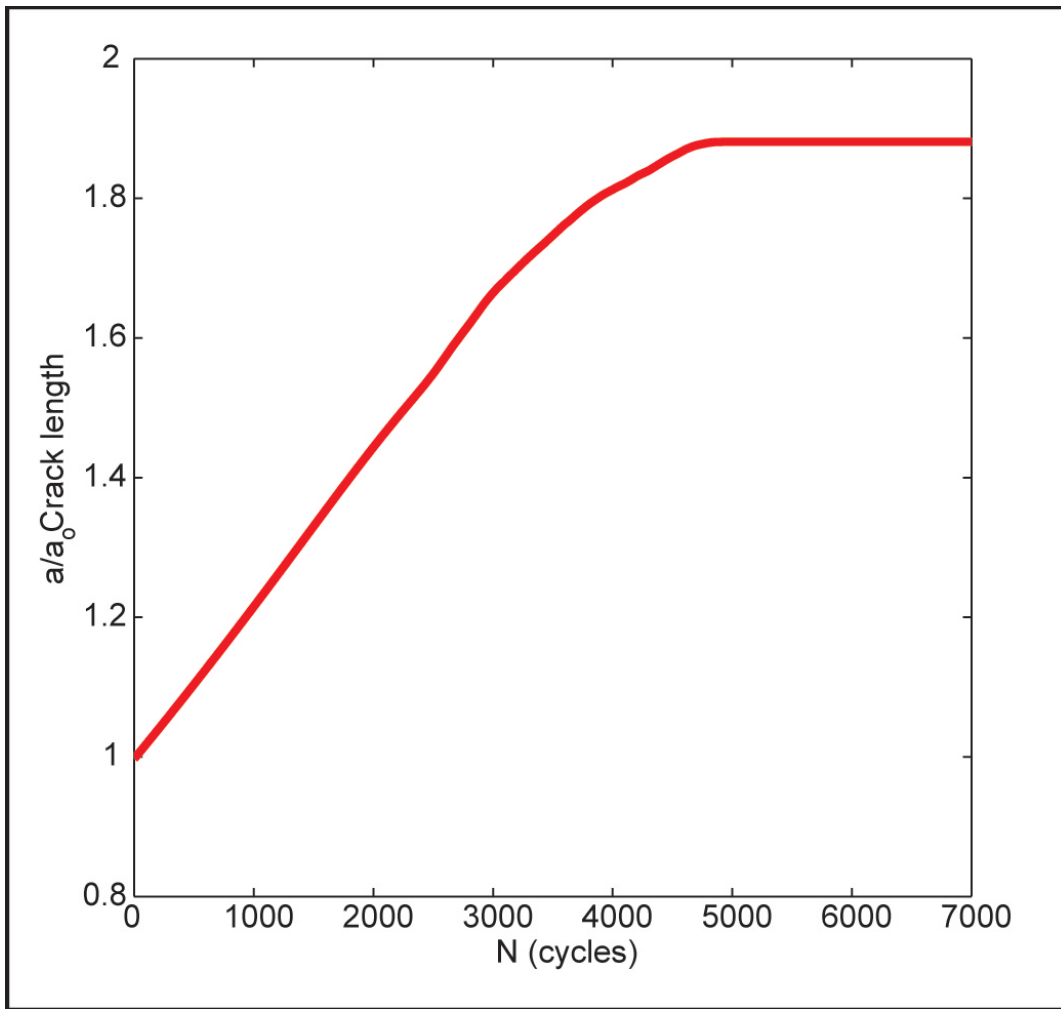
Figure 3-12-Average crack length versus number of cycles for a 100 pairs of cracks

Changing the random sets does not have a significant effect on the asymptotic behavior of the crack growth which is shown in Figure 3-13.
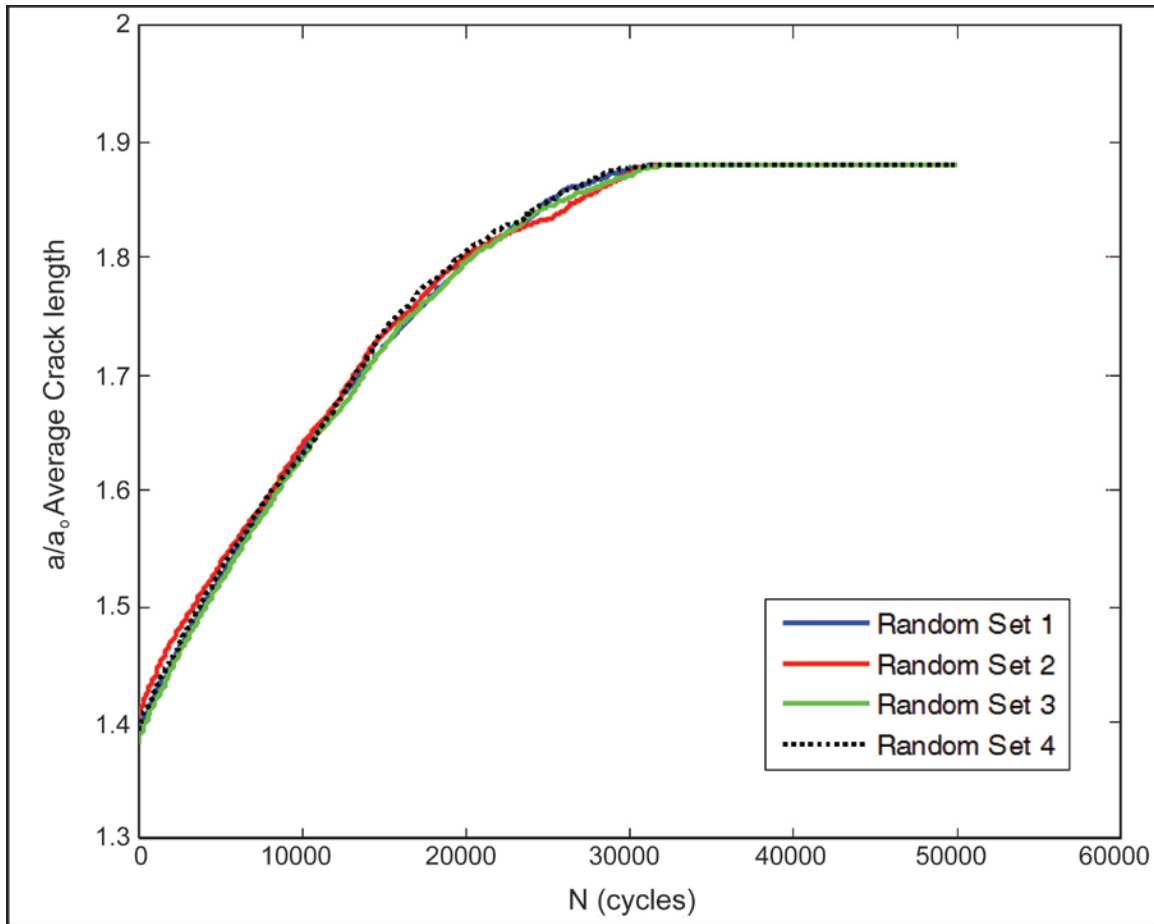
Figure 3-13-Crack length change versus number of cycles for different random sets

To investigate the effect of the other cracks on the asymptotic behavior of crack growth, an ANSYS model was generated with 20 randomly distributed crack pairs as it is shown in Figure 3-14.
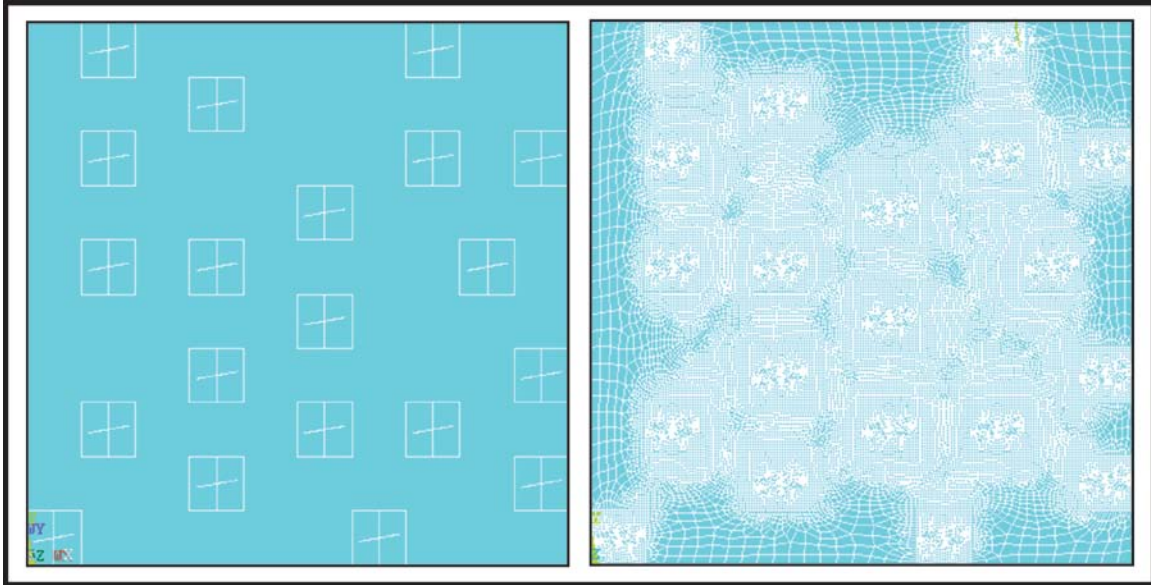
Figure 3-14-Twenty crack pairs randomly distributed in an ANSYS model

Two different random sets was considered in ANSYS to investigate the effect of crack pairs on each other. As it is shown in Figure 3-15, the shape of the crack growth is still asymptotic but when the crack pairs are closer to each other, the crack growth is faster. The maximum error with respect to the Matlab code is less than 2%.
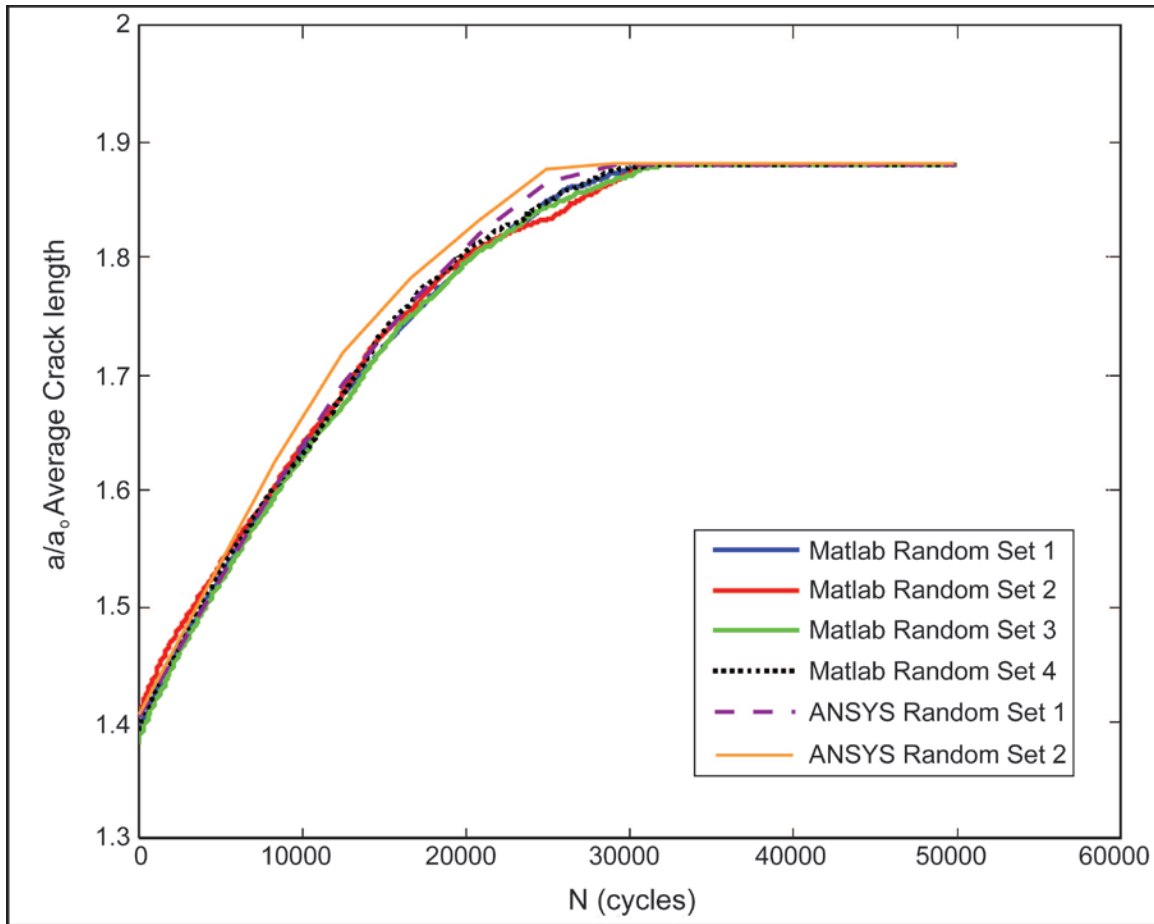
Figure 3-15-Crack length change versus number of cycles for Matlab and ANSYS random sets

In some cases, the cracks will coalescence with each other and make a large crack. To investigate the effect of this kind of crack interactions, different amount of cracks has been considered to coalescence with each other which is called crack bridging. The effect of crack bridging was investigated by doubling the length of 10%, 20% and 30% of cracks at 0, 1000, 2000 or 3000 cycles in the modeling. As it is shown in Figure 3-16, the asymptotic behavior remains after a jump in the amount of average crack length when we have bridging phenomena.
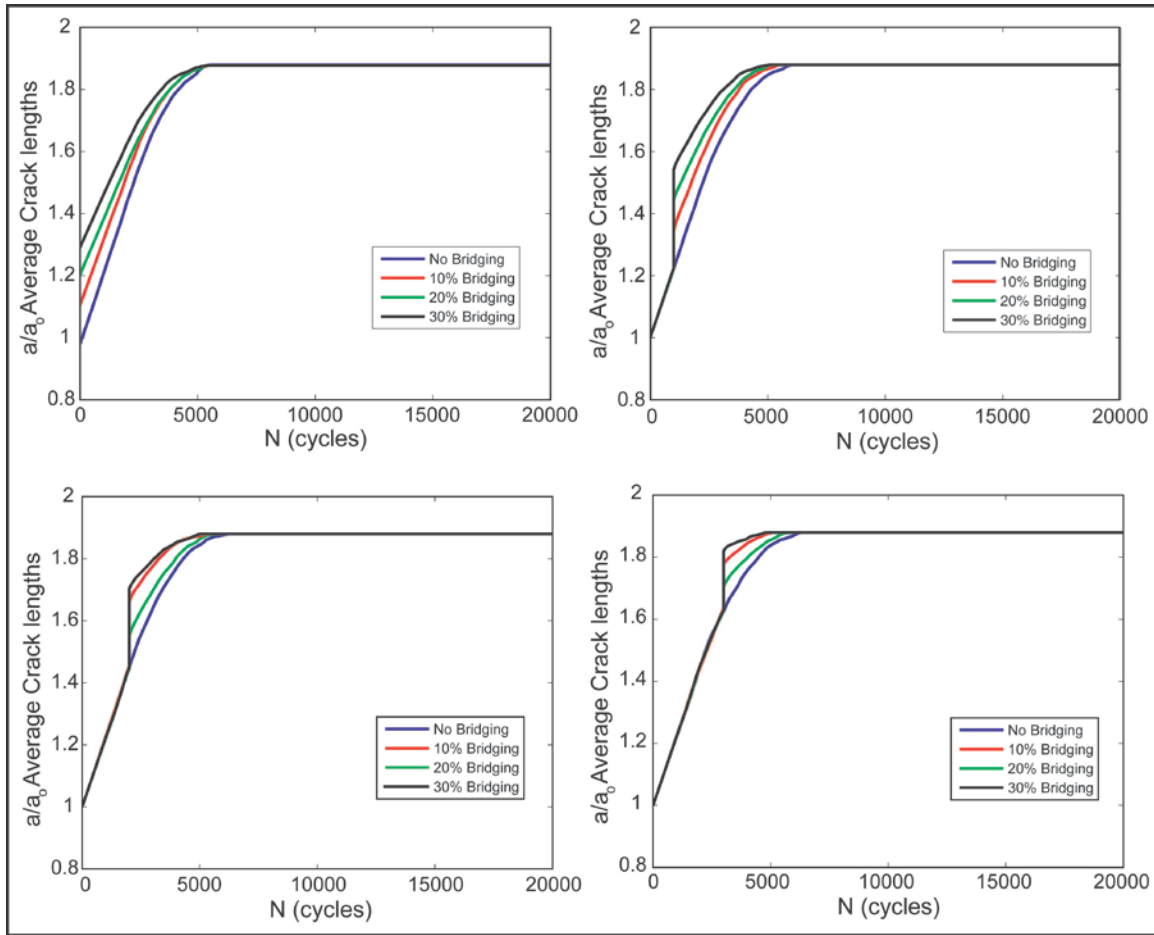
Figure 3-16-Effect of bridging of the cracks on crack length change

To find the dielectric constant of the structure directly from the finite element modeling and compare it to the experimental results, the cracks filled with water were modeled inside a porous Yttria-Stabilized Zirconia (YSZ). The dielectric constant of a pure YSZ is around 22 but the YSZ coating is a porous material consisting of a lot of cavity and cracks which are filled with air and water. In this study, the dielectric constant of the porous YSZ was considered to be 8 because in experimental results the initial dielectric constant is equal to 8.5 which is shown in Figure 3-10. All experiments were at 50% humidity so the cracks were considered to be filled with 50% water and 50% air.

The dielectric constant of the filled cracks was considered to be 40.5 which is the average of dielectric constant of air (1) and dielectric constant of water (80). The porosity of the cracks in the electrical FE modeling of the cracks was chosen precisely to match the initial amount of the dielectric constant from the experiments (8.5 which is shown in Figure 3-10). The length of the cracks was changing manually based on the results from Figure 3-12 for different amount of Paris law constants (*C* and *m*). The schematic electrical FE modeling of the YSZ coating and the cracks inside them is shown in Figure 3-17. As it is shown, the crack length was increasing based on the average crack length change shown in Figure 3-12.
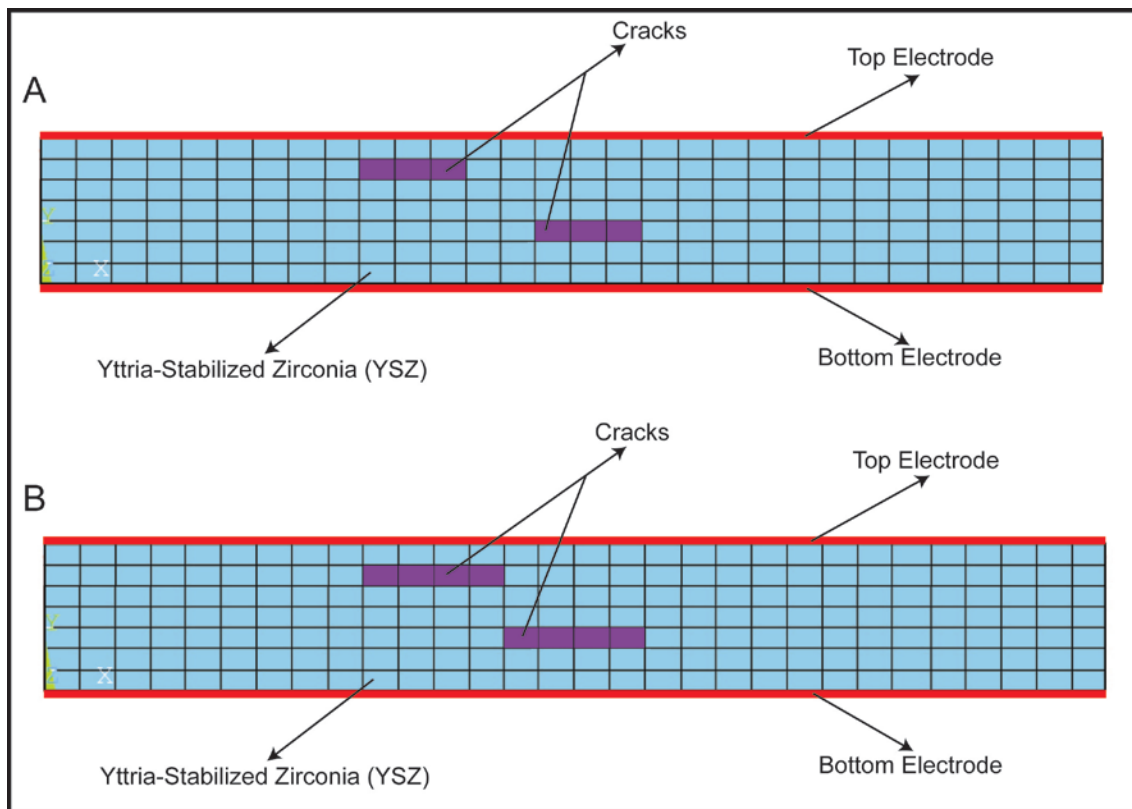
Figure 3-17-Schematic FE modeling of Yttria-Stabilized Zirconia (YSZ) coatings including cracks; A) before crack propagation; B) after crack propagation using Paris law

It has been found that the crack length has a near linear relation with capacitance and dielectric constant which is shown in Figure 3-18.
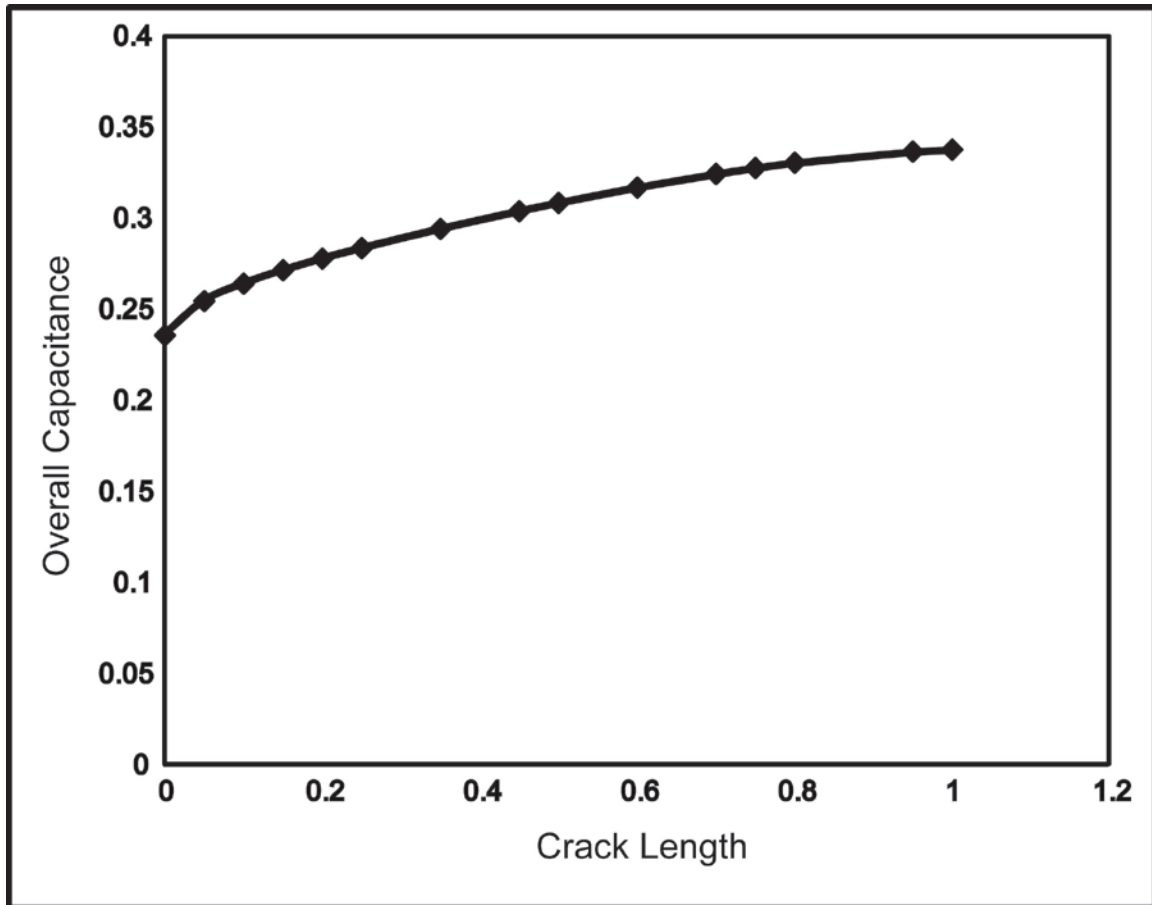
Figure 3-18-Near linear relation between the capacitance and the crack length based on FE modeling

By considering a linear relationship between the relative dielectric constant and crack length, the asymptotic behavior of the crack length from the FE modeling can be transformed to dielectric constant versus number of cycles. By changing the amount of Paris Law constants (*C* and *m*), the electrical FE modeling results can predict the

experimental results perfectly. The effect of change of C and m are shown in Figure 3-19. As it is shown by increasing the amount of C, it takes less cycles to reach the plateau region. Increasing m will result in taking more cycles to reach the plateau region.
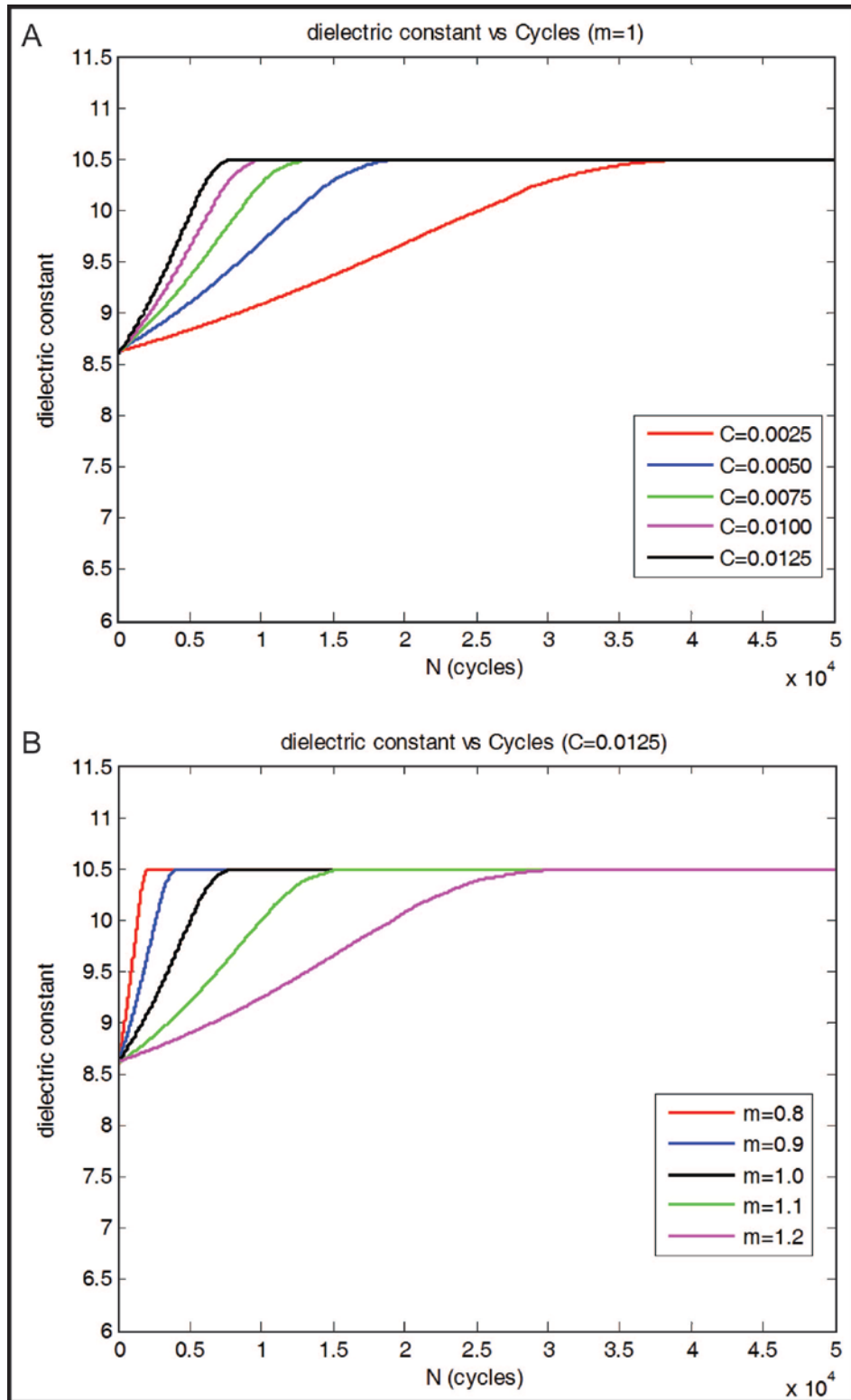
Figure 3-19- Asymptotic behavior of dielectric constant by changing A) *C* **constant and B)** *m* **constant in Paris Law**

By changing the Paris Law constants, the suitable amounts for them was calculated based on experimental results. The Paris Law constants in the modeling were considered as *C*=0.0125 and *m*=1 to show the asymptote behavior of crack length growth at 5000 cycles as it is shown in Figure 3-20. The C value is high, but similar to that in short crack behavior, prior to arrest [13, 16-18, 21-22, 44]. As it is shown in Figure 3-20, the FE modeling results are consistent with experimental results.
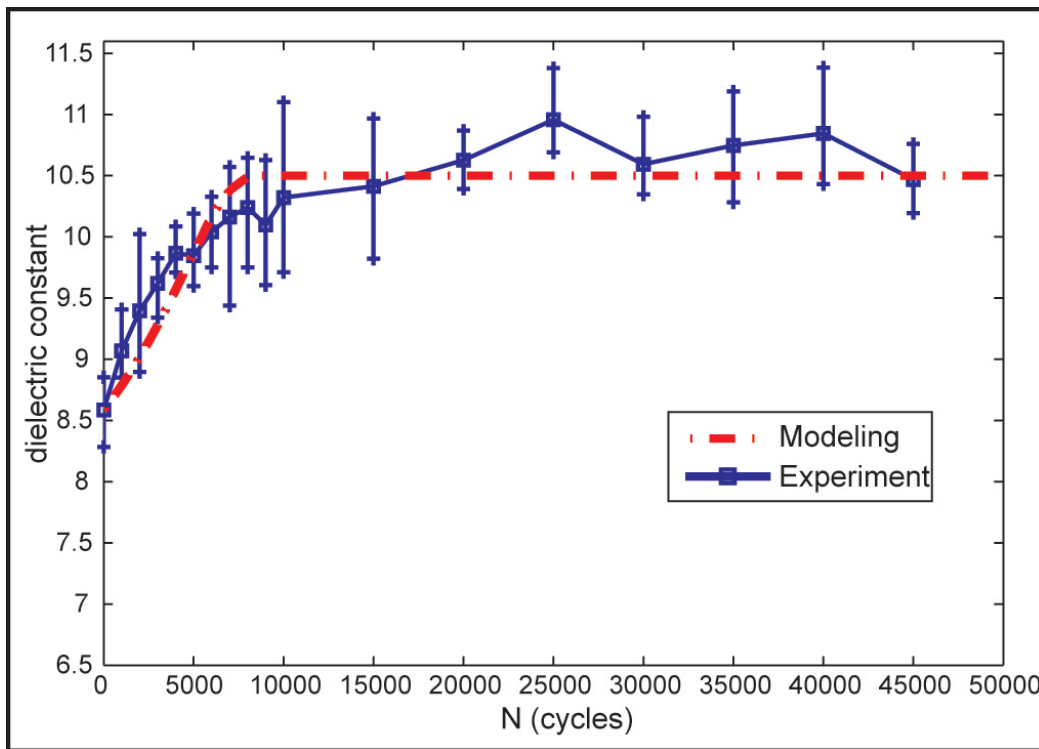
Figure 3-20-Change in effective dielectric constant with cycling, for experiments and models explained in text

By changing the amount of Paris Law constants (*C* and *m*), the experimental results can be predicted easily for any other kind of thermal sprayed coating.

3.6　**Conclusion**

As it was shown, the crack growth modeling based on the Paris Law can predict the asymptotic behavior of the dielectric constant during the fatigue test. For every sample with different coating procedure, the *C* and *m* in the Paris Law can be assigned to mimic the experimental results. It has been shown that *m*=1 and a quite high value for *C* can predict the experimental results for any kind of thermal spray coating easily.

CHAPTER 4. Finding the Topography of a Surface Using a New Method and its Application on Thermal Spray Coatings

4.1 **Abstract**

The author reports the change in measured dielectric constant of thermal barrier coatings after using different kind of polishing procedure on it. TS YSZ coatings on Al substrates samples were used and their dielectric constant was measured. The surface of the samples was polished and the dielectric constant of them was measured. The measured dielectric constant of the samples increased when the surface was smoother. The capacitance of the structure including air gap and coating was modeled by Finite Element Method (FEM) and converted to dielectric constant. The author suggests an inverse procedure to measure the surface roughness and topology of any material by finding its dielectric constant.

4.2 **Introduction**

Thermal spray (TS) coatings and materials including thermal barrier, tribological and anti-corrosive coatings have established application across huge number of engineering fields [45]. TS is attractive for these systems due to its low cost, ability to coat large areas and flexibility in material feedstock. These attributes, along with improvements in process diagnostics have spurred the exploration of TS for more functional applications including fuel cells [6], conformal electronic sensors [7] and biomedical implants [8].

Air or gas gap between two metal walls is typical in many industries. Because of various reasons such as aging, size change, temperature and radiation influence, vibrations, creep, etc. In order to prevent this, the gap width, e.g. between two concentric

66

metal tubes should be continuously monitored. Typically the gap width is measured by using eddy-current technique [46]. This flow creates a reaction field which affects the pick-up voltages in the receive coil. The change in the overall reaction field due to the air gap creates the typical response signal. However, the accuracy of such measurements is rather low. Theoretically, to improve the accuracy, the high-frequency eddy current probe can be used. However, due to electromagnetic field attenuation, such a probe provides only low amplitude response. Moreover, the results of eddy-current measurements are affected by changes in material electric conductivity. The other alternative technique, which can be used for accurate gap measurement, is the ultrasonic method. Ultrasound is not affected by variations in electrical conductivity or permeability, and it can provide the desired accurate measurements and 100% mapping. Another method for measuring the air gaps is photothermal radiometry [47]. All of the above methods are expensive and the resolution of them is really dependent on the equipment resolution and mapping procedure. The effect of air gap on measured dielectric constant of materials was investigated before [47-48] but this effect wasn't used as a method to measure the air gap or to inspect the topography of a material.

Schematic Thermal Spray process is shown in Figure 4-1. In this study TS YSZ coatings (0.20 – 0.40 mm thick) on Al substrates samples were used and their dielectric constant was measured. The surface of the samples was polished by using different sand papers, and the dielectric constant of them was measured again. By using the smoother sand papers, the dielectric constant of the samples increased. The electrode can attach to the coating with a very small air gap between them on a smooth surface and the measured dielectric constant will be increased. In some cases a conductive material like copper foil

67

or a graphite layer will be used to prevent the air gap on the sample. But these methods will change the surface topology.
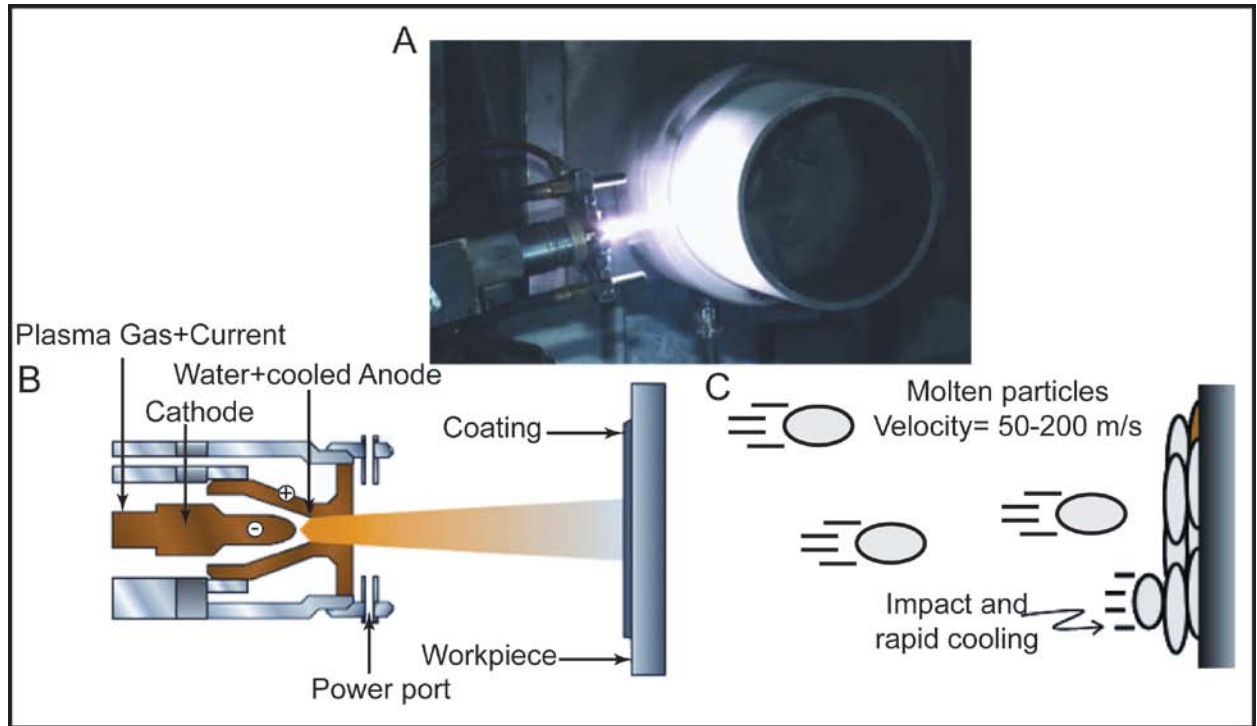
Figure 4-1-A) Thermal spray procedure; B) Schematic thermal spray process; C) high velocity molten particles which make splats on a substrate

In this study, the capacitance of the structure including air gap and coating was modeled by Finite Element Method (FEM) and then it was converted to dielectric constant. So the measured dielectric constant could be predicted by having the actual dielectric constant of the material (i.e. coating) and the width of air gap. We suggest an inverse procedure to measure the surface roughness and topology of any material by finding its dielectric constant as a Nondestructive Test (NDT). In this method, the dielectric constant of an unknown surface will be measured and then it will be modeled

using FEM and the actual material dielectric constant. The experimental and FE results can be matched by changing the air-gap width in the FE model. So we can roughly measure the air gap amount. The accuracy of the method depends on the size of the electrode. If we can have a very small electrode, we can predict topography of the surface with a very high resolution (Figure 4-2).
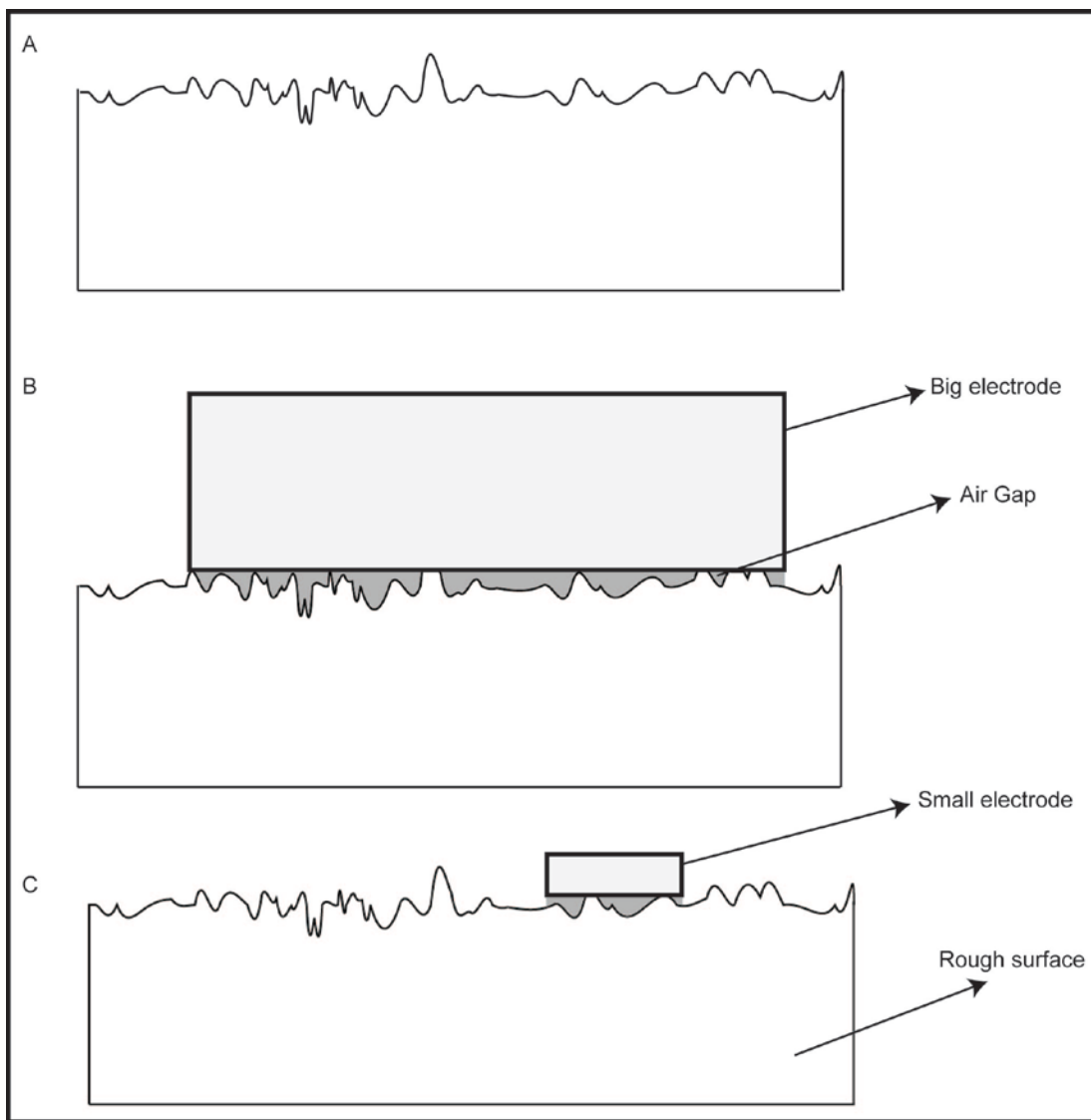
Figure 4-2-A) A rough surface; measuring the air gap by B) a big electrode; C) a small electrode.

4.3 Method

We had different samples of Thermal Spray coatings which are shown in Table 6. We used sample number four and polished it with sand papers of 400 and 600. Average particle diameters of these sand papers are 23 and 16 µm respectively [49].

Table 6-Different parameters of coating samples

	Sample#1	Sample#2	Sample#3	Sample#4
Coating Thickness (mm)	0.2	0.22	0.26	0.40
Current (A)	700	700	700	700
Argon (slm)	40	55	55	30
Helium (slm)	10	10↔15	10	5
Hydrogen (slm)	0	0	0	0
Carrier (slm)	4.0	4.0	4.0	4.0
Federate (RPM)	3.0	3.0	3.0	3.0

The capacitance of the coatings was measured by an impedance analyzer operating at 1kHz (HP 4294A precision impedance analyzer and HP 16451B Dielectric test fixture attachment). The electrodes are shown in Figure 4-3. Capacitance is the ability of a body to hold an electrical charge. Capacitance is also a measure of the amount of electric charge stored for a given electric potential. The measured capacitance was converted to dielectric constants by the following formula:

$$\varepsilon_r = \frac{t_a \ C_p}{A \ \varepsilon_o} \tag{19}$$

where ε_r is dielectric constant, t_a is average thickness of coating, C_P is capacitance, A is area of electrodes, and $\varepsilon_o = 8.85 \times 10^{-12}$ F/m. The dielectric constant (or relative permittivity) of a material is the ratio of the amount of stored electrical energy when a potential is applied, relative to the permittivity of a vacuum (which is equal to one by definition). The measured capacitance and dielectric constant of unpolished and polished coatings are shown in Table 7.
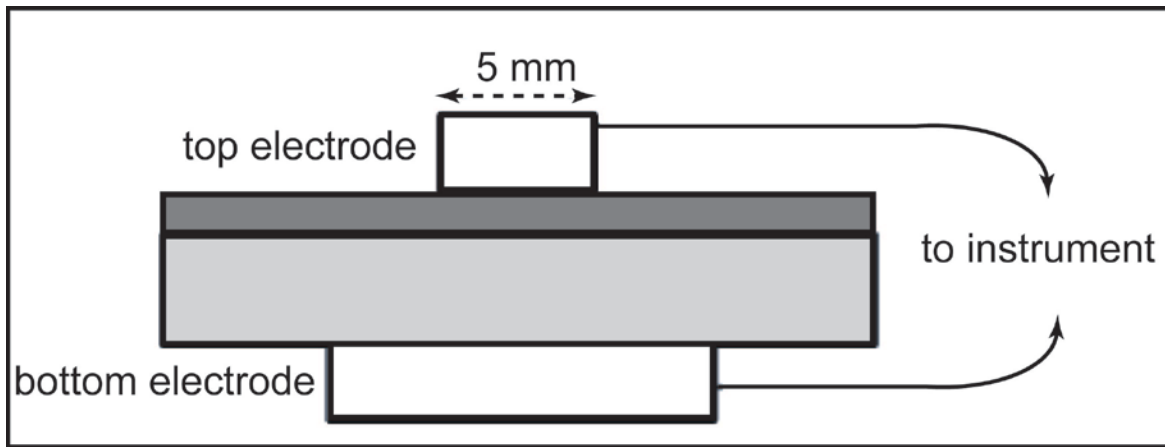
Figure 4-3-Electrodes for measuring the capacitance

Table 7-Capacitance and Dielectric Constant of unpolished and polished samples

	Average Particle diameter (µm) [49]	C_p (pF)	Dielectric Constant	Predicted Air gap amount by FEM (µm)
Unpolished	-	4.0	9.3	28.0
400	23	4.4	10.2	23.6
600	16	5.3	12.1	16.3

4.4   **Finite Element Analysis**

The dielectric constant of the structure was modeled by finite element method in ANSYS which is shown in Figure 4-4. The dielectric constant of the Zirconia and air are around 22 and 1 respectively. By increasing the air gap amount, the dielectric constant of the structure will be decreased which is shown in Figure 4-5. So by comparing the measured dielectric constant and Figure 4-5, we can roughly predict the air gap amount. For example in our case, for polished samples with 400 and 600 sand papers, the predicted amount of air gap is about 16.261 and 23.589 µm which are comparable with 23 and 16 µm as it shown in table 2 too. So the air gap for the unpolished sample with dielectric constant of 9.269 is about 28.001µm.
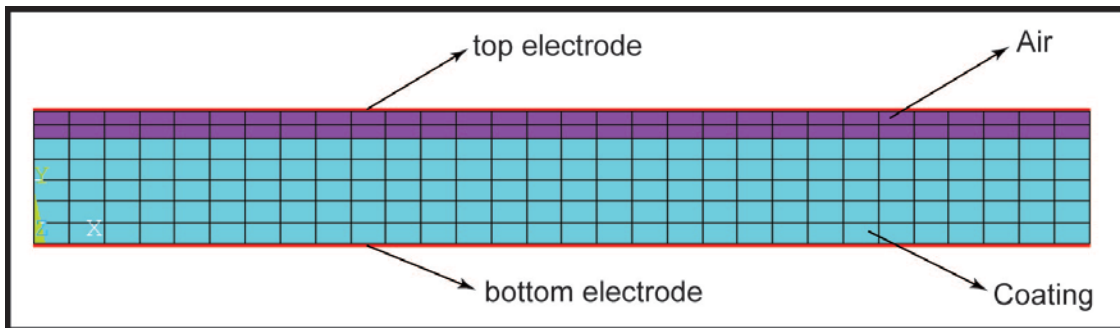
Figure 4-4-ANSYS model
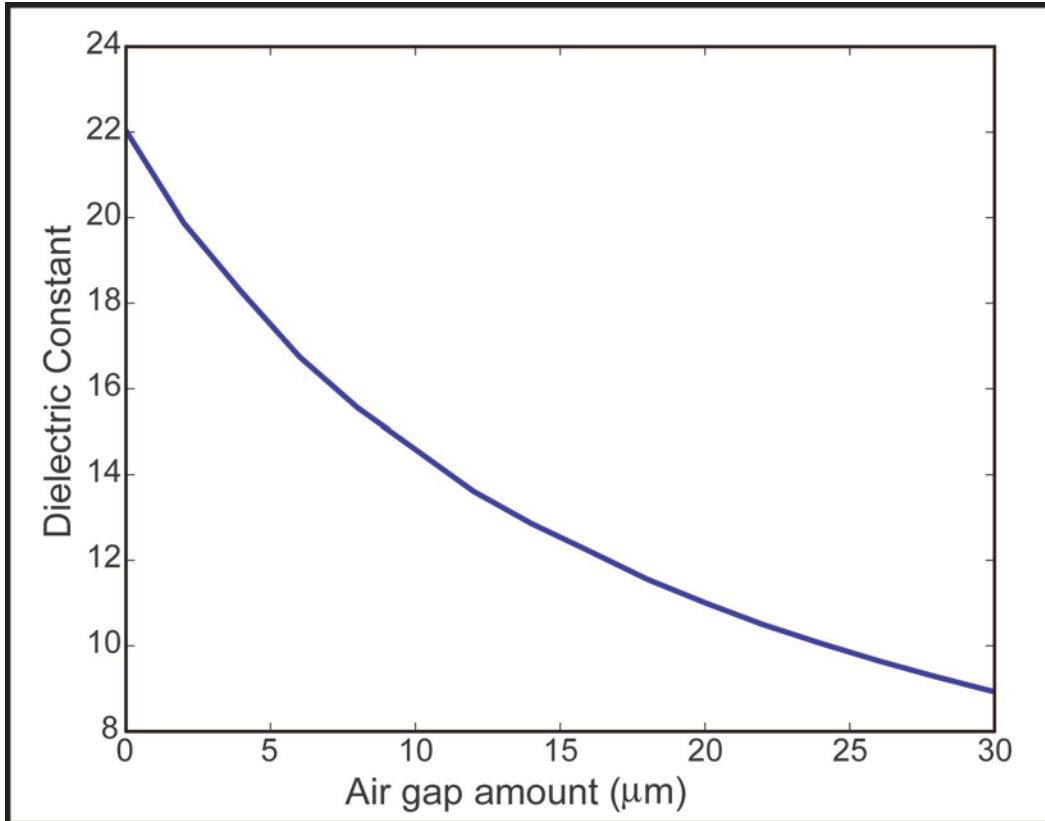
Figure 4-5-Dielectric constant vs. air gap amount From FE modeling

4.5 Finding Real Contact Area and Real Pressure

If a smooth surface (i.e. electrode) and a rough surface (nominally flat), come into contact until their reference planes (taken to pass through the mean of the peak height distribution) are separated by a distance d, then there will be contact at those asperities whose height, z, is greater than d (Figure 4-6). The classical statistical model for a combination of elastic and elastic-plastic contacts between a rough surface and a smooth surface was considered based on Greenwood and Williamson [50] (G&W). They assumed that (1) the rough surface is covered with a large number of asperities, which, at least near their summit, are spherical; (2) asperity summits have a constant radius of R_p;

(3) their heights vary randomly; and (4) most engineering surfaces have a Gaussian distribution of peak heights. Many surfaces follow a Gaussian distribution.
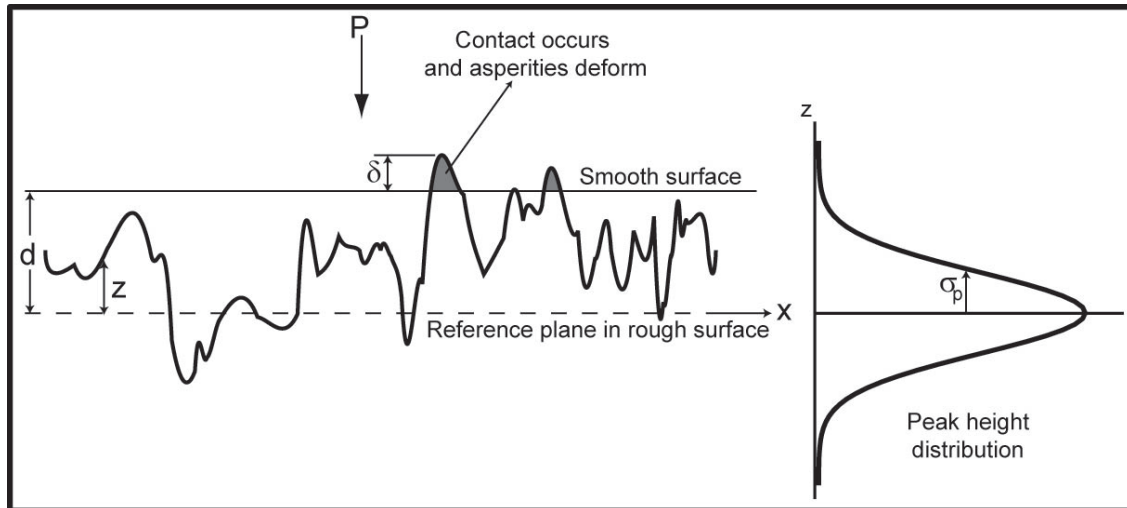
Figure 4-6-A smooth surface in contact with a rough surface and its peak height distribution

If we consider that the rough surface peak heights having a probability density function of $p(z)$; the apparent pressure, p_a, mean real pressure, p_r, (elastic) real area of contact, A_{re}, number of contact spots, n, and mean asperity real area of contact can be calculated as a function of separation, d for elastic contacts in static conditions with no tangential stresses using G&W's assumptions.

If the two surfaces come together until their reference planes are separated by a distance d, then there will be contact at any asperity whose height was originally greater than d. Thus, the probability of making contact at z is

$$P(z > d) = \int_d^\infty p(z)dz \tag{20}$$

and if there are N asperities in all, the expected number of contacts will be

$$n = N \int_d^\infty p(z)dz \tag{21}$$

Also, since $\delta = z - d$, the total (elastic) real area of contact is

$$A_{re} = \pi N R_p \int_d^\infty (z - d)\, p(z)\, dz \tag{22}$$

Similarly, based on Hertz contact theory of two spheres, we can find the expected total load as

$$W = p_r A_{re} = p_a A_a = (\frac{4}{3}) N E^* R_p^{1/2} \int_d^\infty (z - d)^{3/2}\, p(z)\, dz \tag{23}$$

where p_r and p_a are real pressure and apparent pressure, respectively, A_a is the apparent area, and E^* is the composite modulus as

$$\frac{1}{E^*} = \frac{1 - v_1^2}{E_1} + \frac{1 - v_2^2}{E_2} \tag{24}$$

It is convenient to work with dimensionless variables as follow

$$\frac{p_a}{(\eta R_p \sigma_p) E^* (\sigma_p / R_p)^{1/2}} = \left(\frac{4}{3}\right) F_{3/2}(D) \tag{25}$$

$$\frac{p_r}{E^* (\sigma_p / R_p)^{1/2}} = \left(\frac{4}{3\pi}\right) F_{3/2}(D) / F_1(D) \tag{26}$$

$$A_{re} E^* (\sigma_p / R_p)^{1/2} / p_a A_a = \left(\frac{3\pi}{4}\right) F_1(D) / F_{3/2}(D) \tag{27}$$

$$n R_p \sigma_p E^* E^* (\sigma_p / R_p)^{1/2} / p_a A_a = F_0(D) / \left(\frac{4}{3}\right) F_{3/2}(D) \tag{28}$$

$$(A_{re} / n) R_p \sigma_p = \pi F_1(D) / F_0(D) \tag{29}$$

where D, the dimensionless separation, is d/σ_p; η is the density asperity summit per unit area (N/A_a) on a surface with smaller density; and $F_m(D)$ is a parabolic cylinder function given by

$$F_m(D) = \int_D^\infty (s-D)^m p^*(s)ds \qquad (30)$$

where $p^*(s)$ is the standardized peak-height probability density function in which the height distribution has been scaled to make its standard deviation unity. In our case which peak-height distribution following a Gaussian height distribution

$$F_m(D) = \left[\frac{1}{(2\pi)^{1/2}}\right]\int_D^\infty (s-D)^m \exp\left(\frac{-s^2}{2}\right)ds \qquad (31)$$

For a Gaussian distribution, D, p_r, A_{re}, n, and A_{re}/n vs p_a can be obtained. Next the data are fitted to a power-form using the least-squares fit and are presented as following formulas based on Bhushan [51].

$$D = 1.40[\log(0.57/P_a)]^{0.65} \qquad (32)$$

$$\frac{P_r}{E^*\left(\sigma_p/R_p\right)^{1/2}} = 0.42\, P_a^{0.04} \qquad (33)$$

$$\frac{A_{re}}{A_a\left(\eta R_p \sigma_p\right)} = 2.40 P_a^{0.96} \qquad (34)$$

$$\frac{n}{\eta A_a} = 1.21 P_a^{0.88} \tag{35}$$

$$\frac{A_{re}/n}{R_p \sigma_p} = 2.00 P_a^{0.08} \tag{36}$$

where

$$P_a = p_a / \left[(\eta R_p \sigma_p) E^* (\sigma_p / R_p)^{1/2} \right] \tag{37}$$

Now, a relationship between the average air-gap amount and the interplanar separation, d, will be proposed. So by finding the air-gap amount from experimental data and ANSYS results for dielectric constant of the material, the interplanar separation, d, real pressure, p_r, real area of contact, A_{re}, number of contact spots, n, and mean asperity real area of contact, A_{re}/n, can be found.

The air-gap area, A_{air}, can be found by the following formula,

$$A_{air} = Lh - \int_0^L z(x)\, dx + \sum_{i=1}^n A_i \tag{38}$$

where $z(x)$, is the surface profile, n is the number of asperities in contact with smooth surface and A_i is pressed area of the i-th asperity (Figure 4-7A).

So the average air gap amount, h_{air}, is

$$h_{air} = \frac{A_{air}}{L} = h - \frac{1}{L}\int_0^L z\, dx + \frac{1}{L}\sum_{i=1}^n A_i \tag{39}$$

$$h_{air} = h - m + \frac{1}{L}\sum_{i=1}^n A_i \tag{40}$$

where m, is mean value of the profile.

As it is shown in Figure 4-7B, the pressed area of the i-th asperity is

$$A_i = R^2 \arcsin\left(\frac{a_i}{2R}\right) - \frac{a_i}{2}(R - \delta_i) \tag{41}$$
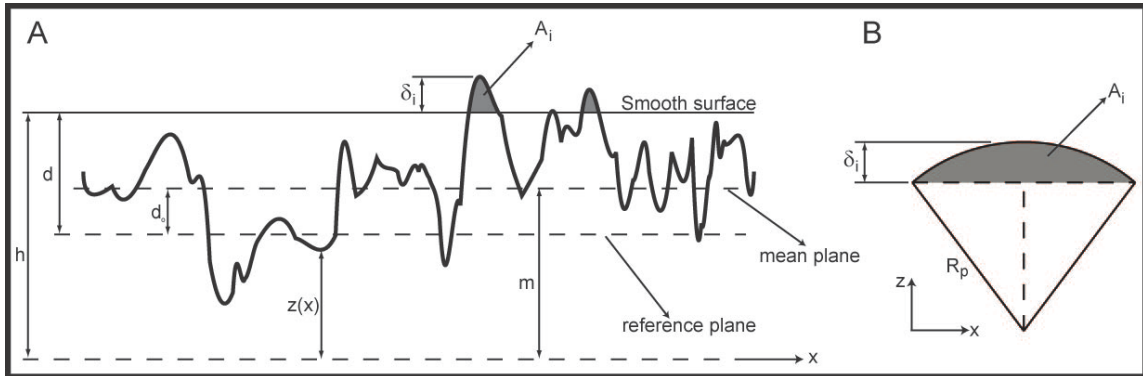
Figure 4-7-A) A smooth surface in contact with a rough surface; B) One peak with under contact

Now, if we consider that $h=d$; i.e. the x-axis is located at reference plane of the mean of the peak height distribution; δ_i and a_i will be

$$\delta_i = z - d \tag{42}$$

79

$$a_i = \sqrt{R\delta_i} = [R(z-d)]^{1/2} \tag{42}$$

So,

$$A_i = R^2 \arcsin\left(\left(\frac{z-d}{4R}\right)^{1/2}\right) - \left(R(z-d)\right)^{1/2}(R+d-z) \tag{43}$$

and then the average air-gap amount is

$$h_{air} = d - m + N \int_d^\infty A_i\, p(z)\, dz \tag{44}$$

so by considering a Gaussian distribution of peak heights

$$\begin{aligned}
h_{air} = d - m + &\left[\frac{1}{\sigma_p(2\pi)^{1/2}}\right] N \int_d^\infty \left(R^2 \arcsin\left(\left(\frac{z-d}{4R}\right)^{1/2}\right)\right. \\
&\left. - \left(R(z-d)\right)^{1/2}(R+d-z)\right) \exp\left(\frac{-z^2}{2\sigma_p^2}\right) dz
\end{aligned} \tag{45}$$

4.6 Conclusion

This method can be used to predict the surface property and air gap amount of any sample with a dielectric constant. If we have smaller electrodes, the resolution of the

method will increase significantly. The dimension of our electrode is about 5mm. Even with this big electrode, we measured the air gaps in order of 10 µm.

CHAPTER 5. Discussion

The predicted *C* value in Paris law is high comparing with the isotropic materials, but it is similar to the short crack behavior, prior to arrest. In this study the propensity of TS coatings to undergo crack growth under nominally elastic strains was described and a mechanism for crack growth in TS coatings was proposed. A potential measurement method for crack initiation and growth behavior was indentified. This method can be used as a non-destructive test method. This consideration could also explain the high-reliability associated with coatings deposited with nano-scale powder, for which no such 'size effect' would be manifested, as crack fields would interact immediately.

As it was shown, the crack growth modeling based on the Paris Law can predict the asymptotic behavior of the dielectric constant during the fatigue test. For every sample with different coating procedure, the *C* and *m* in the Paris Law can be assigned to mimic the experimental results. It has been shown that *m*=1 and a quite high value for *C* can predict the experimental results for any kind of thermal spray coating easily.

By finding the dielectric constant of any material, the surface properties and the amount of air gap between the electrode and the sample can be predicted. By decreasing the size of the electrode, the resolution of the method will increase significantly.

For the future works, this method can be used to find the fracture fatigue behavior of any other kind of coatings or ceramics. The Paris law constants for these materials can be measured based on the experimental data from impedance spectroscopy and comparing them with the FE modeling.

References

[1]   S. Kuroda and et al., "Warm spraying—a novel coating process based on high-velocity impact of solid particles," *Science and Technology of Advanced Materials,* vol. 9, p. 033002, 2008.

[2]   K. W. Schlichting*, et al.*, "Failure modes in plasma-sprayed thermal barrier coatings," *Materials Science and Engineering a-Structural Materials Properties Microstructure and Processing,* vol. 342, pp. 120-130, Feb 2003.

[3]   J. Wu*, et al.*, "High-temperature chemical stability of low thermal conductivity ZrO2-GdO1.5 thermal-barrier ceramics in contact with [alpha]-Al2O3," *Scripta Materialia,* vol. 50, pp. 1315-1318, 2004.

[4]   D. R. Mumm*, et al.*, "Characterization of a cyclic displacement instability for a thermally grown oxide in a thermal barrier system," *Acta Materialia,* vol. 49, pp. 2329-2340, Jul 2001.

[5]   F. Yang and P. Xiao, "Nondestructive evaluation of thermal barrier coatings using impedance spectroscopy," *International Journal of Applied Ceramic Technology,* vol. 6, pp. 381-399, 2009.

[6]   R. Hui*, et al.*, "High performance metal-supported solid oxide fuel cells fabricated by thermal spray," *Journal of Power Sources,* vol. 191, pp. 371-376, 2009.

[7]   Q. Chen*, et al.*, "Novel sensor fabrication using direct-write thermal spray and precision laser micromachnining," *Journal of Manufacturing Science and Engineering-Transactions of the Asme,* vol. 126, pp. 830-836, 2004.

[8]   P. L. Tranquilli*, et al.*, "Evaluation of different preparations of plasma-spray hydroxyapatite coating on titanium alloy and duplex stainless steel in the rabbit " *Journal of Materials Science-Materials in Medicine,* vol. 5, pp. 345-349, 1994.

[9]   R. Ahmed and M. Hadfield, "Mechanisms of fatigue failure in thermal spray coatings," *Journal of Thermal Spray Technology,* vol. 11, pp. 333-349, 2002.

[10]   E. Turunen*, et al.*, "On the role of particle state and deposition procedure on mechanical, tribological and dielectric response of high velocity oxy-fuel sprayed alumina coatings," *Materials Science and Engineering a-Structural Materials Properties Microstructure and Processing,* vol. 415, pp. 1-11, 2006.

[11]   A. A. Kulkarni*, et al.*, "Advanced microstructural characterization of plasma-sprayed zirconia coatings over extended length scales," *Journal of Thermal Spray Technology,* vol. 14, pp. 239-250, 2005.

[12]   K. Kaneko and A. Ohmori, "Evaluations of strength of thermal sprayed coating with crack," *Thermal Spray 2004: Advances in Technology and Applications (ASM International),* pp. 240-245, 2004.

[13]   S. Suresh, *Fatigue of Materials*, 2nd ed.: Cambridge University Press, 1998.

[14]   S. Pearson, "Initiation of fatigue cracks in commercial aluminium alloys and the subsequent propagation of very short cracks," *Engineering Fracture Mechanics,* vol. 7, pp. 235-240, IN15-IN18, 241-247, 1975.

[15]   T. L. Anderson, *Fracture Mechanics: Fundamentals and Applications*, 3rd ed.: CRC Press, 2004.

[16] C. J. Gilbert, *et al.*, "Anomalous cyclic fatigue-crack propagation behavior of small cracks in monolithic, grain-bridging ceramics," *Ceramics International,* vol. 26, pp. 721-725, 2000.

[17] T. Fett and D. Munz, "Why can microcracks in ceramics propagate at extremely low stress intensity factors?," *Journal of Materials Science Letters,* vol. 11, pp. 257-60, 1992.

[18] D. C. Cardona and C. J. Beevers, "Formation and growth of short fatigue cracks in a Zirconia-Ceria alloy," *Scripta Metallurgica,* vol. 23, pp. 945-950, 1989.

[19] L. Ewart and S. Suresh, "Crack propagation in ceramics under cyclic loads," *Journal of Materials Science,* vol. 22, pp. 1173-1192, 1987.

[20] S. Suresh, *et al.*, "Fracture toughness measurements in ceramics: Pre-cracking in cyclic compression," *Journal of Materials Science,* vol. 22, pp. 1271-1276, 1987.

[21] R. H. Dauskardt, *et al.*, "Cyclic fatigue-crack growth in a SiC-whisker-reinforced Alumina ceramic composite: long- and small-crack behavior," *Journal of the American Ceramic Society,* vol. 75, pp. 759-771, 1992.

[22] E. Y. Luh, *et al.*, "Cyclic fatigue-crack growth behaviour of short cracks in SiC-reinforced lithium aluminosilicate glass-ceramic composite," *Journal of Materials Science Letters,* vol. 9, pp. 719-725, 1990.

[23] W. B. Choi, *et al.*, "Indentation of metallic and cermet thermal spray coatings," *Journal of Thermal Spray Technology,* vol. 18, pp. 58-64, 2009.

[24] W. B. Choi, *et al.*, "Modified indentation techniques to probe inelasticity in Ni-5%Al coatings from different processes," *Journal of Thermal Spray Technology,* vol. 18, pp. 65-74, 2009.

[25] J. R. Macdonald, *Impedance Spectroscopy: Emphasizing Solid Materials and Systems*: Wiley-Interscience, 1987.

[26] W. D. Cooper, *Electronic Instrumentation and Measurment Techniques*, 2 ed. Englewood Cliffs, NJ: Prentice-Hall, Inc., 1978.

[27] A. Ghabchi, "Electrical methods to characterize defect evolution in plasma sprayed coatings under cyclic straining," Master of Science, Materials Science and Engineering, State University of Newyork at Stony Brook, Stony Brook 2007.

[28] X. Wang, *et al.*, "Determining oxide growth in thermal barrier coatings (TBCs) non-destructively using impedance spectroscopy," *Journal of Materials Science Letters,* vol. 20, pp. 47-49, 2001.

[29] X. Wang, *et al.*, "Non-destructive evaluation of thermal barrier coatings using impedance spectroscopy," *Journal of the European Ceramic Society,* vol. 21, pp. 855-859, 2001.

[30] A. K. Ray, *et al.*, "Damage resistance of a thermal barrier coated superalloy for combustor liners in aero turbines during fatigue and creep," *Canadian Metallurgical Quarterly,* vol. 47, pp. 479-493, Oct 2008.

[31] Z. G. Zhou and Z. T. Chen, "The interaction of two parallel mode-I limited-permeable cracks in a functionally graded piezoelectric material," *European Journal of Mechanics a-Solids,* vol. 27, pp. 824-846, Sep-Oct 2008.

[32] X. Yan, "Numerical analysis of the stress intensity factor for two kinds of mixed-mode crack specimens," *Journal of Strain Analysis for Engineering Design,* vol. 41, pp. 9-18, Jan 2006.

[33]   J. P. Laures and M. Kachanov, "Three-dimensional interactions of a crack front with arrays of penny-shaped microcracks," *International Journal of Fracture,* vol. 48, pp. 255-279, 1991.

[34]   D. F. Li*, et al.*, "A fast and accurate analysis of the interacting cracks in linear elastic solids," *International Journal of Fracture,* vol. 151, pp. 169-185, Jun 2008.

[35]   X. Q. Yan, "Microdefect interacting with a finite main crack," *Journal of Strain Analysis for Engineering Design,* vol. 40, pp. 421-430, Jul 2005.

[36]   X. Yan, "Interaction among three parallel cracks under a uniaxial cyclic load: a boundary element modelling," *Journal of Strain Analysis for Engineering Design,* vol. 41, pp. 121-133, Feb 2006.

[37]   R. H. C. Wong and K. T. Chau, "Crack coalescence in a rock-like material containing two cracks," *International Journal of Rock Mechanics and Mining Sciences,* vol. 35, pp. 147-164, Feb 1998.

[38]   R. B. Stonesifer*, et al.*, "Mixed-mode stress intensity factors for interacting semi-elliptical surface cracks in a plate," *Engineering Fracture Mechanics,* vol. 45, pp. 357-380, 1993.

[39]   K. Kishimoto*, et al.*, "A numerical investigation of the interaction and coalescence of twin coplanar semi-elliptical fatigue cracks," *International Journal of Fatigue,* vol. 11, pp. 91-96, 1989.

[40]   M. Belhouari*, et al.*, "Elastic-plastic analysis of interaction between an interfacial crack and a subinterfacial microcrack in bi-materials," *Computational Materials Science,* vol. 43, pp. 924-929, Oct 2008.

[41]   M. Kamaya, "Growth evaluation of multiple interacting surface cracks. Part I: Experiments and simulation of coalesced crack," *Engineering Fracture Mechanics,* vol. 75, pp. 1336-1349, Apr 2008.

[42]   M. Kamaya, "Growth evaluation of multiple interacting surface cracks. Part II: Growth evaluation of parallel cracks," *Engineering Fracture Mechanics,* vol. 75, pp. 1350-1366, Apr 2008.

[43]   "ANSYS," 11.0 ed. Canonsburg, PA,USA: ANSYS, Inc., 2007.

[44]   R. Pippan*, et al.*, "The influence of crack length on fatigue," *Metallurgical and Materials Transactions A,* vol. 18, pp. 429-435, 1987.

[45]   H. Herman*, et al.*, "Theme article - thermal spray: current status and future trends," *MRS Bulletin* vol. 25, pp. 17-25, 2000.

[46]   X. n. Li*, et al.*, "Application of eddy-current sensor for air gap detection in magnetic suspension motors," in *Electrical Machines and Systems, 2001. ICEMS 2001. Proceedings of the Fifth International Conference on*, 2001, pp. 326-329 vol.1.

[47]   A. C. Tam and H. Sontag, "Measurement of air gap thickness underneath an opaque film by pulsed photothermal radiometry," *Applied Physics Letters,* vol. 49, pp. 1761-1763, 1986.

[48]   D. Lacey*, et al.*, *The effects of an air gap on the measurement of the dielectric constant of SrTiO3 at cryogenic temperatures* vol. 9. Bristol, ROYAUME-UNI: Institute of Physics, 1998.

[49]   FEPA, "Grit sizes for coated abrasives," in *FEPA-standard 43-1984 R 1993*, ed, 2004.

[50]   J. A. Greenwood and J. B. P. Williamson, "Contact of nominally flat surfaces," *Proceedings of the Royal Society of London. Series A. Mathematical and Physical Sciences,* vol. 295, pp. 300-319, December 6, 1966 1966.

[51]   B. Bhushan, "Analysis of the real area of contact between a polymeric magnetic medium and a rigid surface," *Journal of Tribology,* vol. 106, pp. 26-34, 1984.

Appendix A- Finding the Stress Intensity Factor and Total Energy of Two Interacting Cracks

Abstract

The stress intensity factor KI and the total energy of a crack and an arbitrarily located and oriented crack of same size was evaluated through a 2D finite element model using commercial finite element program of ANSYS. A code was written in APDL, ANSYS Programming Design Language to find a wide variety of different distance between crack tips. The results show a maximum of stress intensity factor and total energy when the relative spacing between both crack tips is close enough. There was a sudden decrease after the two crack tips pass each other which is a result of shielding of two cracks.

Introduction

The analytical model uses the diagram in Figure A-1 as reference. The two cracks have same length (2L=2a). The horizontal distance between crack tips is labeled as S and the vertical distance is labeled as h. The purpose of the finite element model is to evaluate the stress intensity factor and the total energy of the system for mode I for various small h and S distances.

89
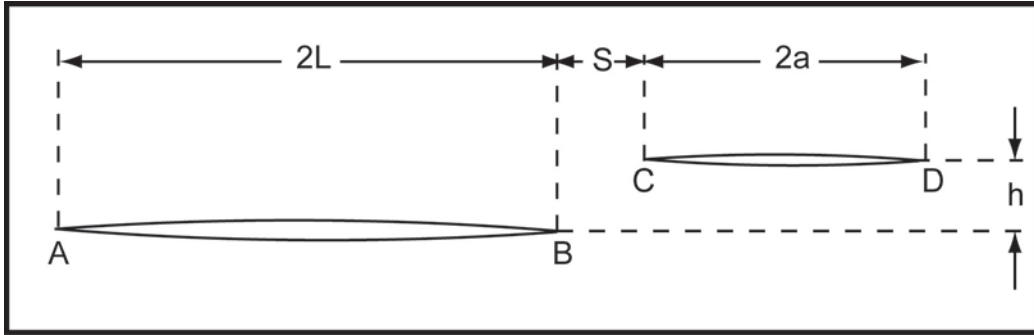
Figure A-1-Two cracks parallel to each other

Method

An ANSYS finite element model is created using PLANE82 type elements. This 8-node element is defined by eight nodes having two degrees of freedom at each node: translations in the nodal x and y directions. The dimensions of the analytical block are 2 meters by 2 meters. Both cracks have a half-length of 10cm (a) and are located at the middle of the block as shown in Figure A-2. The model contains a coarse mesh through most of the model and a fine detailed mesh concentration around both cracks. The distance between two crack was changing by using a code written in APDL, ANSYS Parametric Design Language.

The bottom of the block is fixed and 100Mpa load (σ) is applied at the top of the block. The mode I stress intensity factor of an independent crack with no interaction is calculated using Equation 1. The stress intensity factor is found to be 56.05 MPa m$^{1/2}$.

$$K_I' = \sigma\sqrt{\pi a} \Rightarrow K_I' = 100 \times \sqrt{\pi \times 0.1} = 56.05 \ MPa\sqrt{m} \qquad (46)$$

In a similar matter, the energy of an independent crack with no interaction is calculated by adding the strain energy density of each element. The sum of the strain energy density is independent of meshing type. The energy value of this particular system is found to be 92434.4 J.
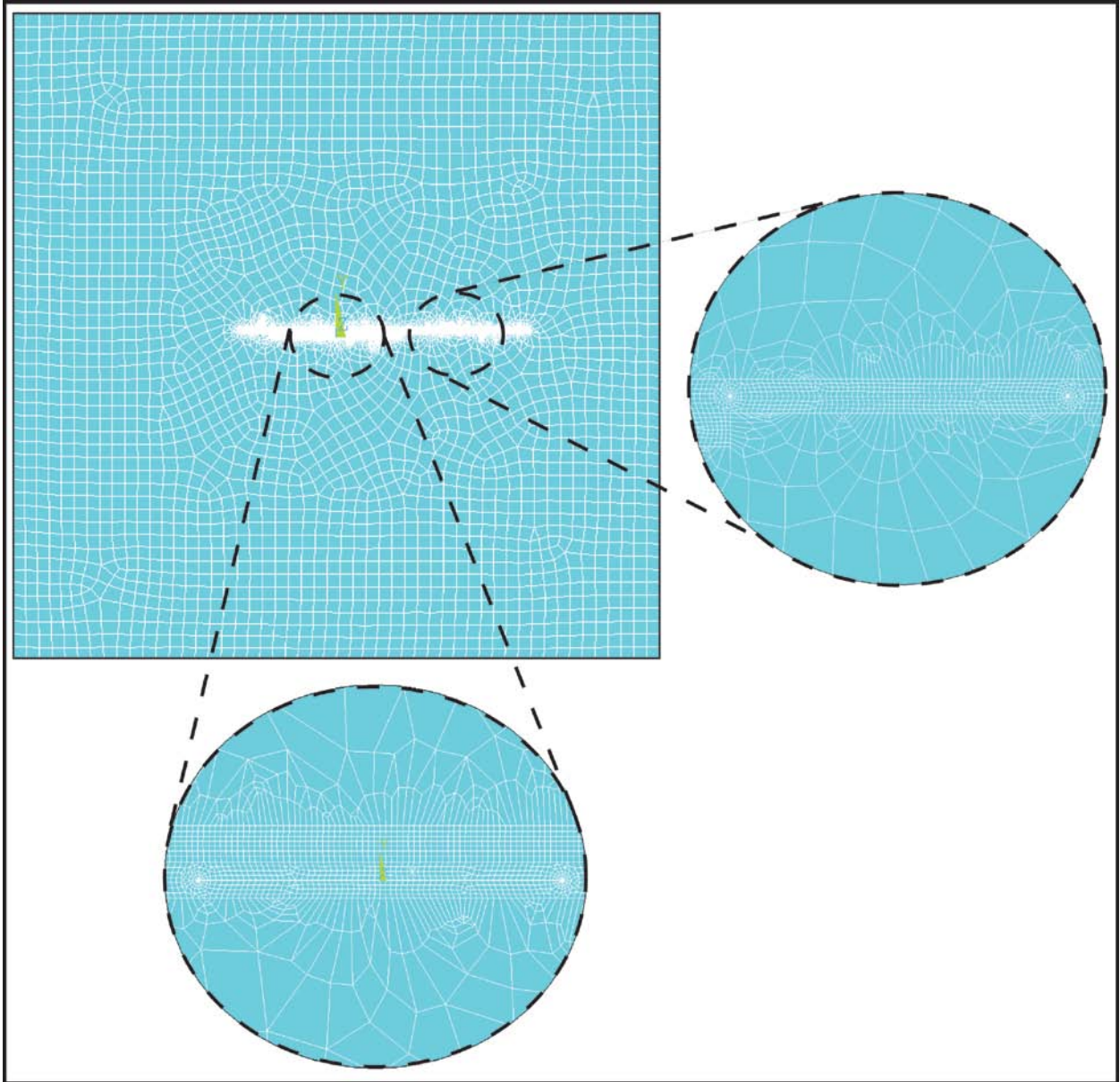
Figure A-2-Meshing

FEM Results

The finite element analysis allows us to obtain the energy of the entire system as well as the Mode I stress intensity factor for all four (A, B, C, and D) crack tips. All results are presented in a non-dimensional form. The total energy of the structure without any cracks in it was subtracted from the two crack energy results, and then was non-dimensionalized by dividing it to energy of one crack.

$$\bar{U} = \frac{U^{**} - U}{U^* - U} \tag{47}$$

where $\bar{U}$ is non-dimensional energy, U^{**} is energy of two cracks, U^* is energy of one crack, and U is energy of the structure without any crack.

The non-dimensional energy of the system is equal to 1.4 when both cracks are well apart from each other, whether they are apart in the horizontal (S) or vertical direction (h). The energy increases as the relative distance in either direction (S or h) becomes closer, reaching its maximum at h→0 and S/l≈ -0.2 as shown in Figure A-3. The maximum non-dimensional energy for different relative distance is shown in Table 8.
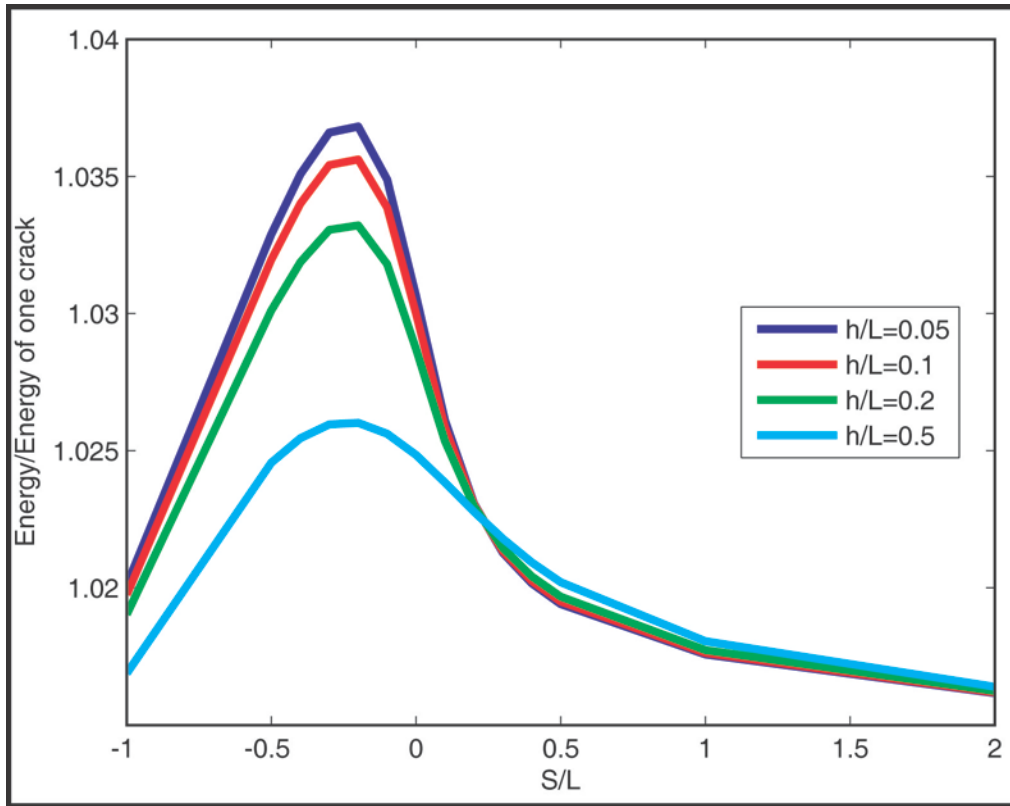
Figure A-3-Non-dimensional energy of a crack pair for a/L=1

Table 8-Non-dimensional Maximum Energy of a crack pair for a/L=1

h/L	S/L	Non-dimensional energy
0.05	-0.2	1.93317
0.1	-0.2	1.90276
0.2	-0.2	1.84195
0.5	-0.2	1.6595

The analysis shows the stress intensity factor for outer crack tips A and D are the same. Although they do not interact directly with another crack tip they do show an increase of their stress intensity factor compared to an independent crack as seen in Figure A-4 and Figure A-5. In a similar matter seen with the energy graph, the stress intensity factor increases as the relative distance in either direction (S or h) becomes

93

closer, reaching its maximum at h→0 and S/L≈ -0.4 as shown in Figure A-4 and Figure A-5.
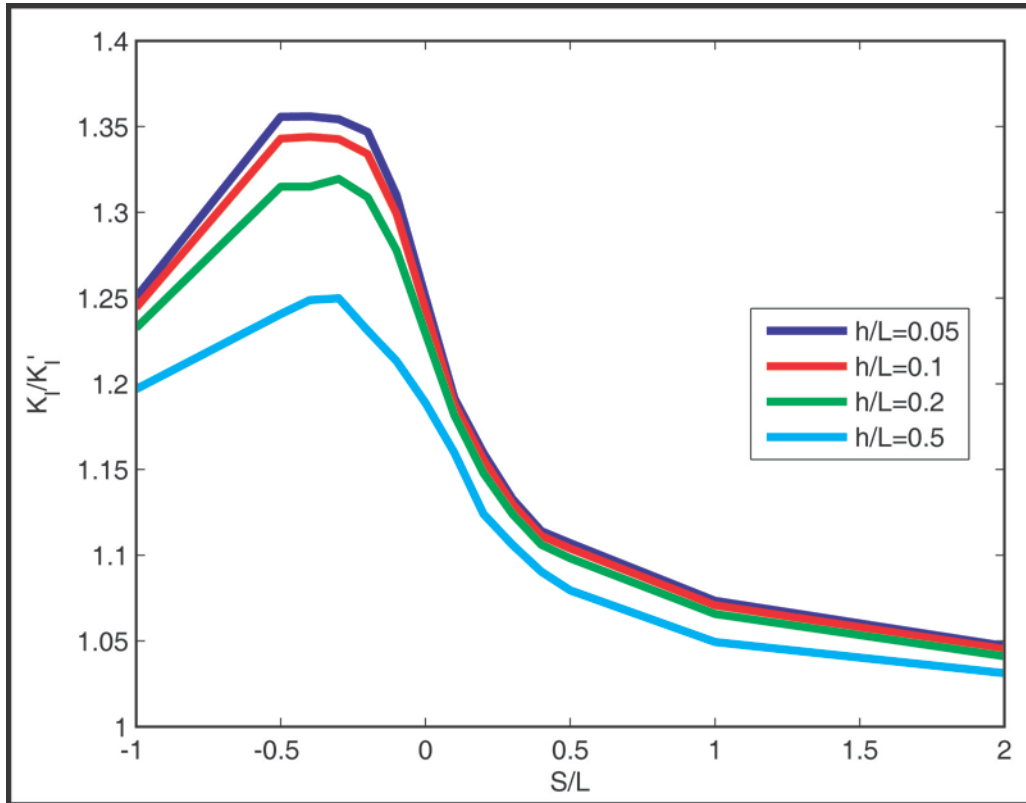
Figure A-4-Non-dimensional K$_I$ of point A for a/L=1

The maximum non-dimensional stress intensity factor for outer crack tips for different relative distance is shown in Table 9.

Table 9- Non-dimensional K$_I$ of a crack pair for a/L=1

h/L	S/L	K_I/ K_I' of point A	K_I/ K_I' of point D
0.05	-0.4	1.35588	1.35588
0.1	-0.4	1.34398	1.34398
0.2	-0.3	1.31948	1.32020
0.5	-0.3	1.24990	1.24990
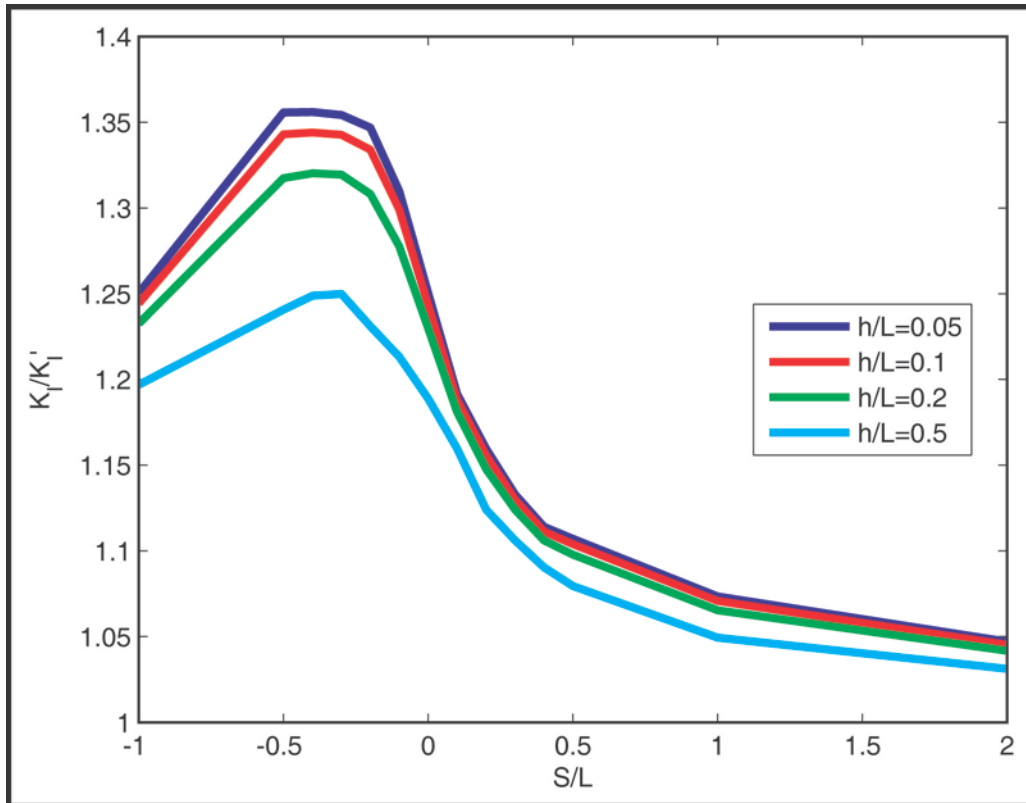
Figure A-5-Non-dimensional K$_I$ of point D for a/L=1

The point of interest for this analysis is the effect on the inner crack tips B and C. Those two crack tips have a direct interaction between each other, causing to experiment a much greater SIF K$_I$ as they approach each other. The analysis shows the SIF for inner crack tips B and C are the same. In a similar matter seen with the SIF of outer crack tips and energy graph, the stress intensity factor increases as the relative distance in either direction (S or h) becomes closer, reaching its maximum at h→0 and S≈0 as shown in Figure A-6 and Figure A-7. However, as the two cracks become almost parallel to each other the SIF approaches 0. Based on an existing report from Kamaya [2] the SIF reaches its minimum almost at S = -a and then approaching 1 at S = -2a.

The maximum non-dimensional stress intensity factor for inner crack tips for different relative distance is shown in Table 10.
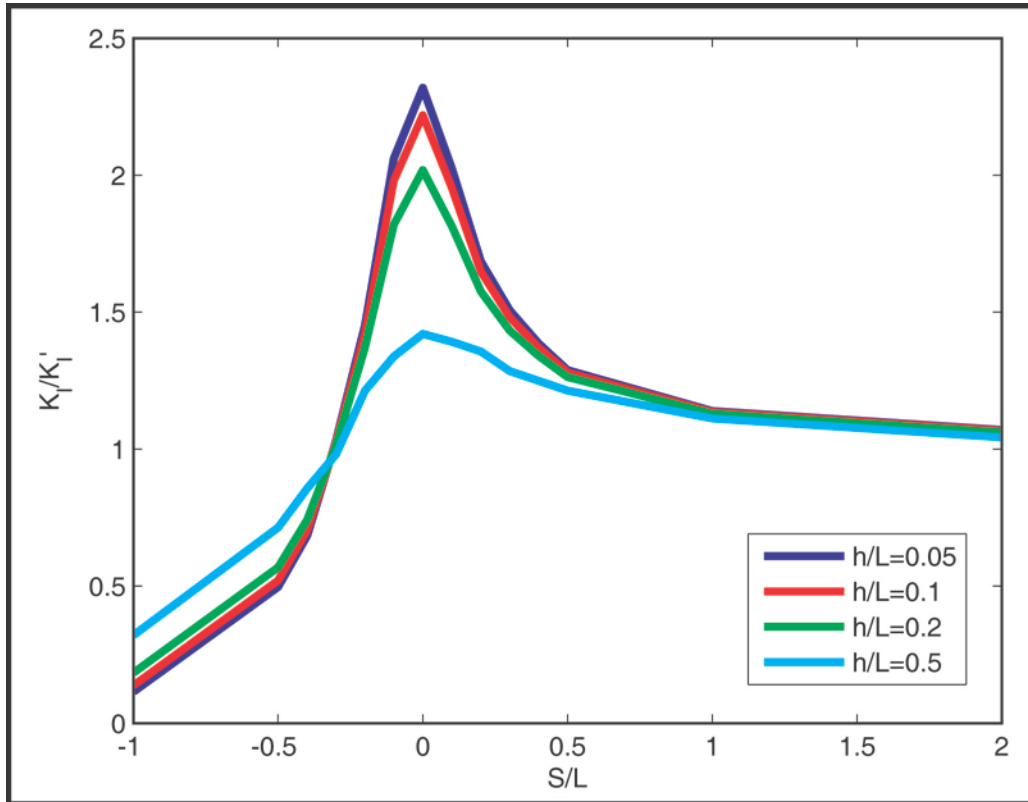
Figure A-6-Non-dimensional K_I of point B for a/L=1
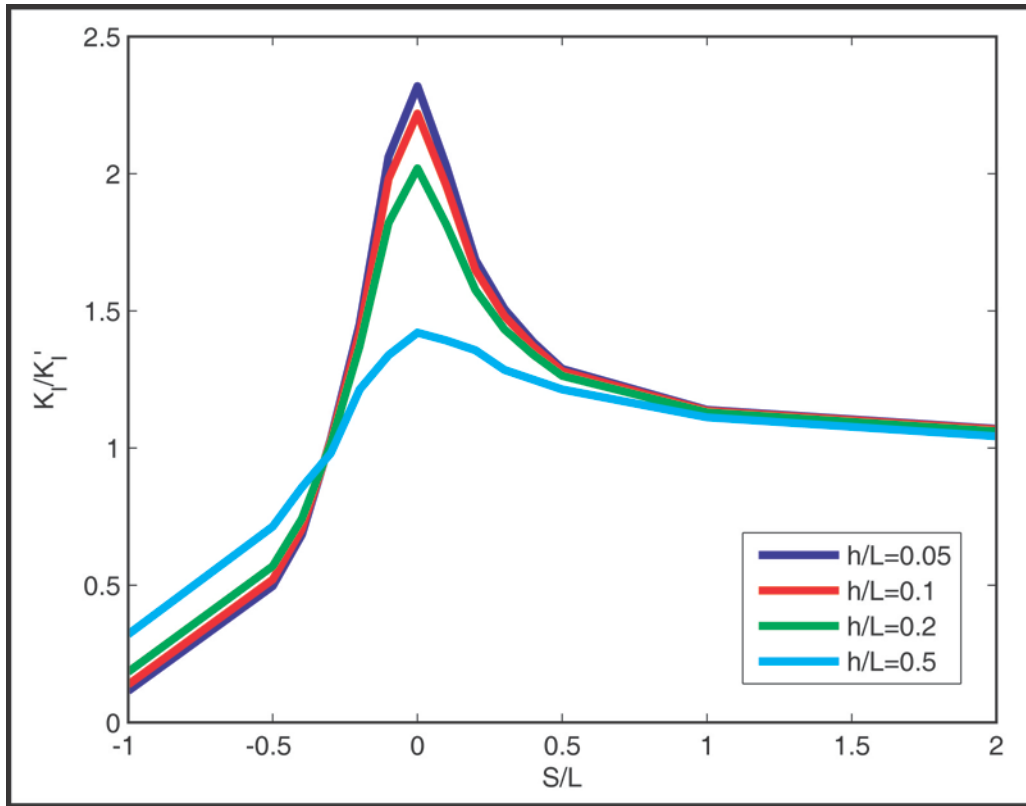
Figure A-7-Non-dimensional K_I of point C for a/L=1

Table 10- Non-dimensional K_I of a crack pair for a/L=1

h/L	S/L	K_I/K_I' of point A	K_I/K_I' of point D
0.05	0	2.31855	2.31855
0.1	0	2.21873	2.21873
0.2	0	2.0182	2.01909
0.5	0	1.42016	1.42016

Discussion

The maximum change for non-dimensional energy of a system with two cracks when their relative distance (h/L=0.05 and S/L = -0.25) is close is found to be 1.93-

1.4=53% higher than an independent crack. The maximum change for non-dimensional SIF of the two outer crack tips when their relative distance (h/L=0.05 and S/L = -0.4) is close is found to be 35% higher than an independent crack.

Finally, the maximum change for non-dimensional SIF of the two inner crack tips when their relative distance (h/L=0.05 and S = 0) is close is found to be 140% higher than an independent crack.

References

[1]   Kamaya*, et al.*, "Growth evaluation of multiple interacting surface cracks. Part I: Experiments and simulation of coalesced crack," *Engineering Fracture Mechanics,* vol. 75, pp. 1336-1349, 2008.
[2]   Kamaya*, et al.*, "Growth evaluation of multiple interacting surface cracks. Part II: Growth evaluation of parallel cracks", *Engineering Fracture Mechanics,* vol. 75, pp. 1350-1366, 2008.
[3]   Belhouari M*, et al.*, "Elastic-plastic analysis of interaction between an interfacial crack and a subinterfacial microcrack in bi-materials," *Computational material Science*, vol. 43, pp. 924-929, 2008.

Appendix B- Stable Crack Growth in Thermal Spray Thick Coating Detected via Capacitance Measurements

Abstract

We report permanent changes in dielectric behavior of thermal sprayed YSZ coatings during in-plane cyclic straining. This occurs within 100 cycles under 1000 microstrain loading, and is interpreted as an increase in internal crack area during Paris-Law type stable growth. Results from FEM crack interaction and capacitance models, with consideration of a randomly-distributed network of short crack pairs support this theory.

Introduction

Thermal spray (TS) coatings and materials including thermal barrier, tribological and anti-corrosive coatings have established application across a number of engineering fields [1]. TS is attractive for these systems due to its low cost, ability to coat large areas and flexibility in material feedstock. These attributes, along with improvements in process diagnostics have spurred the exploration of TS for more functional applications including fuel cells [2], conformal electronic sensors [3, 4], biomedical implants [5] and perhaps stretchable electronics [6]. Successful implementation of TS coatings in these systems will require more robust characterization of their mechanical behavior; to date this has been limited and in practice most measurements are carried out in a pass/fail manner [7]. Little is known about the intrinsic or progressive behavior of the coatings under repeated loading. This is important as the microstructure of TS coatings comprises layers of micron-thick flattened particles ('splats') separated by interfaces, the bonding

100

between which is not well understood [8-9]. These interfaces represent potential short crack growth sites throughout the material.

Method

We deposited TS YSZ coatings (0.20 – 0.40 mm thick) on tapered cantilever Al substrates (3.1 mm thick) using atmospheric plasma spray (APS) (particle T = 2500°C; 7MB APS torch - Sulzer Metco, Inc., Westbury, NY) using N_2-H_2 plasma with a laminar gas flow. Substrates were cleaned with acetone and grit-blasted prior to spraying. Each coated substrate was placed in a glove box maintained at 50% relative humidity, where it remained for all subsequent tests and measurements. Through-thickness capacitance of coatings on metal substrates was measured using a parallel-plate set up on an impedance analyzer operating at 1KHz (HP 4294A precision impedance analyzer and HP 16451B Dielectric test fixture attachment), at five locations along the cantilever length. This value was converted to dielectric constant using $\epsilon_r = t_a \, C_P / (A \, \epsilon_0)$ where ϵ_r is dielectric constant, t_a is average thickness of coating, C_P is capacitance, A is area of electrodes, and $\epsilon_0 = 8.85e\text{-}12$ F/m. As the goal was to ascertain damage, capacitance was measured on as-sprayed, unpolished coating surfaces. Coatings were then strained in-plane by bending the cantilever substrates on a custom-built apparatus. It was assumed that strain in the relatively thin coating was equal to substrate surface strain, and given by the formula for a tapered cantilever $\varepsilon = \delta * t / L^2$, where δ is deflection, t is thickness and L is length, (Figure B-1). In this way coatings were cycled from 0 to 1000 μstrain, placing the coating in

tension, up to 20000 times at 1 cycle per second. Every 1000 cycles, cycling was stopped and capacitance measured.
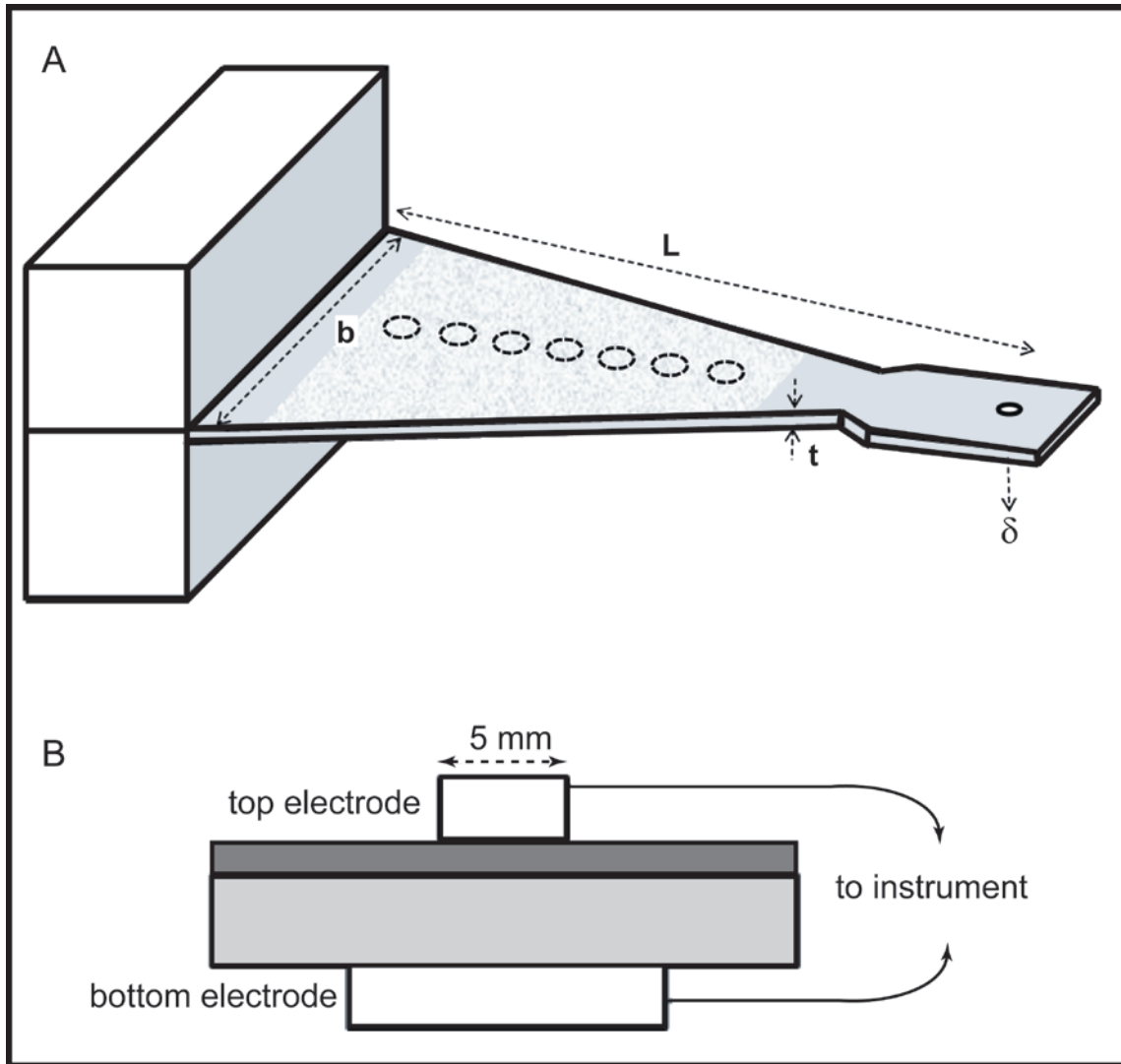
Figure B-1-Schematic of the testing apparatus (Dashed circles are where capacitance measurements were taken).

Figure B-2 shows representative changes in dielectric constant during the experiments. It significantly increases from an initial value of approximately 8.6 over the

first few hundred cycles, and then approaches a constant value of 10.2 after several thousand cycles. The data for tension cycling had the same trend for tension-compression and compression loading. Error bars show that the changes in dielectric constant were significant relative to instrument and measurement noise. That is to say, measurements taken several hours after the mechanical cycling showed no change.
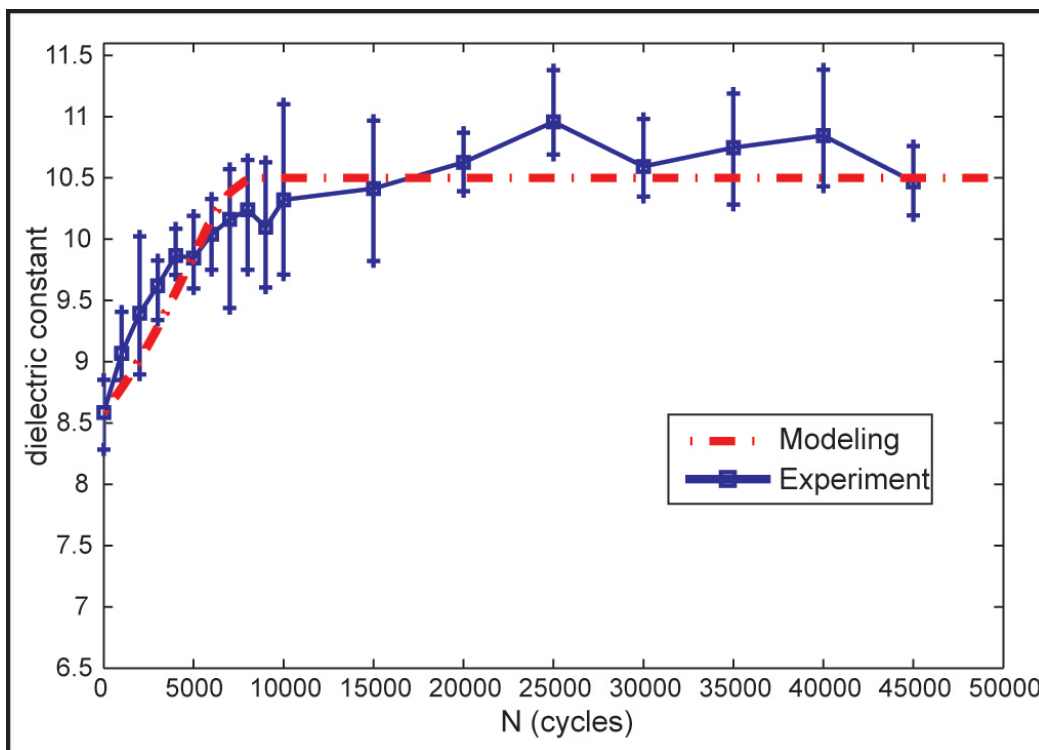
Figure B-2-Change in effective dielectric constant with cycling, for experiments and models explained in text.

Results

We interpret the salient observations by considering the architecture of a TS material a schematic of which is displayed in Figure B-3. A typical TS coating consists of rapidly-quenched lamellae (1 µm thickness and 100 µm width) with incomplete splat-splat bonded regions producing in-plane 'cracks' (lamellar interfaces of << 1µm thickness, denoted as cracks in this letter for brevity). In addition, globular pores are present [1, 7-8]. Globular pores are mainly closed, and filled with air, but cracks are open and susceptible to humidity penetration and water surface adsorption. Dielectric constant values are low relative to bulk YSZ (24) but can be rationalized by considering surface roughness, Niesel's equation for a porous material [10], and short cracks with surface-adsorbed water. As the dielectric constant increases with cycling, we hypothesize that we are seeing the growth of short, 'wet' cracks.
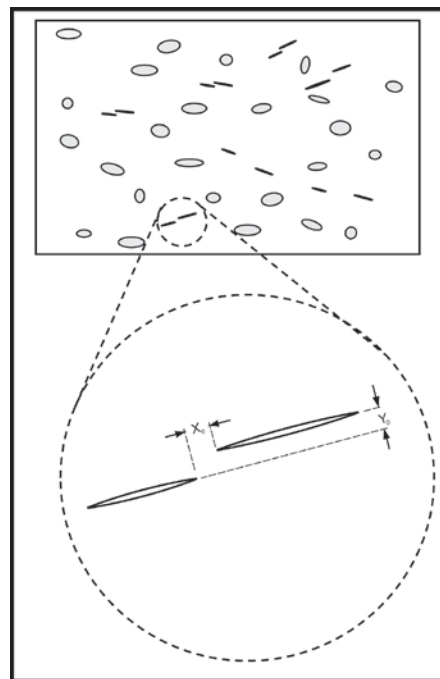
Figure B-3-Schematic of crack pairs simulated in model.

We performed 3D FEM calculations in ANSYS to calculate effective dielectric constant of such a structure, using values of $\epsilon_r = 12$ for the bulk *porous* ceramic, $\epsilon_r = 1$ for air and $\epsilon_r = 80$ for water. For brevity we do not describe all the results here, but salient points are (i) an initial value of $\epsilon_r = 8.6$ can readily be obtained for such a structure with a 'wet' crack porosity of 4 %; (ii) size distribution of globular pores, or thickness distribution of cracks (i.e. 10 cracks 0.001 mm thick vs 1 crack 0.01 mm thick) makes little difference in overall dielectric constant; (iii) within a fairly large range, dielectric constant is linear with crack area. This is perhaps not surprising. We found that an effective dielectric constant change from 8.6 to 10.5 could be obtained via an average 'wet' crack length change from 4µm to 18 µm. Initial crack lengths of 4µm have been observed in ceramic TS materials, via cross-sectional analysis [8], and scattering methods [9]. Coating architecture is dependent upon process [11], but the values here are quite reasonable and representative.

Accepting that dielectric constant is linear with crack area, and assuming cracks grow in a single direction, it follows that self-arresting fatigue behavior is likely responsible for the asymptotic behavior in Figure B-2. This is similar to the literature discussion of short cracks and similitude breakdown in bulk metals [12-13], ceramics [14-15] and composites [16], for which a number of size-dependent mechanisms have been discussed. For TS materials, we suggest that the 'size-effect' comes from the interaction of crack stress field with neighboring defects in the material, and present a simple model to illustrate. Cracks in a TS material can be treated as pairs (Figure B-3) with tips separated by a horizontal distance x_o and a vertical distance y_o; the latter is of similar magnitude to splat thickness (1µm). From micrographs, we see that cracks are

not perfectly horizontal, but are tilted at 5-15 degrees. Crack interaction for pairs has been modeled in a number of systems, but largely under mode I loading, normal to crack faces [17]. Here we modeled single crack pairs in ANSYS, to extract mode I and mode II stress intensity factors (SIF) for different stages of crack approach and overlap, under in-plane tensile loading. Cracks were constrained to grow in-plane. For ANSYS, K_I and K_{II} were derived using the virtual crack extension integral method, and then normalized with respect to K_I or K_{II} of an isolated crack of the same length *a*. Results are shown in Figure B-4a. Both stress intensity factors (SIF) have similar trends, regardless of crack orientation, and salient characteristics are: (i) as the crack tips approach, SIF increases significantly and (ii) upon overlap SIF decreases to near-zero values, due to crack shielding. Considering Paris-type growth of both cracks [18], we can input SIF as applied ΔK into the relation $da/dN = C\Delta K^m$, to obtain crack growth as a function of stress cycles (Figure B-4b). Results here are shown for specific values of C and m, but the trends are general. A slow initial crack growth phase is followed by rapid growth upon approach and arrest upon overlap. This behavior does not precisely match our experiments, but if we now consider the average growth of 100 crack pairs within a structure (Figure B-4b), the asymptotic behavior appears quite clearly. Further, if we consider the dielectric values given above, and an average starting crack length of 4 µm, and Paris law constants of $C = 1e^{-7}$ and m = 1, we match the experimental data quite closely.
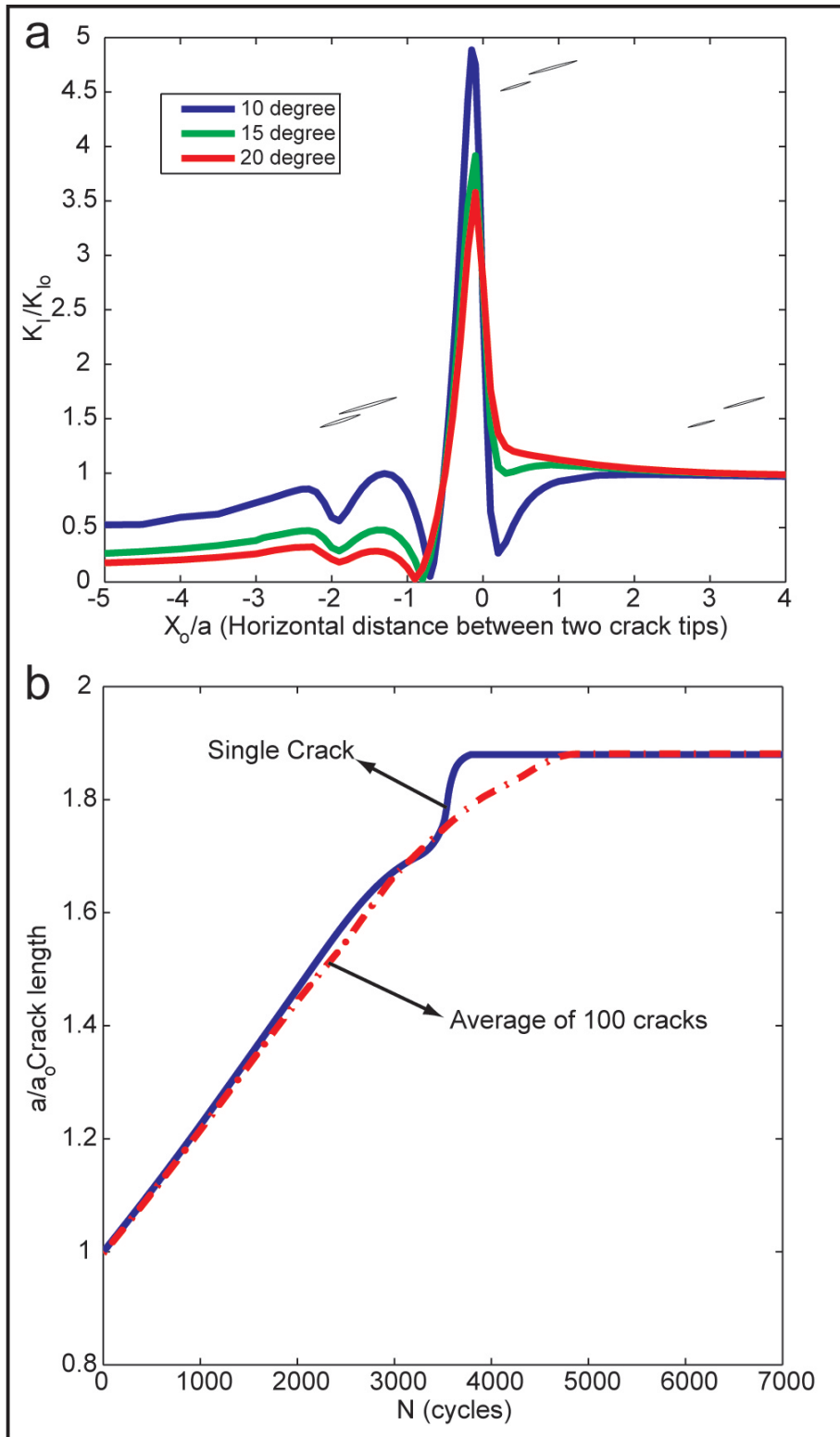
Figure B-4-Predicted change in crack face length for (solid line) single crack pair, (dashed line) 100 randomly oriented crack pairs.

Discussion

The C value is high, but similar to that in short crack behavior, prior to arrest. More systematic experiments could be used to develop a method to measure fatigue parameters of a variety of coatings, but here we have (i) described the propensity of ceramic TS coatings to undergo crack growth under nominally elastic strains (ii) proposed a mechanism for such growth and (iii) identified a potential measurement method for crack initiation and growth behavior, for applications where prime reliance is required. This consideration could also explain the high-reliability associated with coatings deposited with nano-scale powder, for which no such 'size effect' would be manifested, as crack fields would interact immediately.

References

[1] H. Herman, *et al.*, "Theme article - thermal spray: current status and future trends," *MRS Bulletin* vol. 25, pp. 17-25, 2000.

[2] R. Hui, *et al.*, "High performance metal-supported solid oxide fuel cells fabricated by thermal spray," *Journal of Power Sources,* vol. 191, pp. 371-376, 2009.

[3] Q. Chen, *et al.*, "Novel sensor fabrication using direct-write thermal spray and precision laser micromachnining," *Journal of Manufacturing Science and Engineering-Transactions of the Asme,* vol. 126, pp. 830-836, 2004.

[4] S. Sampath, *et al.*, "Direct-write thermal spraying of multilayer electronics and sensor structures," in *Direct-Write Technologies for Rapid Prototyping*, ed San Diego: Academic Press, 2002, pp. 261-302.

[5] P. L. Tranquilli*, et al.*, "Evaluation of different preparations of plasma-spray hydroxyapatite coating on titanium alloy and duplex stainless steel in the rabbit " *Journal of Materials Science-Materials in Medicine,* vol. 5, pp. 345-349, 1994.

[6] J. A. Rogers*, et al.*, "Materials and mechanics for stretchable electronics," *Science,* vol. 327, pp. 1603-1607, March 26, 2010 2010.

[7] R. Ahmed and M. Hadfield, "Mechanisms of fatigue failure in thermal spray coatings," *Journal of Thermal Spray Technology,* vol. 11, pp. 333-349, 2002.

[8] E. Turunen*, et al.*, "On the role of particle state and deposition procedure on mechanical, tribological and dielectric response of high velocity oxy-fuel sprayed alumina coatings," *Materials Science and Engineering a-Structural Materials Properties Microstructure and Processing,* vol. 415, pp. 1-11, 2006.

[9] A. A. Kulkarni*, et al.*, "Advanced microstructural characterization of plasma-sprayed zirconia coatings over extended length scales," *Journal of Thermal Spray Technology,* vol. 14, pp. 239-250, 2005.

[10] T. T. Fang*, et al.*, "Effects of pore morphology and grain size on the dielectric properties and tetragonal; 2013; cubic phase transition of high-purity Barium Titanate," *Journal of the American Ceramic Society,* vol. 76, pp. 1205-1211, 1993.

[11] Y. Li*, et al.*, "Process-controlled plasma-sprayed Yttria-Stabilized Zirconia coatings: new insights from ultrasmall-angle X-ray scattering," *Journal of the American Ceramic Society,* vol. 92, pp. 491-500, 2009.

[12] S. Suresh, *Fatigue of Materials*, 2nd ed.: Cambridge University Press, 1998.

[13] S. Pearson, "Initiation of fatigue cracks in commercial aluminium alloys and the subsequent propagation of very short cracks," *Engineering Fracture Mechanics,* vol. 7, pp. 235-240, IN15-IN18, 241-247, 1975.

[14] C. J. Gilbert*, et al.*, "Anomalous cyclic fatigue-crack propagation behavior of small cracks in monolithic, grain-bridging ceramics," *Ceramics International,* vol. 26, pp. 721-725, 2000.

[15] D. C. Cardona and C. J. Beevers, "Formation and growth of short fatigue cracks in a Zirconia-Ceria alloy," *Scripta Metallurgica,* vol. 23, pp. 945-950, 1989.

[16] R. H. Dauskardt*, et al.*, "Cyclic fatigue-crack growth in a SiC-whisker-reinforced Alumina ceramic composite: long- and small-crack behavior," *Journal of the American Ceramic Society,* vol. 75, pp. 759-771, 1992.

[17] Y. Murakami, *Stress Intensity Factors Handbook*, 1 ed.: Pergamon, 1987.

[18] T. Fett and D. Munz, "Why can microcracks in ceramics propagate at extremely low stress intensity factors?," *Journal of Materials Science Letters,* vol. 11, pp. 257-60, 1992.

Appendix C- ANSYS Parametric Design Language (APDL) Code for Finding the Stress Intensity Factor of a Pair of Cracks

Attached is the ANSYS APDL code that was used to find the Stress intensity factor and total energy of the structure.

```
/BATCH
FINISH
PARSAV,,,,
/clear,nostart
PARRES,, ,,
!********** "a" is the first crack length which is called "L" in some papers ***********
!********* "a2" is the second crack length which is called "a" in some papers ***********
*SET,a,0.1                              !*********** First crack dimension **************
*SET,a2,1*a                             !*********** Second crack dimension ***********
*SET,h,0.2*a                            !******* Vertical distance between two cracks ****
*SET,S,1*a                              !**** Horizontal  distance between two cracks *****
/PREP7
ET,1,PLANE82                            !************* Element Type  ****************
KEYOPT,1,3,2
KEYOPT,1,5,0
KEYOPT,1,6,0
MPTEMP,,,,,,,,
MPTEMP,1,0
MPDATA,EX,1,,200e9                      !******** Modulus of elasticity *********
MPDATA,PRXY,1,,0.3                      !******** Poisson's ratio **************
*DIM,X,ARRAY,2,1
*DIM,Y,ARRAY,2,1
*DIM,K,ARRAY,1,3
*SET,tt,0.017453*0                      !*** ******** First crack  angle *************
!********************** first crack location  ************************
*SET,X(1,1),0
*SET,Y(1,1),0
!*********************** first Crack Keypoints *******************
*SET,II,1
K,(II-1)*16+1,X(II,1)+cos(tt)*0-sin(tt)*a/1000,Y(II,1)+sin(tt)*0+cos(tt)*a/1000,,
K,(II-1)*16+2,X(II,1)+cos(tt)*14*a/15-sin(tt)*a/1000,Y(II,1)+sin(tt)*14*a/15+cos(tt)*a/1000,,
K,(II-1)*16+3,X(II,1)+cos(tt)*a-sin(tt)*0,Y(II,1)+sin(tt)*a+cos(tt)*0,,
K,(II-1)*16+4,X(II,1)+cos(tt)*14*a/15-sin(tt)*(-a/1000),Y(II,1)+sin(tt)*14*a/15+cos(tt)*(-a/1000),,
K,(II-1)*16+5,X(II,1)+cos(tt)*0-sin(tt)*(-a/1000),Y(II,1)+sin(tt)*0+cos(tt)*(-a/1000),,
```

K,(II-1)*16+6,X(II,1)+cos(tt)*0-sin(tt)*(-h/2),Y(II,1)+sin(tt)*0+cos(tt)*(-h/2),,

K,(II-1)*16+7,X(II,1)+cos(tt)*2*a-sin(tt)*(-h/2),Y(II,1)+sin(tt)*2*a+cos(tt)*(-h/2),,

K,(II-1)*16+8,X(II,1)+cos(tt)*2*a-sin(tt)*0,Y(II,1)+sin(tt)*2*a+cos(tt)*0,,

K,(II-1)*16+9,X(II,1)+cos(tt)*2*a-sin(tt)*(h/2),Y(II,1)+sin(tt)*2*a+cos(tt)*(h/2),,

K,(II-1)*16+10,X(II,1)+cos(tt)*0-sin(tt)*(h/2),Y(II,1)+sin(tt)*0+cos(tt)*(h/2),,

K,(II-1)*16+11,X(II,1)+cos(tt)*(-2*a)-sin(tt)*(h/2),Y(II,1)+sin(tt)*(-2*a)+cos(tt)*(h/2),,

K,(II-1)*16+12,X(II,1)+cos(tt)*(-2*a)-sin(tt)*0,Y(II,1)+sin(tt)*(-2*a)+cos(tt)*0,,

K,(II-1)*16+13,X(II,1)+cos(tt)*(-2*a)-sin(tt)*(-h/2),Y(II,1)+sin(tt)*(-2*a)+cos(tt)*(-h/2),,

K,(II-1)*16+14,X(II,1)+cos(tt)*(-14*a/15)-sin(tt)*(-a/1000),Y(II,1)+sin(tt)*(-14*a/15)+cos(tt)*(-a/1000),,

K,(II-1)*16+15,X(II,1)+cos(tt)*(-a)-sin(tt)*0,Y(II,1)+sin(tt)*(-a)+cos(tt)*0,,

K,(II-1)*16+16,X(II,1)+cos(tt)*(-14*a/15)-sin(tt)*a/1000,Y(II,1)+sin(tt)*(-14*a/15)+cos(tt)*a/1000,,

!********************** Second crack location & angle ************************

*SET,tt,0.017453*0

*SET,x2,a+S+a2+X(1,1)

*SET,y2,h+Y(1,1)

!********************** Second crack location ************************

*SET,X(2,1),x2

*SET,Y(2,1),y2

!*************************** Second Crack Keypoints *********************

*SET,II,2

K,(II-1)*16+1,X(II,1)+cos(tt)*0-sin(tt)*a/1000,Y(II,1)+sin(tt)*0+cos(tt)*a/1000,,

K,(II-1)*16+2,X(II,1)+cos(tt)*(a2-a/15)-sin(tt)*a/1000,Y(II,1)+sin(tt)*(a2-a/15)+cos(tt)*a/1000,,

K,(II-1)*16+3,X(II,1)+cos(tt)*a2-sin(tt)*0,Y(II,1)+sin(tt)*a2+cos(tt)*0,,

K,(II-1)*16+4,X(II,1)+cos(tt)*(a2-a/15)-sin(tt)*(-a/1000),Y(II,1)+sin(tt)*(a2-a/15)+cos(tt)*(-a/1000),,

K,(II-1)*16+5,X(II,1)+cos(tt)*0-sin(tt)*(-a/1000),Y(II,1)+sin(tt)*0+cos(tt)*(-a/1000),,

K,(II-1)*16+6,X(1,1)+cos(tt)*(3*a)-sin(tt)*(h/2),Y(1,1)+sin(tt)*(3*a)+cos(tt)*(h/2),,

K,(II-1)*16+7,X(1,1)+cos(tt)*6*a-sin(tt)*(h/2),Y(1,1)+sin(tt)*6*a+cos(tt)*(h/2),,

K,(II-1)*16+8,X(1,1)+cos(tt)*6*a-sin(tt)*h,Y(1,1)+sin(tt)*6*a+cos(tt)*h,,

K,(II-1)*16+9,X(1,1)+cos(tt)*6*a-sin(tt)*3*(h/2),Y(1,1)+sin(tt)*6*a+cos(tt)*3*(h/2),,

K,(II-1)*16+10,X(1,1)+cos(tt)*(3*a)-sin(tt)*(3*h/2),Y(1,1)+sin(tt)*(3*a)+cos(tt)*(3*h/2),,

K,(II-1)*16+11,X(1,1)+cos(tt)*(-3*a)-sin(tt)*3*(h/2),Y(1,1)+sin(tt)*(-3*a)+cos(tt)*3*(h/2),,

K,(II-1)*16+12,X(1,1)+cos(tt)*(-3*a)-sin(tt)*h,Y(1,1)+sin(tt)*(-3*a)+cos(tt)*h,,

K,(II-1)*16+13,X(1,1)+cos(tt)*(-3*a)-sin(tt)*(h/2),Y(1,1)+sin(tt)*(-3*a)+cos(tt)*(h/2),,

K,(II-1)*16+14,X(II,1)+cos(tt)*(-(a2-a/15))-sin(tt)*(-a/1000),Y(II,1)+sin(tt)*(-(a2-a/15))+cos(tt)*(-a/1000),,

K,(II-1)*16+15,X(II,1)+cos(tt)*(-a2)-sin(tt)*0,Y(II,1)+sin(tt)*(-a2)+cos(tt)*0,,

K,(II-1)*16+16,X(II,1)+cos(tt)*(-(a2-a/15))-sin(tt)*a/1000,Y(II,1)+sin(tt)*(-(a2-a/15))+cos(tt)*a/1000,,

```
*DO,II,1,2
!************************* Crack Areas *********************
LSTR,      (II-1)*16+1,      (II-1)*16+2
LSTR,      (II-1)*16+2,      (II-1)*16+3
LSTR,      (II-1)*16+3,      (II-1)*16+4
LSTR,      (II-1)*16+4,      (II-1)*16+5
LSTR,      (II-1)*16+5,      (II-1)*16+6
LSTR,      (II-1)*16+6,      (II-1)*16+7
LSTR,      (II-1)*16+7,      (II-1)*16+8
LSTR,      (II-1)*16+8,      (II-1)*16+9
LSTR,      (II-1)*16+9,     (II-1)*16+10
LSTR,     (II-1)*16+10,      (II-1)*16+1
LSTR,      (II-1)*16+5,     (II-1)*16+14
LSTR,     (II-1)*16+14,     (II-1)*16+15
LSTR,     (II-1)*16+15,     (II-1)*16+16
LSTR,     (II-1)*16+16,      (II-1)*16+1
LSTR,     (II-1)*16+10,     (II-1)*16+11
LSTR,     (II-1)*16+11,     (II-1)*16+12
LSTR,     (II-1)*16+12,     (II-1)*16+13
LSTR,     (II-1)*16+13,      (II-1)*16+6
FLST,2,10,4
FITEM,2,(II-1)*18+1
FITEM,2,(II-1)*18+2
FITEM,2,(II-1)*18+3
FITEM,2,(II-1)*18+4
FITEM,2,(II-1)*18+5
FITEM,2,(II-1)*18+6
FITEM,2,(II-1)*18+7
FITEM,2,(II-1)*18+8
FITEM,2,(II-1)*18+9
FITEM,2,(II-1)*18+10
AL,P51X
FLST,2,10,4
FITEM,2,(II-1)*18+11
FITEM,2,(II-1)*18+12
FITEM,2,(II-1)*18+13
FITEM,2,(II-1)*18+14
```

```
FITEM,2,(II-1)*18+15
FITEM,2,(II-1)*18+16
FITEM,2,(II-1)*18+17
FITEM,2,(II-1)*18+18
FITEM,2,(II-1)*18+10
FITEM,2,(II-1)*18+5
AL,P51X
*ENDDO
!******************** Main Frame and crack areas ********************
RECTNG,-1,1,-1,1,
LSTR,    25,    27
LSTR,    27,    29
LSTR,    29,    11
LSTR,    11,    13
LSTR,    13,     7
LSTR,     7,     9
LSTR,     9,    23
LSTR,    23,    25
FLST,2,9,4
FITEM,2,27
FITEM,2,33
FITEM,2,42
FITEM,2,43
FITEM,2,44
FITEM,2,45
FITEM,2,46
FITEM,2,47
FITEM,2,48
AL,P51X
!***************************** Subtracting Crack areas *****************************
ASBA,    5,     6
!******************** Crack Areas Glue  to each other and the main frame ********************
WPSTYLE,,,,,,,,0
FLST,2,5,5,ORDE,3
FITEM,2,1
FITEM,2,-4
FITEM,2,7
```

```
AGLUE,P51X
!***************************** mesh size **********************************
!*********************** Crack 1 mesh size ********************************
FLST,2,4,5,ORDE,3
FITEM,2,1
FITEM,2,-3
FITEM,2,5
FLST,2,2,5,ORDE,2
FITEM,2,1
FITEM,2,-2
AESIZE,P51X,a/32,
KSCON,3,a/30,1,16,0,
KSCON,15,a/30,1,16,0,
!********************** crack 2 mesh size ********************************
FLST,2,2,5,ORDE,2
FITEM,2,3
FITEM,2,5
AESIZE,P51X,a/32,
KSCON,16+3,a/30,1,16,0,
KSCON,16+15,a/30,1,16,0,
!******************* Frame mesh size    ****************************
FLST,2,1,5,ORDE,1
FITEM,2,6
AESIZE,P51X,0.04,
MSHKEY,0
!***************************** Meshing *************************
MSHKEY,0
CM,_Y,AREA
ASEL, , , ,     5
CM,_Y1,AREA
CHKMSH,'AREA'
CMSEL,S,_Y
AMESH,_Y1
CMDELE,_Y
CMDELE,_Y1
CMDELE,_Y2
MSHKEY,0
```

```
CM,_Y,AREA
ASEL, , , ,      3
CM,_Y1,AREA
CHKMSH,'AREA'
CMSEL,S,_Y
AMESH,_Y1
CMDELE,_Y
CMDELE,_Y1
CMDELE,_Y2
MSHKEY,0
CM,_Y,AREA
ASEL, , , ,      2
CM,_Y1,AREA
CHKMSH,'AREA'
CMSEL,S,_Y
AMESH,_Y1
CMDELE,_Y
CMDELE,_Y1
CMDELE,_Y2
MSHKEY,0
CM,_Y,AREA
ASEL, , , ,      1
CM,_Y1,AREA
CHKMSH,'AREA'
CMSEL,S,_Y
AMESH,_Y1
CMDELE,_Y
CMDELE,_Y1
CMDELE,_Y2
MSHKEY,0
CM,_Y,AREA
ASEL, , , ,      6
CM,_Y1,AREA
CHKMSH,'AREA'
CMSEL,S,_Y
AMESH,_Y1
CMDELE,_Y
```

```
CMDELE,_Y1
CMDELE,_Y2
!***************************** Boundary conditions. ****************************
FLST,2,1,4,ORDE,1
FITEM,2,37
/GO
DL,P51X, ,UY,0
FLST,2,1,4,ORDE,1
FITEM,2,39
/GO
DL,P51X, ,UY,0.001
/SOL
SOLVE
FINISH
/POST1
PATH,AAA,2,30,30,
PPATH,1,0,-1,1,,0,
PPATH,2,0,1,1,,0,
AVPRIN,0,0,
PDEF, ,S,Y,AVG
TotalSigma=0
*DO,I,1,30
*GET, SigmaY, PATH, 0, ITEM, SY, PATHPT, I
TotalSigma=TotalSigma+SigmaY
*ENDDO
TotalSigma=TotalSigma/30
FINISH
/PREP7
LSCLEAR,ALL
FLST,2,1,4,ORDE,1
FITEM,2,37
/GO
DL,P51X, ,UY,0
FLST,2,1,4,ORDE,1
FITEM,2,39
/GO
DL,P51X, ,UY,0.001*100e6/TotalSigma
```

```
FINISH
!************************* Solve ****************************
 /SOL
SOLVE
FINISH
/POST1
TotalEnergy=0
*GET, MAXELEMENT, ELEM,  0, NUM, MAXD, ,
*DO,I,1,MAXELEMENT
*GET,Energy, ELEM, I, SENE, , ,
TotalEnergy=TotalEnergy+Energy
*ENDDO
TotalEnergy=TotalEnergy
```

Appendix D- Matlab Code for Crack Propagation

Attached is the Matlab code that was used to find the crack growth.

```matlab
% The results for Stress Intensity Factor should be loaded before using
this code.
m=1;                    % Paris Law Constant
C=0.0125;               % Paris Law Constant
Nmax=50000;             % Number of cycles
RANDD=100;              % Number of Random Sets


RandomSet=rand(1,RANDD);

ao=ai*(RandomSet+(1-mean(RandomSet)));
a=zeros(Nmax,RANDD);



for j=1:RANDD
    a(1,j)=ao(1,j);
    for N=1:Nmax
        for i=1:31
            if ((a(N,j) >= KKK10(i,1)*ai) & (a(N,j) <= KK10(i+1,1)*ai))
                dK=((a(N,j)-KKK10(i,1)*ai)*(KKK10(i+1,3)-
KKK10(i,3))/(KKK10(i+1,1)*ai-KKK10(i,1)*ai)+KKK10(i,3))*ratio;
            end
        end

        da=C*dK^m;

        if a(N,j)>1.88*ai
            da=0;

        end

        a(N+1,j)=a(N,j)+da;

    end
end
avg=zeros(Nmax+1,1);
for i=1:RANDD
    avg=avg+a(:,i);
end
avg=avg/RANDD;

figure(2)
plot(avg/ai,'LineWidth',2)
xlabel('N (cycles)')
ylabel('a/a_o Average Crack lengths')
title('Average Crack Lengths vs Cycles for a structure with 10 cracks')
grid
axis([0 2e4 0.5 2])
```